Computer simulation of liquid crystals

Carl M(ᶜ)*Bride*

Computer Simulation of Liquid Crystals

Carl M^{c}Bride

Ph.D. Thesis

University of Durham

Department of Chemistry.

1999

Abstract

Molecular dynamics simulation performed on modern computer workstations provides a powerful tool for the investigation of the static and dynamic characteristics of liquid crystal phases. In this thesis molecular dynamics computer simulations have been performed for two model systems. Simulations of 4,4′-di-n-pentyl-bibicyclo[2.2.2]octane demonstrate the growth of a structurally ordered phase directly from an isotropic fluid. This is the first time that this has been achieved for an atomistic model. The results demonstrate a strong coupling between orientational ordering and molecular shape, but indicate that the coupling between molecular conformational changes and molecular reorientation is relatively weak. Simulations have also been performed for a hybrid Gay-Berne/Lennard-Jones model resulting in thermodynamically stable nematic and smectic phases. Frank elastic constants have been calculated for the nematic phase formed by the hybrid model through analysis of the fluctuations of the nematic director, giving results comparable with those found experimentally. Work presented in this thesis also describes the parameterisation of the torsional potential of a fragment of a dimethyl siloxane polymer chain, disiloxane diol $(HOMe_2Si)_2O$, using *ab initio* quantum mechanical calculations.

Acknowledgements

I owe a great debt of thanks to my supervisors; Dr. Mark R. Wilson and Professor Judith A. K. Howard. The abundant assistance of Dr. Wilson, with his advice, patience, and time, has made this work possible. I would like to thank my co-worker Melanie Cook for being a star.

I would very much like to thank Dr. Carlos Vega de las Heras of the the Departamento de Química-Física in the Universidad Complutense for his hospitality and support during my field work in Madrid and Dr. Lydia Heck of the Department of Physics for solving so many system administration problems on our Digital and Silicon Graphics workstations. I would like to thank Angus M^{ac}Kinnon for introducing me to the LaTeX program, with which this thesis was written. I would also like to thank the University of Durham Information Technology Service for the provision of software and computer time, as well as the advice of Barry Cornelius and Mike Ellison.

Collaborative Computational Projects 5 and 6 (CCP5/CCP6), the British Liquid Crystal Society (BLCS), and the Institute of Physics (IOP) for organising so many of the conferences that I attended and learnt so much from.

I am also thankful to the Engineering and Physical Sciences Research Council (EPSRC) for a regular income, the Edinburgh Parallel Computing Centre (EPCC) for time on the Cray T3D, and the University of Southampton High Performance Computing Centre (HPCC) for time on the IBM SP2.

Given for one instant an intelligence which could comprehend all the forces by which nature is animated and the respective situation of the beings who compose it - an intelligence sufficiently vast to submit these data to analysis - it would embrace in the same formula the movements of the greatest bodies of the universe and those of the lightest atoms: for it, nothing would be uncertain and the future, as the past, would be present to its eyes.

Laplace 1814.

CONTENTS

LIST OF FIGURES

LIST OF TABLES

CHAPTER 1

Introduction

1.1 Liquid Crystals

1.1.1 Historical Introduction

Liquid crystal mesophases can exist between the solid and liquid phases. In liquid crystals molecules are able to diffuse (as in liquids), yet there exists a preferred direction of alignment as occurs in crystalline solids. It is this combination of fluid and crystal properties that make liquid crystals fascinating materials to study.

The discovery of the liquid crystal phase is attributed to the botanist Friederich Reinitzer [1]. In 1888, whilst working on melts of cholesteryl benzoate in the Institute for Plant Physiology in the University of Prague, Reinitzer wrote [2]:

> *With respect to the melting point... despite continued purification I was able to find only 145.5°. However, it struck me that the substance, in this case, melted not into a clear transparent but always into a cloudy only translucent*

> *liquid, which I initially considered to be a sign of impurities, although both microscopic and crystallographic examinations of the compound revealed no signs of nonuniformity. Upon closer examination, it was then also noted that when heated to higher temperatures, the clouding suddenly vanishes. This happens at 178.5°. ....*

He then proceeded to describe the presence of 'colour phenomenon' which '*...also displays chromatic polarisation*'.

We now know that what Reinitzer observed was a chiral nematic liquid crystal. Phase transitions in homogeneous substances occur at precise temperatures. This led Reinitzer to conclude that the observed material was indeed homogeneous, and the cloudy liquid was a phase of matter different from both the solid, and the clear liquid. Friederich Reinitzer initiated correspondence with Otto Lehmann of the Polytechnical School at Aachen. At that time Lehmann was noted for his work in designing and developing polarisation microscopes. From this point onwards Lehmann developed a strong interest in liquid crystals, later discovering mesophases in purely synthetic materials.

Although work progressed on the study of such systems, it was not until 1922, when G. Friedel [3] published a paper classifying liquid crystals into types (smectic, nematic and cholesteric), that the liquid crystalline phase was finally accepted as being a new state of matter. Friedel also introduced the term mesophase, unhappy with the (even today) widely used name of liquid crystals. At the present date there are at least 40 known mesophases [4].

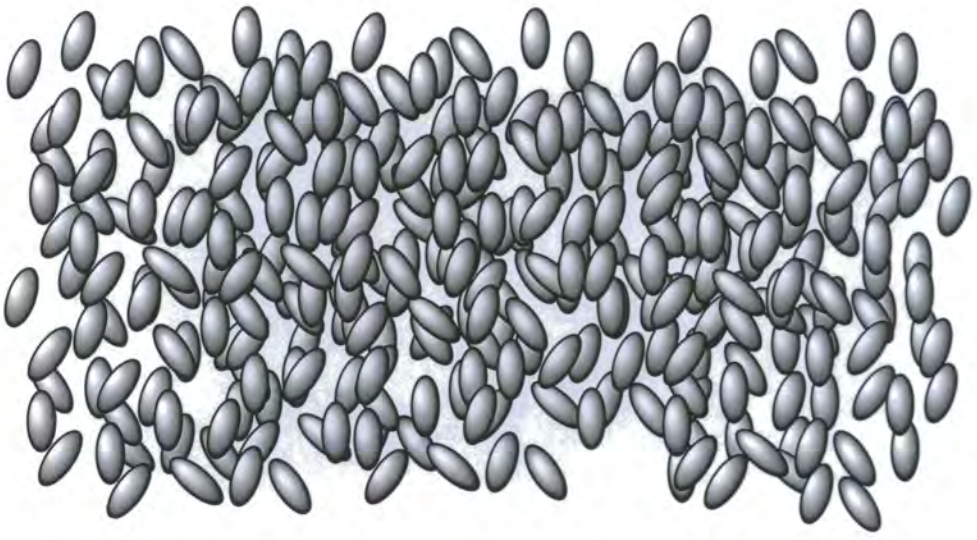

Figure 1.1: Schematic diagram of a nematic phase.

1.1.2 Thermotropic Liquid Crystals

Mesogenic materials whose phase transitions are initiated by changes in temperature are known as *thermotropic* liquid crystals. There are three varieties of thermotropic liquid crystals: nematic, cholesteric (or chiral nematic) and smectic. Nematic liquid crystals (figure 1.1) are characterised by having a high degree of long-range orientational order, but no long-range translational order. Thus in the nematic phase, molecules spontaneously order with their long axes approximately parallel. The cholesteric mesophase (figure 1.2) also exhibits nematogenic ordering, but in addition is composed of chiral molecules. As a consequence of this, the structure has either a left-handed or right-handed (depending on the molecular chirality) twist about an axis normal to the preferred direction of the molecular long axes. The cholesteric phase has the ability to perform selective reflection of circularly polarised light, and a rotatory power more than a thousand times greater than that of an ordinary optically active substance. Smectic phases have a further degree of order. In addition to their orientational order molecules form into layers. For example, in the smectic-A (S_A) phase, layers form with the layer

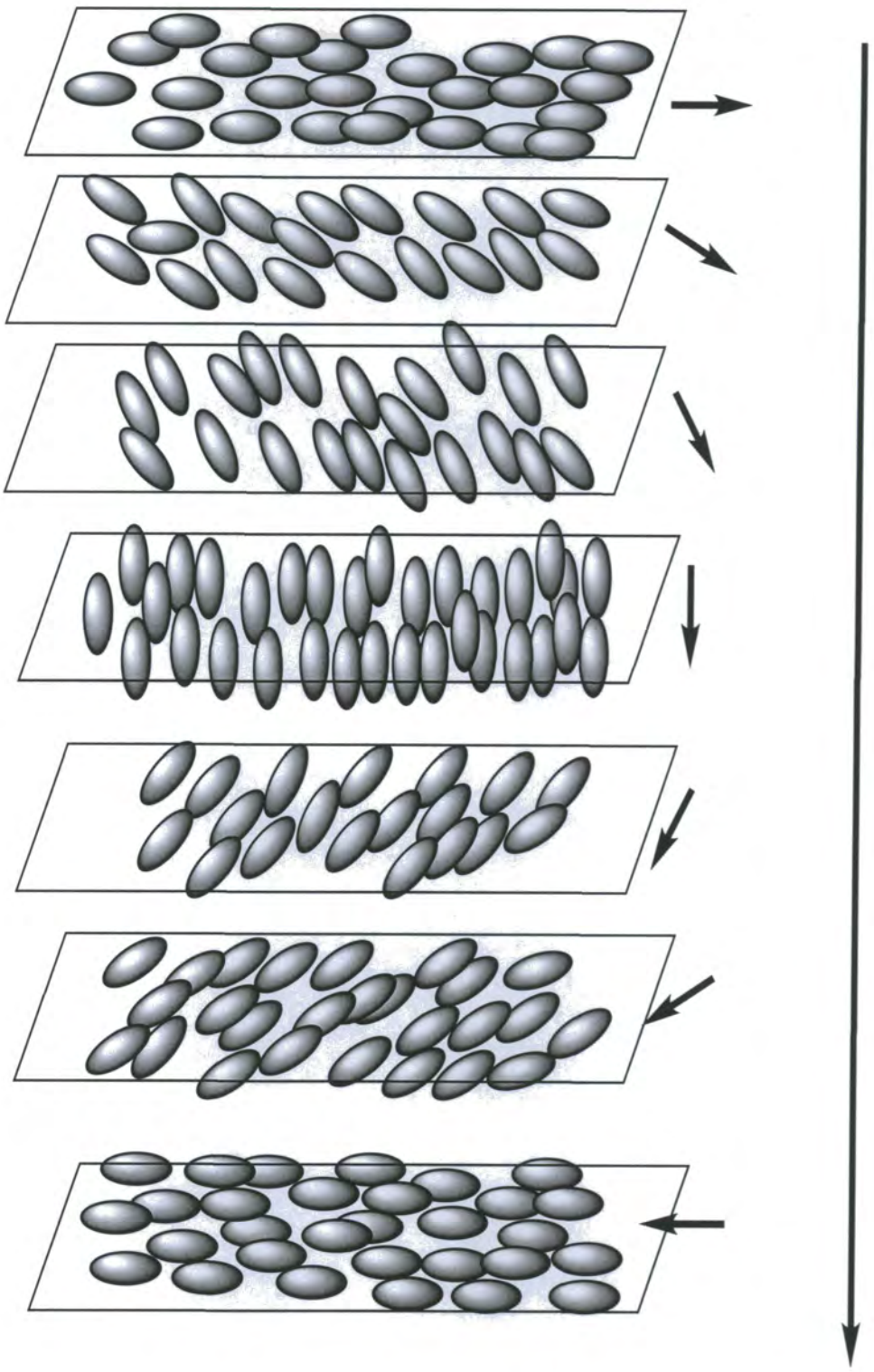

Figure 1.2: Schematic diagram of a cholesteric liquid crystal

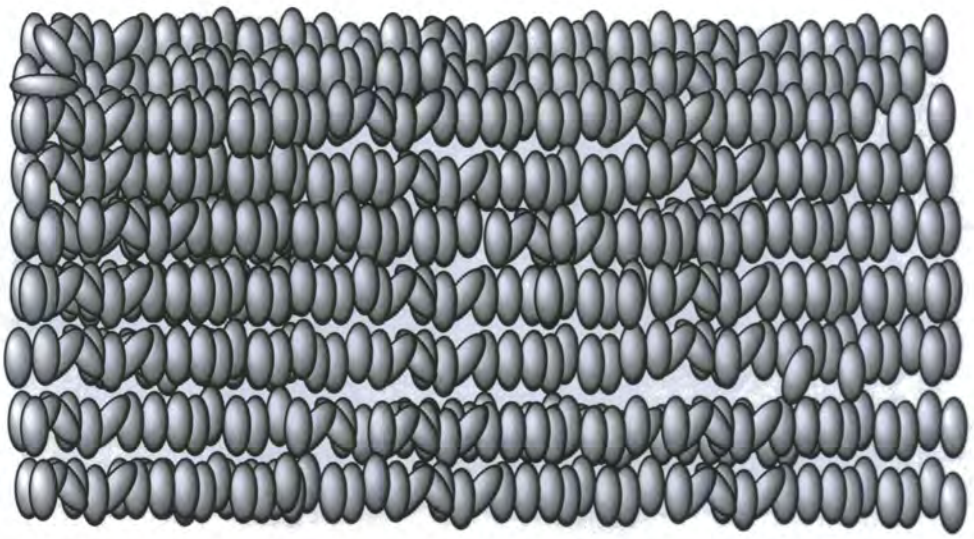

Figure 1.3: Schematic diagram of a smectic A phase

normal parallel to the molecular long axes (see figure 1.3). The smectic-C phase differs from the S_A phase in that the molecules are tilted with respect to the layer normal (see figure 1.4). There are also several other smectic phases, which have long-range positional order [5].

Mesophases can be formed by low molecular mass organic or organometallic molecules. However, high molecular mass polymeric substances also form a variety of liquid crystal phases [6]. Polymeric liquid crystals fall into two categories, depending on where the mesogenic core lies. If the core unit is within the main polymer chain then this is known as a *main-chain* liquid crystal polymer (MCLCP) (figure 1.5). The mesogenic cores may also be suspended from the 'backbone' forming *side-group* liquid crystal polymers (SGLCP) (see figure 1.6). The thermotropic mesophases formed by polymers are highly dependent on the flexibility of the backbone, the nature of the mesogenic unit used and (in the case of SGLCP's) the spacers.

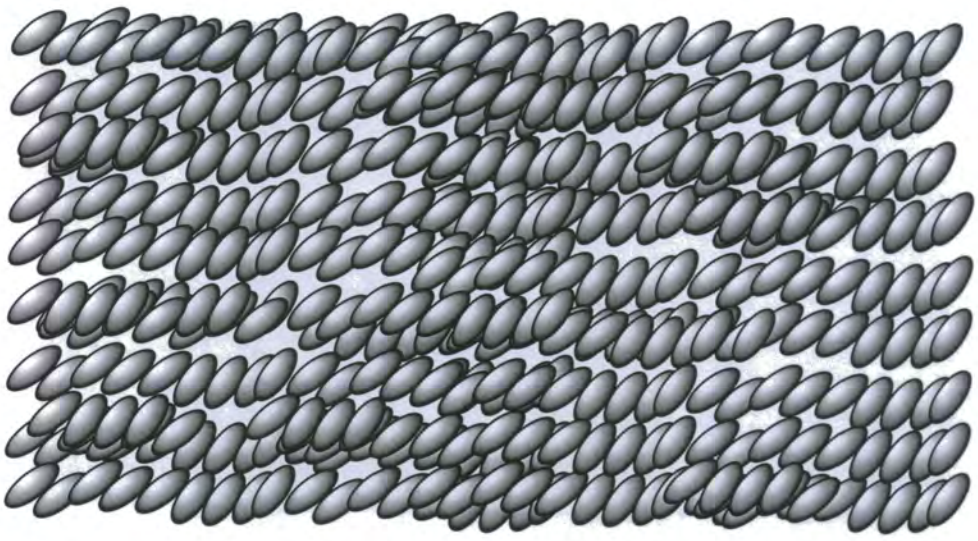

Figure 1.4: Schematic diagram of a smectic C phase

Figure 1.5: Schematic diagram of a main chain liquid crystal polymer.

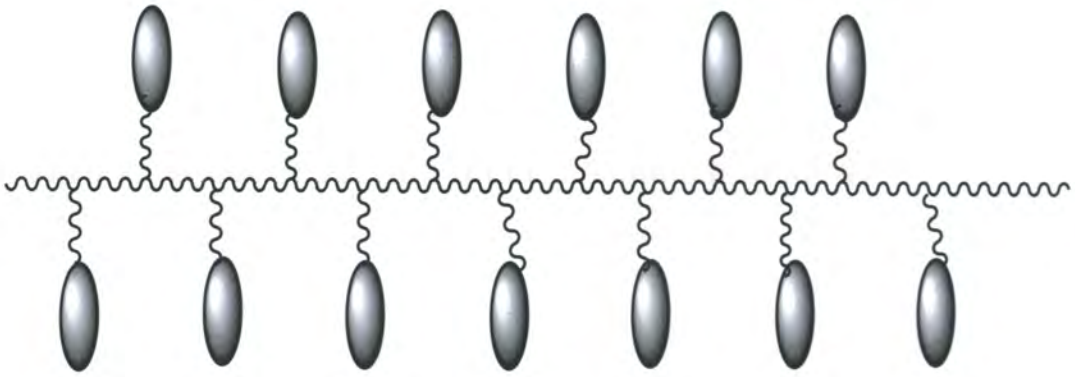

Figure 1.6: Schematic diagram of a side group liquid crystal polymer.

Figure 1.7: Schematic diagram of a surfactant molecule

1.1.3 Lyotropic Liquid Crystals

The phase behaviour of lyotropic liquid crystals is governed by both temperature and solvent concentration. Lyotropic phases are formed by amphiphilic molecules. These consist of a polar head group attached to one or more long non-polar chains (figure 1.7). These molecules are also known as *surfactants* (**surf**ace **act**ive **a**g**ents**). In appropriate solvents amphiphilic molecules can self-assemble to create structures known as *micelles* (figure 1.8). These structures are roughly spherical aggregates in which the chains are 'protected' from the solvent by the polar head groups. As the concentration of amphiphilic molecules increases then much larger structures form, thus creating *lyotropic* phases. Examples of lyotropic phases include the lamellar phase, the cubic phase and the hexagonal phase. The lamellar phase is composed of bilayers separated by water. These form at high surfactant concentrations and are planar, with the chains shielded from the solvent by the head groups (figure 1.9). In the cubic phase the spherical micelles pack together to form an isotropic *body centered cubic* arrangement. The hexagonal phase is formed from tube shaped micelles; the centres of the tubes are filled with chains, and the walls are made from the head groups. These tubes pack into an hexagonal array. Lyotropic liquid crystals are known to form some mesophases which are not exhibited by thermotropic liquid crystals: for example hexagonal columnar structures [7, 8].

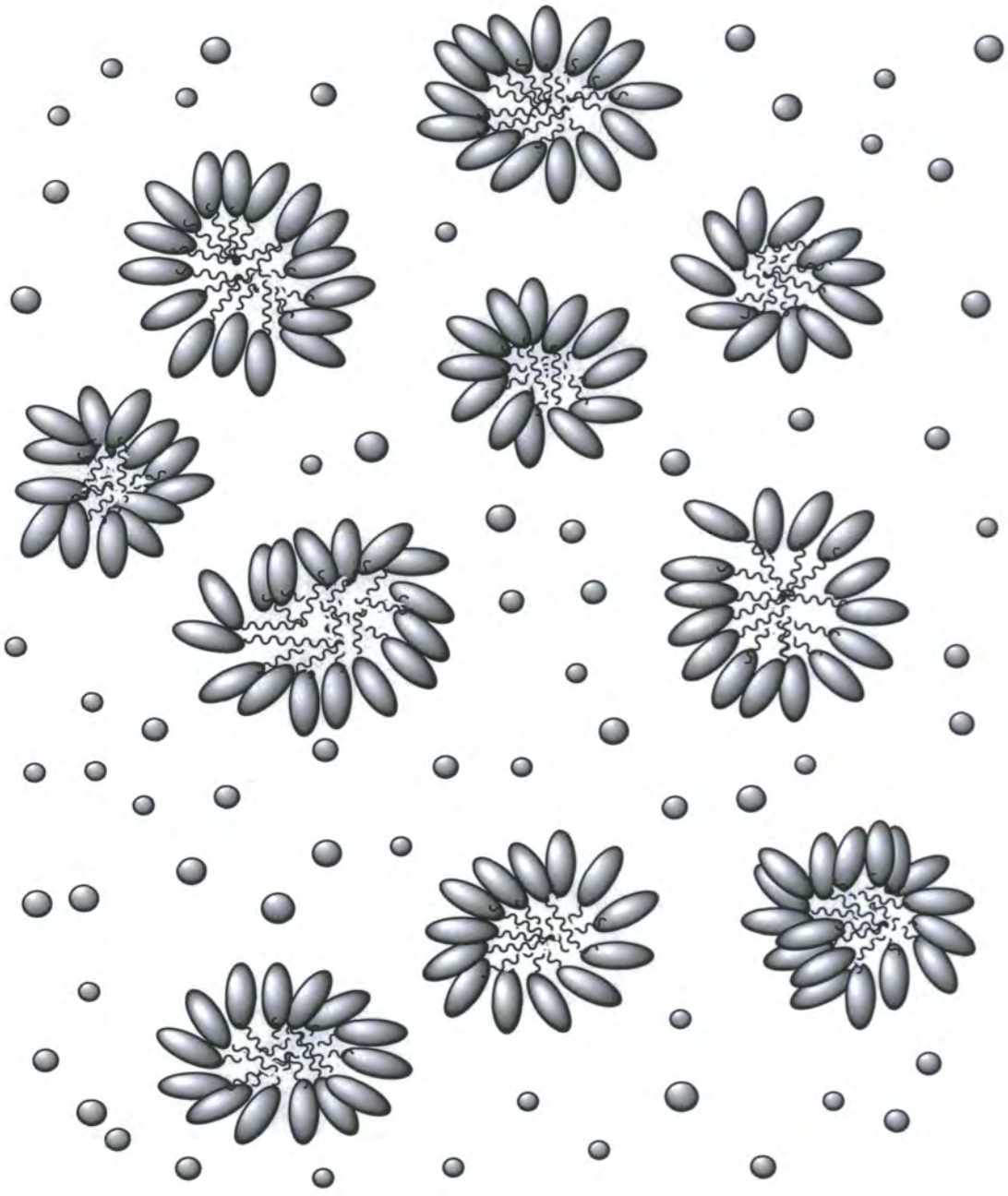

Figure 1.8: Schematic diagram of the micellar phase.

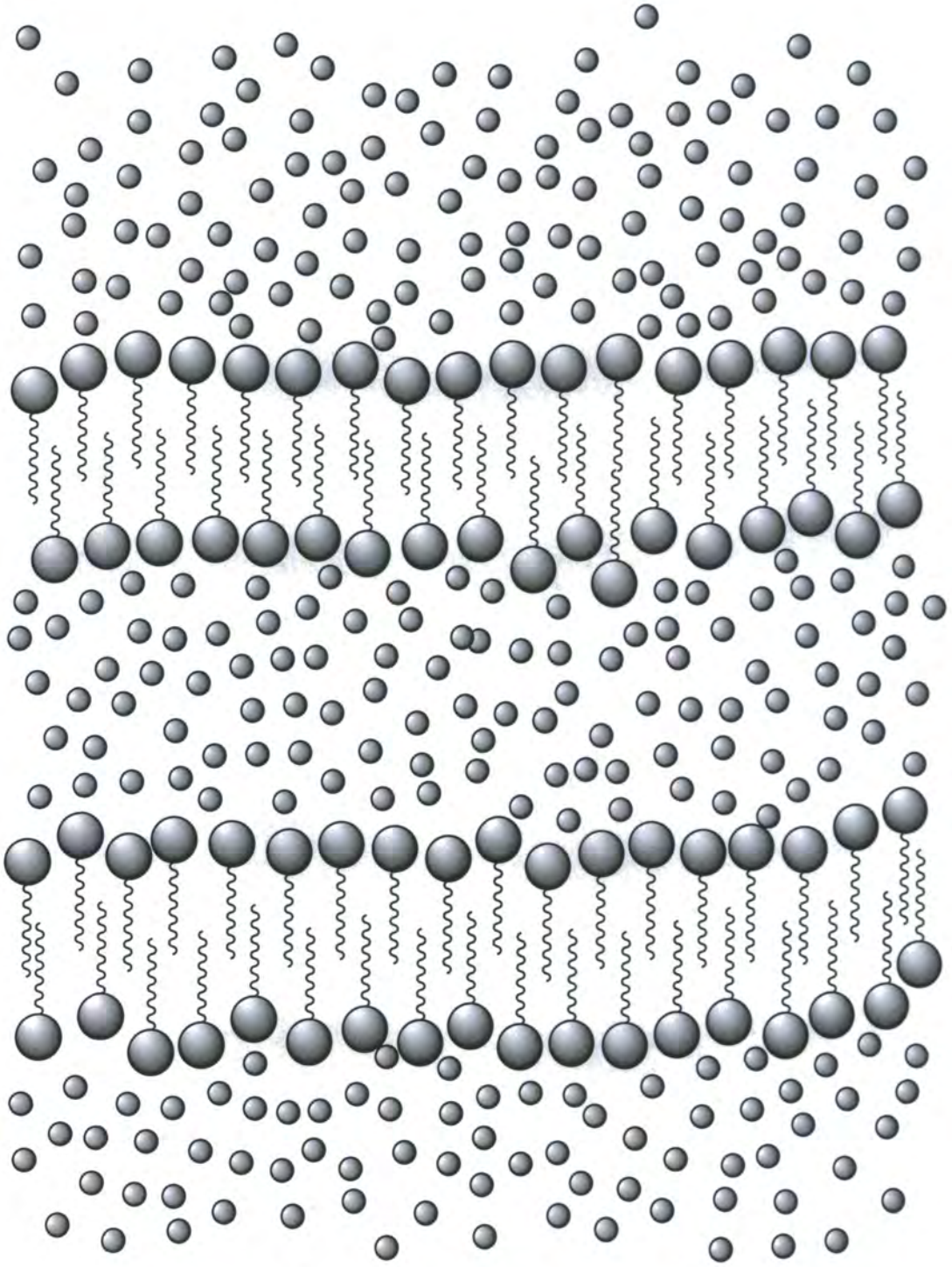

Figure 1.9: Schematic diagram of the lamellar phase.

1.2 Computer Modelling of Liquid Crystals

The primary concern of this thesis is the modelling, computer simulation, and subsequent analysis, of liquid crystal materials. To perform a computational study of a liquid crystalline compound it is first necessary to create a model that contains the "correct physics" to describe the system.

1.3 Review of models of mesogens

It is very common for mesogenic molecules to consist of one or more rigid aromatic units often known as core units, which are joined by linking groups and flanked by two terminal units. This leads to a characteristic geometric molecular shape that is often described as rod-like or lath-like. This rod-like shape creates anisotropic intermolecular forces, with the interactions between the ends of the molecules being weaker than the lateral interactions. It is generally observed that any structural feature that lends itself to increasing the length of the molecule (and providing some modest rigidity, e.g. increased core length, longer terminal or longer linking groups), is conducive to liquid crystal formation as seen by an increased thermal stability of the mesophase. The earliest models of liquid crystals were based on lattice systems with purely orientational dependant interactions of the type described by Maier and Saupe [9] in 1958. In these models a lattice site represents a small region of the liquid crystal. The interaction between nearest neighbour lattice sites is given by the expression

$$V(\theta) = \epsilon \left(\frac{3}{2} \cos^2 \theta - \frac{1}{2} \right) \tag{1.1}$$

where θ is the angle between vectors on neighbouring sites and ϵ is an energy parameter. This expression represents the orientating influence of surrounding regions of nematic fluid. Many Monte Carlo simulations have been undertaken using this model [10, 11],

most famously by Lebwohl and Lasher [12] in 1972. This model predicts a weakly first-order phase transition between the nematic and isotropic states.

1.3.1 Hard anisotropic models

Many of the early models of mesogens consisted of various anisotropic geometrical shapes that represented the overall rod-shaped structure of a mesogen. The early models were based on 'hard' interaction sites. 'Hard molecules' interact via an infinitely steep potential whenever two molecules overlap. These potentials model excluded volume interactions and have demonstrated the stability of a nematic phase for spheroids, and the existence of smectic-A liquid crystals (Frenkel and co-workers [13,14]) for spherocylinders [15–18]. Hard anisotropic models are the liquid crystal analogue of the hard sphere fluid that was extremely successful in studying the behaviour of simple liquids.

1.3.2 Soft interaction site models

'Soft' potentials have attractive as well as repulsive terms.

Lennard-Jones potential

The Lennard-Jones (LJ) 12:6 potential,

$$U_{ij}^{\mathrm{LJ}} = 4\epsilon_{ij}^{\mathrm{LJ}} \left[\left(\frac{\sigma_{ij}{}^{\mathrm{LJ}}}{r_{ij}} \right)^{12} - \left(\frac{\sigma_{ij}{}^{\mathrm{LJ}}}{r_{ij}} \right)^{6} \right], \tag{1.2}$$

is an isotropic model. The interaction between a pair of LJ sites depends only on their distance of separation, and not on their orientation. The potential is designed to model non-bonded interactions and is calculated for pairs of atoms in different molecules, or for pairs of atoms that are in the same molecule, but are separated by more than three bonds. The potential consists of a hard repulsive wall generated by the $\frac{1}{r^{12}}$ term, and a longer range attractive tail, generated by the $\frac{-1}{r^{6}}$ term. There are two parameters in

the LJ model; ϵ represents the well-depth and σ represents the distance at which the attractive and repulsive terms in the potential cancel out.

Gay-Berne potential

The Gay-Berne potential is an anisotropic potential originally designed to represent the overlap between two ellipsoidal Gaussian functions [19]. It has undergone a number of modifications and several versions of the potential have appeared in the literature. In the original form specified by Gay and Berne [20] the potential was fitted to mimic the interactions of a linear chain of four Lennard-Jones interaction sites. The interaction energy, U_{ij}^{GB} between a pair of Gay-Berne (GB) sites depends on the relative orientation of the GB sites, as well as their distance of separation.

$$\begin{aligned} U_{ij}^{\mathrm{GB}} &= 4\epsilon_0^{\mathrm{GB}}[\epsilon^{\mathrm{GB}}(\hat{\mathbf{u}}_i,\hat{\mathbf{u}}_j)]^{\nu}[\epsilon'^{\mathrm{GB}}(\hat{\mathbf{u}}_i,\hat{\mathbf{u}}_j,\hat{\mathbf{r}}_{ij})]^{\mu} \\ &\times \left[\left(\frac{\sigma_0^{\mathrm{GB}}}{r_{ij}-\sigma(\hat{\mathbf{u}}_i,\hat{\mathbf{u}}_j,\hat{\mathbf{r}}_{ij})+\sigma_0^{\mathrm{GB}}}\right)^{12}-\left(\frac{\sigma_0^{\mathrm{GB}}}{r_{ij}-\sigma(\hat{\mathbf{u}}_i,\hat{\mathbf{u}}_j,\hat{\mathbf{r}}_{ij})+\sigma_0^{\mathrm{GB}}}\right)^{6}\right] \end{aligned} \tag{1.3}$$

where $\hat{\mathbf{u}}_i$ and $\hat{\mathbf{u}}_j$ are unit vectors along the Gay-Berne molecular axes, σ is the orientation dependent distance of separation at which attractive and repulsive energies cancel given by

$$\sigma(\hat{\mathbf{u}}_i,\hat{\mathbf{u}}_j,\hat{\mathbf{r}}_{ij}) = \sigma_0\left[1-(\chi/2)\left(\frac{(\hat{\mathbf{r}}_{ij}\cdot\hat{\mathbf{u}}_i+\hat{\mathbf{r}}_{ij}\cdot\hat{\mathbf{u}}_j)^2}{1+\chi(\hat{\mathbf{u}}_i\cdot\hat{\mathbf{u}}_j)}+\frac{(\hat{\mathbf{r}}_{ij}\cdot\hat{\mathbf{u}}_i-\hat{\mathbf{r}}_{ij}\cdot\hat{\mathbf{u}}_j)^2}{1-\chi(\hat{\mathbf{u}}_i\cdot\hat{\mathbf{u}}_j)}\right)\right]^{-1/2} \tag{1.4}$$

with the shape anisotropy parameter χ given by

$$\chi = \left[\frac{(\sigma_{ee}/\sigma_{ss})^2-1}{(\sigma_{ee}/\sigma_{ss})^2+1}\right]. \tag{1.5}$$

In equation 1.3 $\epsilon_0^{\mathrm{GB}}[\epsilon^{\mathrm{GB}}]^{\nu}[\epsilon'^{\mathrm{GB}}]^{\mu}$ is the orientation dependent well depth given by

$$\epsilon^{\mathrm{GB}}(\hat{\mathbf{u}}_i,\hat{\mathbf{u}}_j) = \left[1-\chi^2(\hat{\mathbf{u}}_i\cdot\hat{\mathbf{u}}_j)^2\right]^{-1/2} \tag{1.6}$$

and

$$\epsilon'^{\mathrm{GB}}(\hat{\mathbf{u}}_i,\hat{\mathbf{u}}_j,\hat{\mathbf{r}}_{ij}) = 1-(\chi'/2)\left(\frac{(\hat{\mathbf{r}}_{ij}\cdot\hat{\mathbf{u}}_i+\hat{\mathbf{r}}_{ij}\cdot\hat{\mathbf{u}}_j)^2}{1+\chi'(\hat{\mathbf{u}}_i\cdot\hat{\mathbf{u}}_j)}+\frac{(\hat{\mathbf{r}}_{ij}\cdot\hat{\mathbf{u}}_i-\hat{\mathbf{r}}_{ij}\cdot\hat{\mathbf{u}}_j)^2}{1-\chi'(\hat{\mathbf{u}}_i\cdot\hat{\mathbf{u}}_j)}\right) \tag{1.7}$$

with

$$\chi' = \left[\frac{1-(\epsilon_{ee}/\epsilon_{ss})^{1/\mu}}{1+(\epsilon_{ee}/\epsilon_{ss})^{1/\mu}}\right] \tag{1.8}$$

A variety of different forms of the Gay-Berne potential can be produced by varying the ratios σ_{ee}/σ_{ss} in equation 1.5 (the end-to-end/side-to-side distances at which the potential is zero), $\epsilon_{ee}/\epsilon_{ss}$ in equation 1.8 (the end-to-end/side-to-side well depths), and the exponents μ and ν.

1.3.3 Flexible models

For model mesogens containing multiple interaction sites one can introduce terms to describe the bending of bond angles and the rotation about dihedral angles. This allows the molecular model to become flexible with the ability to explore a variety of conformations. Incorporation of molecular flexibility allows mesogenic models to more realistically reflect the structure of real liquid crystal molecules. Consequently flexible alkyl chains attached to rigid core units or (in the case of dimer liquid crystals) between core units can be modelled in a simulation [21,22]. In recent years there has been much interest in 'realistic' or 'semi-realistic' models for liquid crystals. These have included several simulations of low molecular weight compounds [21, 23–39] and (recently) one simulation study of main chain liquid crystal polymers. The latter have been performed by Lyulin *et al.* [40] with systems of 64 polymer chains with a degree of polymerisation of 10 and alkyl spacers with chain lengths of between 5 and 8.

Force fields

There are a number of parameterised functional forms that have been developed to describe flexible molecules. These include the CHARMM force field [41, 42], the AMBER [43] and AMBER94 force fields [44], the OPLS [45, 46] (**O**ptomised **P**otentials

for **L**iquid **S**imulation) force field developed by Jorgensen and co-workers, and a series of all-atom force fields developed by Allinger and co-workers; MM1 [47], MM2 [48], MM3 [49] and MM4 [50–54]. These force fields are published along with large tables of parameters that are obtained from sources such as vibrational spectroscopy studies, diffraction data and NMR. Force fields are equations that describe the potential energy of a molecule in terms of its mechanical features. The equations are classical mechanical approximations to the *inter-* and *intra*-molecular interactions that control the behaviour of real molecules. The mathematical functions in a force field adopt a number of analytical forms, each of which has a basis in chemical physics. These are parameterised to give accurate energy differences between different conformations of small molecules. In general, the configurational energy of a molecular system may be expressed as:

$$\begin{aligned} U(\mathbf{r_1}, \mathbf{r_2}, ..., \mathbf{r_N}) &= \sum_{i_{\text{bond}}=1}^{N_{\text{bond}}} U_{\text{bond}}(i_{\text{bond}}, \mathbf{r_a}, \mathbf{r_b}) \\ &+ \sum_{i_{\text{angle}}=1}^{N_{\text{angle}}} U_{\text{angle}}(i_{\text{angle}}, \mathbf{r_a}, \mathbf{r_b}, \mathbf{r_c}) \\ &+ \sum_{i_{\text{dihed}}=1}^{N_{\text{dihed}}} U_{\text{dihed}}(i_{\text{dihed}}, \mathbf{r_a}, \mathbf{r_b}, \mathbf{r_c}, \mathbf{r_d}) \\ &+ \sum_{i=1}^{N-1} \sum_{j>i}^{N} U_{\text{pair}}(i, j, \mid \mathbf{r_i} - \mathbf{r_j} \mid) \\ &+ \sum_{i=1}^{N-2} \sum_{j>i}^{N-1} \sum_{k>j}^{N} U_{3\_\text{body}}(i, j, k, \mathbf{r_i}, \mathbf{r_j}, \mathbf{r_k}) \\ &+ \sum_{i=1}^{N} U_{\text{extn}}(i, \mathbf{r_i}, \mathbf{v_i}) \end{aligned} \tag{1.9}$$

where $U_{\text{bond}}, U_{\text{angle}}, U_{\text{dihed}}, U_{\text{pair}}$ and U_{3_body} are the empirical functions representing chemical bonds, valence angles, dihedral angles, pair-body and three-body forces respectively, and U_{extn} represents an external potential. Force fields come in two varieties, all-atom and united-atom force fields. All-atom force fields such as MM2 and MM3 tend to be more accurate in describing the energy difference between different conformations,

but are more expensive than united-atom models. In united-atom force fields hydrogen atoms that are bonded to carbon atoms are represented by single site potentials (such as CH_2 or CH_3). This method was first employed by Ryckaert and Bellemans [55], and is known as the *united-atom* approximation. It greatly cuts down the computational expense of a simulation by reducing the number of non bonded interactions. It is also a good idea not to explicitly incorporate the hydrogens because of the fact that the bond stretching frequency is so high that there is a very poor coupling between C-H vibrations ($T_{C-H} \approx 10$ fs) and the slower, 'softer' vibrations of the rest of the molecule, so they take a long time to 'thermalise', i.e. for the equipartition principle to be obeyed. Comparisons of all-atom and united-atom approximation for a number of nucleosides and dipeptides were calculated in the AMBER [43] paper and validated the use of the united-atom approximation.

1.3.4 Quantum mechanical models

The main difference between classical methods and quantum mechanical methods is the explicit inclusion of the electrons in quantum calculations. This requires one to solve the Schrödinger equation for the system of interest. For a system of more than one electron this necessitates the use of approximate methods (the three body problem has no exact solution). Quantum mechanical calculations are very expensive in terms of computer time, and at the present time calculations are restricted to single liquid crystal molecules containing no more than 50 atoms [56,57]. There are currently several available programs that provide access to 'off-the-shelf' *ab initio* quantum calculations (such as Gaussian94 [58]). These calculations can provide the energy of a structure in a specified conformation, thereby allowing the development of force field parameters for various structural features of a molecule, such as torsional potentials. A study of

the parameterisation of a torsional potential is presented in chapter 6.

1.4 Simulation techniques

The aim of molecular simulation is to generate a representative statistical sample of the system. This is done by enclosing a number of molecules (with present computer power this number is between 60 and 10,000, depending on the complexity of the model) in a region of space. This region is then periodically 'imaged', i.e. when a molecule leaves one side of the region, it appears on the opposite side, thus approximating an infinite volume. One then assigns velocities to the computer molecules, (e.g. from a Maxwell-Boltzmann distribution) corresponding to the temperature of interest. The equations of motion are then solved within the computer to generate a trajectory in phase space from which macroscopic quantities can be calculated.

1.4.1 Molecular dynamics

In general a molecular dynamics code will take in information about the system to be simulated in the form of a force field, an initial configuration, information about the type of simulation required, and the periodic boundary conditions to be used. The simulation code will then perform the molecular dynamics, periodically outputting information on the state of the system, as well as coordinates and velocities of the system for later analysis. With good simulation code, the main tasks of the simulator is to prepare a system for simulation (i.e. a molecular model and an initial configuration), and then perform a meaningful analysis of the output data produced during the course of the simulation run.

1.4.2 Monte Carlo

The Monte Carlo method stochastically samples the phase space of a given ensemble. The method is stochastically equivalent to molecular dynamics and provides an alternative simulation method for many systems. Monte Carlo simulations can easily be extended to a number of ensembles where it is difficult to carry out molecular dynamics. However, the drawback of this technique is that it is unable to generate dynamical information (such as rates of molecular reorientation).

The simulations in this thesis concentrate on molecular dynamics method, a technique which will be discussed in detail in chapter 2.

CHAPTER 2

Molecular Dynamics Simulation

2.1 Introduction

The classical equations of motion will be introduced in the first part of this chapter. It is these equations that are solved during a molecular dynamics simulation to produce a set of positions and velocities that describe the time evolution of the system under investigation. The analysis of the coordinate and velocity data is the subject of the latter part of this chapter. It is this analysis that allows us to build a quantitative picture of the physical behaviour of our mesogenic model.

2.2 Classical Equations of Motion

In classical simulations the positions of spherical atomic sites can be represented by a set of coordinate vectors $\{\mathbf{r}_i\}$. If the sites are set in motion with velocities $\{\mathbf{v}_i\}$ a

molecular dynamics program can be used to solve the translational equations of motion:

$$\frac{d\mathbf{v}_i}{dt} = \frac{\mathbf{f}(r_i)}{m_i}, \tag{2.1}$$

$$\frac{d\mathbf{r}_i}{dt} = \mathbf{v}_i. \tag{2.2}$$

The forces $\mathbf{f}(r_i)$ in equation 2.1 are calculated from

$$\mathbf{f}_i(r_i) = -\nabla U_i(r_i) \tag{2.3}$$

where $U_i(r_i)$ is the potential energy of site i.

For anisotropic sites rotation about the center of mass of the sites must also be considered. If the anisotropic site is axially symmetric and represented by a unit vector $\hat{\mathbf{e}}$ along its long axis, the torque about its center of mass is given by

$$\mathbf{T}_i = \hat{\mathbf{e}}_i \times \mathbf{g}_i \tag{2.4}$$

where

$$\mathbf{g}_i = -\nabla_{\hat{\mathbf{e}}_i} U_i(\mathbf{r}_i, \mathbf{e}_i) = -\left(\frac{\partial U}{\partial \hat{\mathbf{e}}_x}, \frac{\partial U}{\partial \hat{\mathbf{e}}_y}, \frac{\partial U}{\partial \hat{\mathbf{e}}_z} \right). \tag{2.5}$$

In equation 2.4 the torque can be seen as the force acting on a point separated by a unit distance from the center of mass, acting normal to the symmetry axis of the particle. It is usual to take the component of $\mathbf{g}$ perpendicular to the molecular axis

$$\mathbf{g}_i^{\perp} = \mathbf{g}_i - (\mathbf{g}_i \cdot \hat{\mathbf{e}}_i)\hat{\mathbf{e}}_i \tag{2.6}$$

so that equation 2.4 becomes

$$\mathbf{T}_i = \hat{\mathbf{e}}_i \times \mathbf{g}_i^{\perp}. \tag{2.7}$$

The rotational equations of motion are then written as

$$\frac{d\hat{\mathbf{e}}_i}{dt} = \mathbf{u}_i \tag{2.8}$$

and

$$\frac{d\mathbf{u}_i}{dt} = \frac{\mathbf{g}_i^{\perp}}{I_i} + \lambda \hat{\mathbf{e}}_i \tag{2.9}$$

where λ is an undetermined Lagrange multiplier, given by equation 2.15 in section 2.3.2, and I is the moment of inertia.

2.3 Integration Algorithms

The process of MD simulation involves the solution of an *initial value* problem. The equations of motion (2.1-2.2, 2.8-2.9) are solved computationally using *finite difference* methods (also known as *step-by-step* methods). One of the most widely used integration schemes is that of Verlet [59] and this is the method implemented in the simulation codes DL_POLY [60] and GB-MOL [61] used in this thesis.

2.3.1 Verlet leapfrog scheme (isotropic particles)

For isotropic particles one is concerned solely with the equations of motion of the centers of mass. The Verlet leapfrog algorithm [59] generates trajectories in the NVE (microcanonical) ensemble. In the leapfrog scheme the positions ($\mathbf{r}_i$) and forces ($\mathbf{f}_i$) are started at time t, whilst the velocities ($\mathbf{v}_i$) are started at a time, $t - \Delta t$ (where Δt is the simulation time step). The forces and masses (m_i) are used to advance the velocities by one timestep. A truncated Taylor series expansion for the velocity gives

$$\mathbf{v}_i(t + \frac{1}{2}\Delta t) \approx \mathbf{v}_i(t - \frac{1}{2}\Delta t) + \Delta t \frac{\mathbf{f}_i(t)}{m_i}. \tag{2.10}$$

The positions are then advanced using the new velocities

$$\mathbf{r}_i(t + \Delta t) = \mathbf{r}_i(t) + \Delta t \;\; \mathbf{v}_i(t + \frac{1}{2}\Delta t). \tag{2.11}$$

When the positions and the velocities are both required at the same time step, the velocities at time t can be obtained by averaging the velocities at half a timestep either

side of t:

$$\mathbf{v}_i(t) = \frac{1}{2}[\mathbf{v}_i(t - \frac{1}{2}\Delta t) + \mathbf{v}_i(t + \frac{1}{2}\Delta t)]. \tag{2.12}$$

2.3.2 Verlet leapfrog scheme (anisotropic particles)

For anisotropic particles (such as the Gay-Berne (GB) particle), rotational motion must also be considered in the integration algorithm. It can be handled independently of the linear motion but in a similar fashion [62–66]. For linear particles with only two degrees of rotational freedom, a leapfrog scheme to solve equations 2.8-2.9 is given by

$$\mathbf{u}_i(t + \frac{1}{2}\Delta t) \approx \mathbf{u}_i(t - \frac{1}{2}\Delta t) + \Delta t \left(\frac{\mathbf{g}_i^{\perp}}{I_i} + \lambda(t)\hat{\mathbf{e}}_i(t) \right) \tag{2.13}$$

and

$$\hat{\mathbf{e}}_i(t + \Delta t) \approx \hat{\mathbf{e}}_i(t) + \Delta t \;\; \mathbf{u}_i(t + \frac{1}{2}\Delta t) \tag{2.14}$$

with

$$\Delta t \lambda_i(t) = -2\mathbf{u}_i(t - \frac{1}{2}\Delta t) \cdot \hat{\mathbf{e}}_i(t). \tag{2.15}$$

2.3.3 Bond length constraints - the SHAKE algorithm

It is often desirable to constrain bond lengths during a molecular dynamics simulation. Bond stretching motion occurs at high frequencies ($T_{\mathrm{C-C}} \approx 37$ fs) and the exchange of energy between bond stretches and other degrees of freedom can be rather poor. In addition to this, elimination of bond stretching motion from a simulation allows much longer time steps to be taken during the integration of the equations of motion. The SHAKE method [67] provides an iterative scheme that allows bond length constraints to be incorporated into the leap frog algorithm. SHAKE is available in the DL_POLY and GBMOL simulation codes described in section 2.5, and is used throughout the simulations described in this thesis.

2.4 Starting MD simulations

Once a force field has been chosen and parameterised for the mesogen to be simulated, a starting configuration is built. It is often difficult to pack the molecules in a periodic cell at liquid densities without considerable overlaps between neighbouring molecules. Instead a short program is used to create a regular array of molecules centered on, for example, a cubic array of lattice points. If this array is suitably spacious and an isotropic starting configuration is required, it is possible to add a random displacement and orientation to each of the molecules so as to introduce disorder to the system. From this configuration it is then possible to perform MD at a very high (e.g. 10^{15} atm) pressure in order to compress the system to liquid densities. This produces a configuration suitable to start the liquid state equilibration runs. If it is preferable to start the simulations from a system that has a high degree of orientational order (a pseudo-nematic starting configuration), then the following procedure can be followed. A non-overlapping perfectly aligned system is produced with each molecule positioned on a cubic lattice point. A small random displacement is made to the molecular positions in each direction and the system is compressed by applying a small linear scaling to the molecular centers of mass. This is followed by a short duration molecular dynamics simulation at 10 K to remove the high energy configurations caused by molecules coming unrealistically close together. A series alternate coordinate scalings and molecular dynamics runs may then be carried out until the desired density is reached. In this way it is possible to create a starting configuration with a nematic order parameter of $S_2 \approx 0.6$.

2.5 Simulation codes

The simulations undertaken in this work were performed by two simulation programs, DL_POLY [60] produced by EPSRC Collaborative Computational Project Number 5 (CCP5) and GB-MOL [61] written by Dr. M. R. Wilson, University of Durham.

2.5.1 DL_POLY

DL_POLY is a molecular dynamics simulation code based on the Verlet Leapfrog integration scheme (see section 2.3.1). It can perform simulations in the NVE, NVT, NpT and $N\sigma T$ ensembles, and can use a number of different periodic boundary conditions. DL_POLY also contains a choice of classical force fields and a selection of methods for handling long range electrostatic potentials. DL_POLY was developed by W. Smith and T. R. Forester for CCP5 and the Advanced Research Computing Group (ARCG) at Daresbury Laboratory and is available free to academic institutions. DL_POLY is portable over a variety of UNIX platforms, and implements both MPI and PVM options to allow for parallel operation. DL_POLY requires the input of, at least, three files: FIELD, CONFIG and CONTROL. The FIELD file is a file containing the parameters and functional forms of the force field of the molecule. The CONFIG file contains coordinates and (for a restarted system) velocities and forces for the system. The CONTROL file provides parameters describing the nature of the simulation: time step, ensemble to be used, fixed thermodynamic quantities etc. During, and at the end of, a MD simulation data is written out from the DL_POLY code. The most useful output file is the HISTORY file which contains a dump of atomic coordinates, velocities and forces at a series of timesteps throughout the simulation. It is on this file that the data analysis is performed (see section 2.7).

2.5.2 GB-MOL

The GB-MOL program was written by Dr. M. R. Wilson (University of Durham). This code incorporates both Gay-Berne and Lennard-Jones potentials, and can simulate systems in the NVT, NpT and NVE ensembles using the anisotropic form of the Verlet Leapfrog algorithm (see section 2.3.2). It has options for several torsional potentials: Ryckaert-Bellemans, AMBER3 and MM2. GB-MOL functions in a similar fashion to DL_POLY, with the additional feature of the anisotropic Gay-Berne potential. It is available for single processor workstations, and multi-processor machines using PVM or MPI message passing harnesses.

2.6 Testing of MD algorithms

DL_POLY has already undergone a series of rigorous tests, including simulations of metals, a shell model of water, linked rigid bodies at constant pressure, and an osmosis experiment with a semi permeable membrane [60]. GB-MOL [61] is a much more recent code and prior to the work described in this thesis it was necessary to test the torsional potential and constant pressure routines. Testing of the pressure routine and the torsional potential was carried out on methane and butane respectively and details of this are given in appendix A.

For simulations in which the total energy of the system is conserved (NVE ensemble) it is necessary to test the numerical stability of an integration algorithm with respect to the size of the time step, because the latter strongly influences energy conservation. The time step should be sufficiently short to correctly account for the fastest motions within the molecule. When bond stretching motion is removed with the SHAKE algorithm, the fastest motion consists of bond bends with a typical period of 110 fs. The length of the timestep has a fundamental effect on the truncation errors of the

algorithm. The truncation error is a measure of how accurately the finite difference algorithm approximates the correct solution of the coupled differential equations. The integration algorithm uses a truncated expression to calculate each subsequent MD step (equations 2.10, 2.11). With long timesteps the higher order terms, which are neglected, become increasingly significant. We are concerned with using the largest timestep possible in a simulation, so truncation errors must be carefully monitored. An assessment of a suitable time step to employ is performed by undertaking a series of short runs from the same initial configuration, for the same total time, but each employing a different time step Δt. For the Verlet integration algorithm the plot of timestep squared against the standard deviation of the total energy $\langle \Delta \mathcal{H}^2 \rangle^{\frac{1}{2}}$ should result in a straight line graph over the region for which the algorithm is stable [68]. From the graph shown in figure 2.1, one can see that the truncation errors become significant for timesteps greater than 3.5 fs. Beyond this point, energy conservation is poor, indicating that only timesteps lower than 3.5 fs should be used for molecular systems. At very short timesteps (less than 1 fs) one starts to meet rounding errors associated with the integration steps and the SHAKE algorithm. These rounding errors provide a fundamental limit on the accuracy of the trajectory generated by the leap frog algorithm.

2.7 Analysis of Molecular Dynamics Data

Coordinates, velocities and forces are available at each step of a molecular dynamics simulation. However, it is always necessary to further process these data to obtain physically useful quantities that are able to characterise the structure and dynamics of the material under investigation. Sections 2.7.1 to 2.7.5 summarise the calculation of the main structural and dynamical quantities of interest in the study of liquid crystal

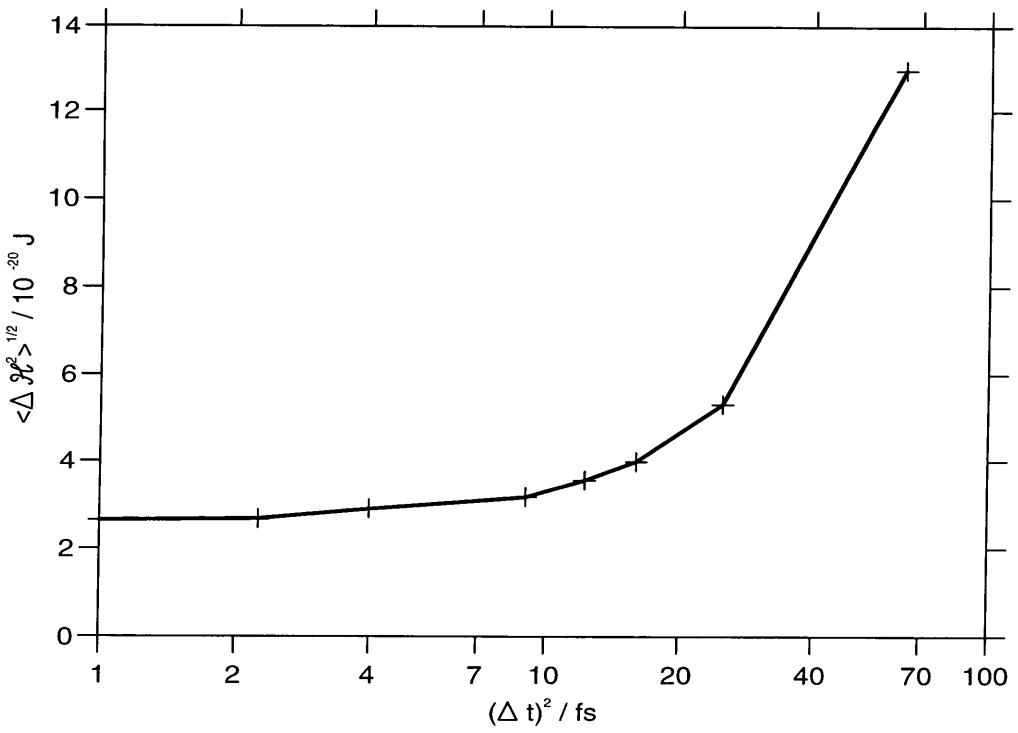

Figure 2.1: Standard deviation of total energy against time step squared.

systems.

2.7.1 Orientational Order

Nematic director

In the nematic phase it is very useful to define a quantity that represents the average alignment of the long axis of the molecules. This quantity is the *director* and is represented by the unit vector **n**. The director can be calculated from the equation [69]

$$Q_{\alpha\beta} = \frac{1}{N_{\mathrm{m}}} \sum_{j=1}^{N_{\mathrm{m}}} \left(\frac{3}{2} \hat{e}_{j\alpha} \hat{e}_{j\beta} - \frac{1}{2} \delta_{\alpha\beta} \right), \qquad \alpha, \beta = x, y, z, \tag{2.16}$$

where Q is a second rank tensor, $\hat{\mathbf{e}}_j$ is a unit vector along the long axis of the molecule, and $\delta_{\alpha\beta}$ is the Kronecker delta. Diagonalisation of this tensor gives three eigenvalues λ_+, λ_0 and λ_-, and **n** is the eigenvector associated with the largest eigenvalue (λ_+).

Order Parameter S_2

Once a director for a particular configuration is known, it is desirable to measure the degree of alignment with respect to this director. This can be done by defining a function such that for a completely disordered system the function would return a value of zero, and for a perfectly aligned system, (with all molecules parallel to the director), would return a value of one. In 1939 Zwetkoff [70] introduced such a function:

$$S_2 = \langle P_2(\mathbf{n} \cdot \mathbf{e}) \rangle = \langle P_2(\cos\theta) \rangle = \left\langle \frac{3}{2}\cos^2\theta - \frac{1}{2} \right\rangle \tag{2.17}$$

where S_2 is known as the uniaxial order parameter. Here P_2 is the second order Legendre polynomial, θ is the angle between a molecular axes and the director $\mathbf{n}$, and the angle brackets indicate an ensemble average. S_2 has the properties we desire: for a system of perfectly aligned molecules, θ is equal to 0 or π for every molecule giving

$$\langle P_2(\cos\theta) \rangle = 1, \tag{2.18}$$

and for a system of randomly aligned molecules [71]

$$\left\langle \cos^2\theta \right\rangle = \frac{\int_0^\pi \sin\theta \cos^2\theta \; d\theta}{\int_0^\pi \sin\theta \; d\theta} = \frac{1}{3} \tag{2.19}$$

giving

$$\langle P_2(\cos\theta) \rangle = 0. \tag{2.20}$$

In a simulation S_2 can be calculated using equation 2.17, or, as is more usual, S_2 can be obtained from the diagonalisation of equation 2.16, where $S_2 = \lambda_+ = -2\lambda_0$ in a uniaxial nematic.

For non-linear molecules a choice must be made for the vector $\mathbf{e}_j$ in equations 2.16, 2.17. For a mesogenic molecule, which has a rigid core unit, then one may take the vector along the long axis of the core to represent $\mathbf{e}_j$. Alternatively, one may define $\mathbf{e}_j$

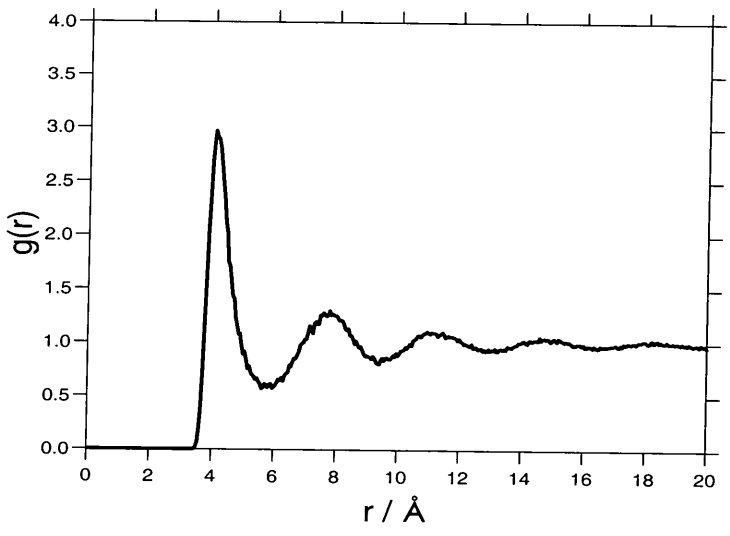

Figure 2.2: RDF for a system of Lennard-Jones atoms.

as the molecular long axis vector obtained through the diagonalisation of the inertia tensor [25]

$$I_{\alpha\beta} = \sum_i m_i(r_i^2\delta_{\alpha\beta} - r_{i\alpha}r_{i\beta}), \tag{2.21}$$

where the atomic distance vector $\mathbf{r}_i$ is measured relative to the molecular center of mass. To calculate the ordering of individual parts of a flexible molecule it is possible to replace the vector $\mathbf{e}_j$ with a bond vector, thus allowing the calculation of order parameters for individual bonds [21].

2.7.2 Distribution Functions

Radial Distribution Function $g(r_{ij})$

The pair distribution function, or *radial distribution function* (RDF), $g(r)$ provides information on the structure of the fluid, a measure of the probability of finding two particles at a distance $|\mathbf{r}_{ij}|$ from each other. The form of the RDF for a monatomic fluid (for example liquid argon or a Lennard-Jones fluid), is given in figure 2.2. The first, and largest, peak is located approximately at the minimum in the pair potential,

and corresponds to the first solvation shell. The following peaks are both successively smaller and broader, until beyond the fourth or fifth shell the function tends to unity. At large distances there is no correlation between the atomic positions and that of the 'origin' atom and so the RDF tends to the ideal-gas limit. The RDF for a fluid of N particles is given by

$$g(r_{ij}) = \frac{V}{N^2} \left\langle \sum_{i}^{N} \sum_{j \neq i}^{N} \delta\left(\mathbf{r} - \mathbf{r}_{ij}\right) \right\rangle, \tag{2.22}$$

where $\mathbf{r}_{ij}$ is the vector between the centers of mass of particles i and j. In the analysis of the data from simulations, the delta function is replaced by a 'top-hat' function, and pairs within this range are sorted into a histogram. In the analysis of smectic phases it is useful to plot the radial distribution function parallel ($g_{\parallel}(r)$) and perpendicular ($g_{\perp}(r)$) to the director $\mathbf{n}$, providing information on the *inter*-layer and *intra*-layer structure.

Orientational pair correlation parameter $g_2(r_{ij}, \mathbf{\Omega}_i, \mathbf{\Omega}_j)$

The pair correlation function g_2 provides information on how aligned pairs of molecules are as a function of distance [72]:

$$g_2(r_{ij}) = \langle P_2\left(\cos\theta_{ij}\left(r\right)\right)\rangle, \tag{2.23}$$

where θ_{ij} is the angle between vectors $\mathbf{e}_i$ and $\mathbf{e}_j$, and the ensemble average includes all pairs of particles.

2.7.3 Structure Factor $S_{\mathrm{CM}}(\mathbf{k})$

Results from X-ray diffraction experiments provide a diffraction pattern that is related to the structure of the material under investigation. The intensity of the scattered radiation is proportional to the structure factor

$$S_{\mathrm{CM}}(\mathbf{k}) = \frac{1}{N_m} \left\langle \left| \sum_{j=1}^{N_m} \exp(-i\mathbf{k}.\mathbf{R}_j) \right|^2 \right\rangle \tag{2.24}$$

where $\mathbf{R}_j$ is the position vector of the center of mass of the j^{th} molecule, and $\mathbf{k}$ is a reciprocal lattice vector for the periodic system of dimensions $L_x \times L_y \times L_z$,

$$\mathbf{k} = 2\pi \left(\frac{n_x}{L_x}, \frac{n_y}{L_y}, \frac{n_z}{L_z} \right). \tag{2.25}$$

Peaks in $S_{\mathrm{CM}}(\mathbf{k})$ correspond directly to translational ordering within a liquid crystal phase, indicating the existence of smectic phases.

2.7.4 Diffusion D

For molecular dynamics simulations the diffusion coefficient D is a key property of the fluid. A sharp drop in the diffusion coefficient indicates the onset of crystallisation/solidification, and aids in distinguishing between thermodynamically stable liquid crystalline phases and those in which orientational or translational order have been frozen into the system. The diffusion coefficient can be calculated from the integral of the velocity autocorrelation function,

$$D = \frac{1}{3} \int_0^\infty \langle \mathbf{v}_i(t).\mathbf{v}_i(0) \rangle \; dt \tag{2.26}$$

where $\mathbf{v}_i(t)$ is the velocity of the molecular center-of-mass. For long time scales the corresponding Einstein relation can be used to obtain D:

$$2tD = \frac{1}{3} \left\langle \mid \mathbf{r}_i(t) - \mathbf{r}_i(0) \mid^2 \right\rangle \tag{2.27}$$

where $\mathbf{r}_i(t)$ is the molecular position vector. To improve the statistics the calculation is performed for each molecule in the system, and D is averaged over several time origins for $\mathbf{r}_i(0)$.

2.7.5 Reorientation $C_l(t)$

Reorientation of molecules and molecular fragments can be described by reorientation time-correlation functions [73, 74] of the form

$$C_l(t) = \langle P_l(\hat{\mathbf{e}}_i(t_0) \cdot \hat{\mathbf{e}}_i(t + t_0)) \rangle \,, \tag{2.28}$$

where $\hat{\mathbf{e}}_i$ is a unit vector parallel to the axis of the molecule or bond i, and $P_l()$ is a Legendre polynomial of order l.

The quantities described in sections 2.7.1 - 2.7.5 will be used to characterise the liquid crystal phases simulated in chapters 3 and 4.

CHAPTER 3

Simulation of Liquid Crystals using Atomistic Potentials

3.1 Introduction

In the past few years the rapid rise in the speed of modern microprocessors has led to an increase in the number of chemical systems that can be studied by classical simulation techniques. A number of atomistic studies of liquid crystal systems now exist [21, 23–39]. However, these studies have largely been for small systems (less than one hundred molecules) and relatively small simulation times (100-200 ps). In all cases the runs have been too short to demonstrate the thermodynamic stability of a mesophase.

This chapter describes molecular dynamics simulations of the mesogen 4,4′-di-n-pentyl-bibicyclo[2.2.2]octane using an united-atom model. The long simulation runs

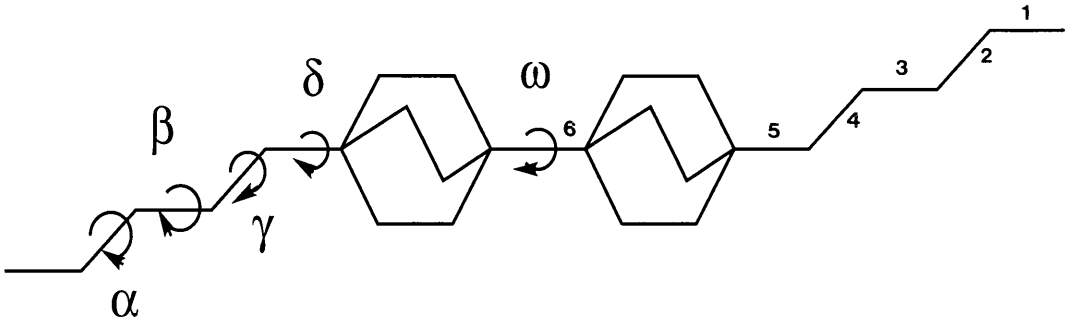

Figure 3.1: Molecular structure of 4,4′-di-n-pentyl-bibicyclo[2.2.2]octane (5,5-BBCO), with bond and dihedral labels.

that have been undertaken demonstrate the growth of an orientationally ordered phase directly from an isotropic fluid. This is the first time that this has been seen for an atomistic model. This chapter gives details of the simulations and describes the nature of the orientationally ordered phase, its structure and its dynamics.

3.2 Simulation of 4,4′-di-n-pentyl-bibicyclo[2.2.2]octane

The mesogen 4,4′-di-n-pentyl-bibicyclo[2.2.2]octane (5,5-BBCO) (figure 3.1) is a hydrocarbon system, that can be modelled directly by united atom potentials situated on each of the carbon atoms. The two bicyclooctane units are relatively rigid and provide a strongly anisotropic core for the molecule, this leads to a large mesophase range of 319 K - 520 K [75] in the real molecule.

The lack of strongly dipolar regions in the 5,5-BBCO molecule mean that no charge interactions are required, and so prohibitively expensive Ewald sums or reaction field calculations are avoided. The molecule also lacks aromatic regions. These are considerably harder to model than aliphatic regions. For example, the work of Claessens *et al.* [76] suggests that quadrupoles are needed to properly represent the interactions between benzene molecules. This can be done either by a point quadrupole in the centre of the ring, or by partial aromatic charges on carbons and hydrogens. Both

methods necessitate the use of the expensive Ewald sum method to calculate the long range interactions. Aliphatic hydrocarbons however require no such special treatment. All these factors together make 5,5-BBCO a highly suitable candidate molecule for atomistic modelling.

3.3 Computational Model

3.3.1 Force field

5,5-BBCO was modelled by a series of united atom potentials, (CH_3, CH_2, $C(sp^3)$), situated on each of the carbon atoms. The potential energy of the system was represented by a variant of the AMBER united atom force field [44] in which the bond lengths were fixed using the SHAKE procedure of Ryckaert (see section 2.3.3). The energy of the molecule in the force field was given by

$$E_{\text{total}} = \sum_{\text{angles}} \frac{k_\theta}{2}(\theta - \theta_{\text{eq}})^2 + \sum_{\text{dihedrals}} [1 + \cos(n\phi)] + \sum_{i<j} \left[\frac{A_{ij}}{{R_{ij}}^{12}} - \frac{B_{ij}}{{R_{ij}}^{6}} \right]. \quad (3.1)$$

Here, the bond bending term is modelled by a quadratic function where θ and θ_{eq} are actual and equilibrium bond angles, ϕ is a dihedral angle in a three term Fourier series, and the Lennard Jones coefficients are given by

$$A_{ij} = 4\epsilon_{ij}{\sigma_{ij}}^{12}, \quad (3.2)$$

and

$$C_{ij} = 4\epsilon_{ij}{\sigma_{ij}}^{6}. \quad (3.3)$$

Here ϵ_{ij} is the Lennard-Jones well-depth and σ_{ij} is the distance at which the potential is zero for atoms i and j. Interactions between unlike atoms can be obtained from the Lorentz-Berthelot mixing rules

$$\epsilon_{ij} = \sqrt{\epsilon_{ii}\epsilon_{jj}} \quad (3.4)$$

and

$$\sigma_{ij} = \frac{\sigma_{ii} + \sigma_{jj}}{2}. \tag{3.5}$$

The geometry of each bicyclooctane unit was fixed at its equilibrium values as determined by the molecular mechanics calculations using the MM3 force field [49]. Each of the sites were chargeless. All 1-4 non-bonded interactions were scaled by an empirical factor of 0.5 [43] which has the effect of 'softening' the steep repulsive Lennard Jones r^{-12} term, that was applied in the original fitting of the AMBER force field.

3.3.2 Force field parameters

The force field parameters were all taken from the AMBER force-field [43] and are listed in table 3.1.

3.3.3 Molecular dynamics simulations

The equations of motion were solved using a variant of the quaternion leap frog algorithm suitable for the integration of rigid body motion. This algorithm incorporates constraints between rigid bodies by using the QSHAKE procedure [77] (an extension to SHAKE [67]). The program DL_POLY_2.0 [78] was used throughout this study. A 2 fs time-step was employed. All production runs were carried out in the NVT ensemble using the Nosé-Hoover thermostat [79] coupled to translational and (rigid body) rotational motion. A 7 Å cutoff was employed for nonbonded interactions along with long range corrections for the energy and the virial for $r_{ij} > 7$ Å. A Verlet neighbour list [59] was used to speed up the expensive computation of intermolecular forces. The calculations were carried out on systems of 64 and 125 molecules.

bond	bond length / Å
C-C	1.526

bond angle	K_θ/kJ mol^{-1}rad^{-2}	θ_{eq}/°
CH_2-C-CH_2	167.36	109.5
CH_2-CH_2-CH_2	263.592	112.4
CH_2-CH_2-CH_3	263.592	112.4

Dihedral	$\frac{V_n}{2}$/kJ mol^{-1}	n	1-4 vdw scale factor
X-CH_2-CH_2-X	8.368	3	0.5
X-C-CH_2-X	2.791	3	0.5
X-C-C-X	0.6025	3	0.5

Non-bonded	ϵ / kJ mol^{-1}	σ / Å
C(sp3)	0.25104	3.2072
CH_2	0.50208	3.43
CH_3	0.62760	3.5636

Table 3.1: Force field data for 5,5-BBCO.

3.4 Results

3.4.1 Initial simulations

Simulations were started from a *fcc* array of aligned molecules inside a box at gas phase densities. This was rapidly compressed, using a Hoover barostat at a pressure of 1000 atm, to a density of 1115 kg m^{-3} to provide a pseudo nematic starting configuration using the procedure described in section 2.4. This in turn was equilibrated at a temperature of 500 K to provide an isotropic starting configuration. Simulations of 64 molecules starting from pseudo nematic and isotropic state points were carried out in parallel on separate workstations to provide a preliminary survey of the phase diagram.

Orientational order was monitored through the order parameter of equation 2.17. In equation 2.16, a number of choices are possible for the vector $\mathbf{u}_j$. The most useful features for characterising the order in 5,5-BBCO were found to be the axis vector associated with the core of the molecule (the two bicyclohexane units) and the long molecular axis calculated from diagonalising the inertia tensor (equation 2.16).

The time required for the decay of orientational order in the pseudo nematic system provided an initial pointer to the proximity of the system to a mesophase. For runs close to the isotropic-nematic phase transition, simulation times in excess of 4 ns were required for S_2 to decay to a value of less than 0.2. At similar temperatures in the isotropic phase the onset of fluctuations in S_2 were observed. These runs provided an initial estimate for the phase transition to an orientationally ordered phase of 330±50 K. Several longer runs were then carried out to attempt to demonstrate the thermodynamic stability of a mesophase by growing it directly from the isotropic liquid.

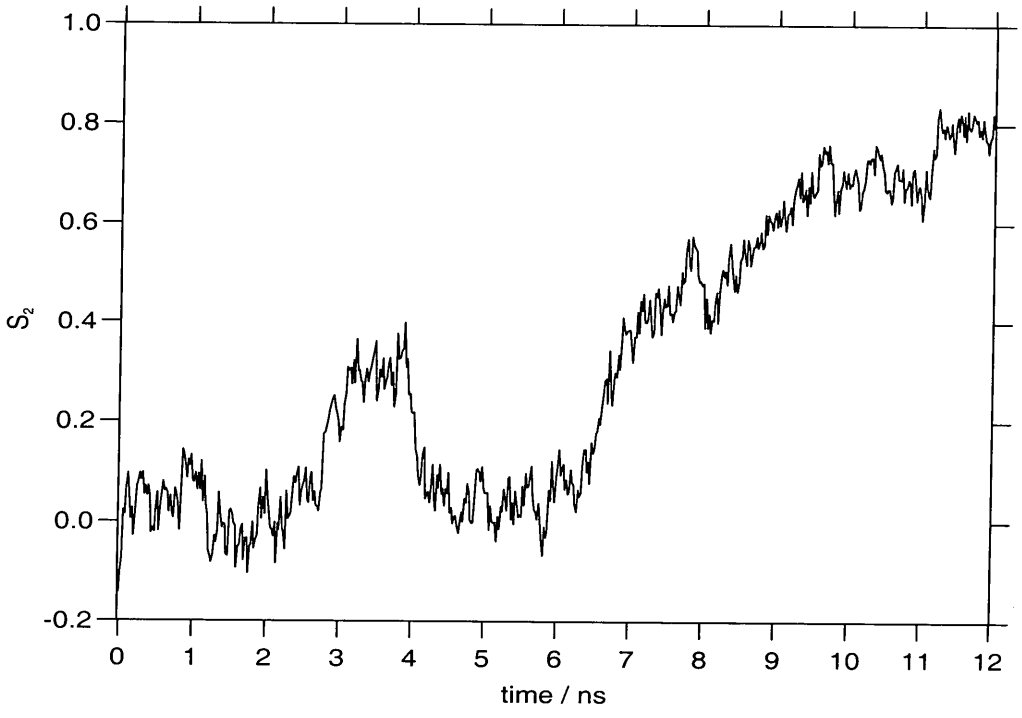

Figure 3.2: Order parameter S_2 for 64 molecules at 300 K

3.4.2 Demonstration of mesophase stability for 64 molecules

The growth of orientational order for a system of 64 molecules at 300 K is shown in figure 3.2. Growth in orientational order requires approximately 10 ns of simulation time at this temperature. Analysis of system snapshots for this run indicate that the fluctuations between 3-4 ns correspond to the growth of a single extended domain of ordered molecules within the isotropic phase. At longer times ($5 - 6$ ns) the decay of S_2 is due to the formation of multiple orientationally ordered domains with the domain directors pointing in different directions such that the overall order parameter remains close to zero. In the final equilibration period these domains coalesce to form a uniformly ordered sample. Analysis of an independent quench run at 330 K, shows a similar pattern, though in this case domains seem to form more rapidly and equilibration takes place in approximately 6 ns. A summary of equilibrated state-points is

$\langle T \rangle$ /K	no. of molecules	equilibration time / ns	production time / ns	$\langle S_2 \rangle$
500	64	0.5	1.5	0.21 ± 0.01
400	64	7	2	0.25 ± 0.02
360	64	2	2	0.49 ± 0.03
330	64	6	2	0.49 ± 0.04
300	64	10	2	0.73 ± 0.02
300	125	6.5	1.5	0.64 ± 0.02
250	125	8 (at 300 K)	1	0.74 ± 0.02
		1 (at 250 K)		
200	125	2 (at 250 K)	1	0.78 ± 0.02
		1 (at 200 K)		

Table 3.2: Summary of simulation data for 5,5-BBCO. (Quoted values for the orientational order parameter S_2 are for the molecular long axis vector obtained from equation 2.21.)

given in table 3.2.

Monitoring of the diffusion constant for two additional short simulations at 200 K and 150 K indicated that the system was frozen at these temperatures.

3.4.3 Simulations of a 125 molecule system

After the successful growth of a mesophase for 64 molecules, simulations were carried out for a larger system of 125 molecules in a periodic box of dimensions 1:1:1.6, with the aim of characterising the nature of the mesophase. The simulations were started from a fully aligned pseudo nematic system with randomly selected position vectors

for molecular centres of mass, and 7 ns were allowed for initial equilibration at 300 K. Three temperatures were studied in all (300 K, 250 K and 200 K) and full details are given in table 3.2. The 125 molecule system remained fluid for all 3 temperatures. There was some system size dependency found in the order parameter values at 300 K (when compared to the 64 molecule simulation at this temperature) as one would predict for these relatively small systems.

3.4.4 Phase characterisation

Careful monitoring of $S_{\mathrm{CM}}(\mathbf{k})$ (equation 2.24) throughout the simulations for each temperature indicated the absence of significant peaks at low wavevectors and the mesophase was therefore assigned to be nematic. Translational order was also monitored through the centre of mass radial distribution function $g(r)$ (equation 2.22). $g(r)$ was also resolved parallel ($g_{||}(r)$) and perpendicular ($g_{\perp}(r)$) to the director $\mathbf{n}$, (obtained from the diagonalisation of equation 2.17), to check for signs of smectic ordering. To allow for spatial fluctuations in $\mathbf{n}$, a new director was used for each set of coordinate data used in the compilation of $g_{||}(r)$. The radial distribution function for the molecular centre of mass in the isotropic and nematic phases are plotted in figures 3.3 and 3.4. The change in phase is characterised by a moderate growth in the size of the first solvation peak in $g(r)$. However, $g_{||}(r)$ remains flat and there is no indication of the periodic ordering of molecules into smectic layers. There is also no significant growth in the first solvation peak of $g_{\perp}(r)$ beyond what is expected for normal short range order within a nematic. Significant growth in this peak is expected when molecules exhibit strong local ordering as a precursor to smectic layer formation [80]. In figures 3.5 and 3.7 snapshots from the simulations at 250 K (nematic) and 400 K (isotropic) are plotted. The molecular long axis vectors are derived from equation 2.21. The snapshots

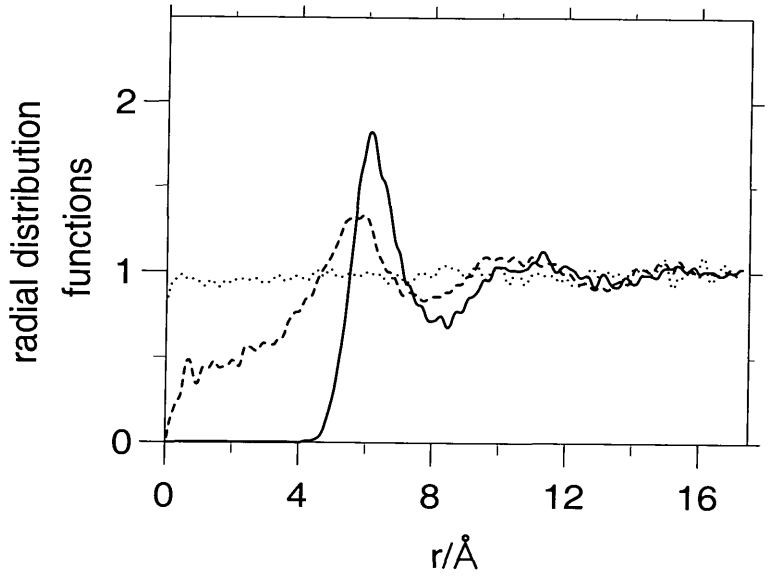

Figure 3.3: Radial distribution functions for the molecular centre of mass, at 250 K (nematic phase). Bold line – $g(r)$, dotted line – $g_{||}$, dashed line – $g_{\perp}$.

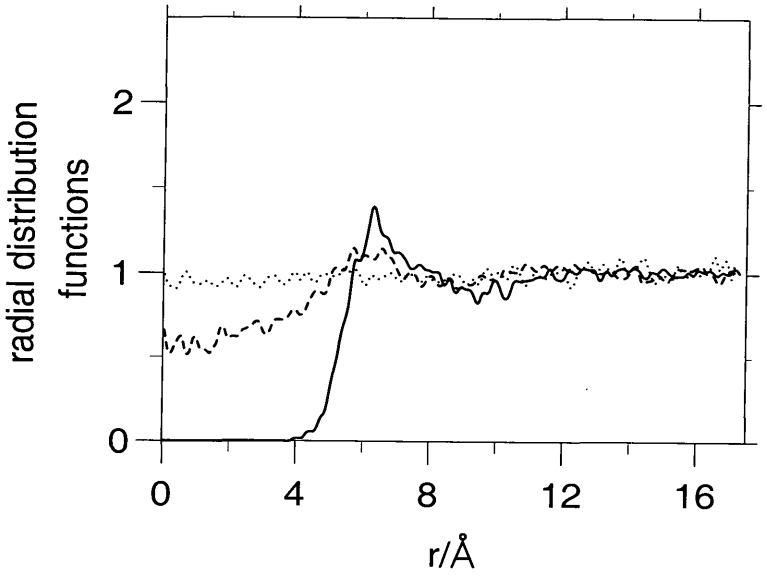

Figure 3.4: Radial distribution functions for the molecular centre of mass, at 400 K (isotropic phase, pretransitional region). Bold line – $g(r)$, dotted line – $g_{||}$, dashed line – $g_{\perp}$.

confirm the phase assignments made above and confirm local short range translational predicted from $g_{\perp}(r)$. It is seen that molecules are able to sample a wide range of conformations in the mesophase (see figures 3.6 and 3.8), and this will be discussed in detail in section 3.4.6. MD movies made from sequential snapshots confirm that that molecular conformational changes occur in the mesophase down to 200 K.

3.4.5 Search for smectic phases

Experimentally 5,5-BBCO is seen to form a uniaxial smectic phase [75]. However, in this study only a nematic phase was seen. To check if the absence of a smectic phase was influenced by the fixed periodic boundary conditions, preliminary simulations were carried out for different box dimensions for the 125 molecule system. For the original box dimensions of 1:1:1.6. The length of the z-axis corresponds to slightly less than 3 molecular lengths for molecules in an all-*trans* conformation. Simulations for box dimensions of up to 1:1:2 (with the z-axis significantly longer than 3 molecular lengths) also showed no evidence for the growth of smectic layers. The director was able to fluctuate during the course of the simulation and there was no evidence of any preferred director orientations induced by the presence of the periodic boundaries. Preliminary simulations were also carried out in the NpT ensemble. Here the box lengths were able to fluctuate independently and thereby accommodate the formation of smectic layers without favouring particular layer spacings. However, for the NpT runs it was found that the Hoover barostat produced large density fluctuations for the small system sizes studied here. These runs were therefore not pursued further. Limits on computer time also restricted the study of phase behaviour below 200 K for 125 molecules, where molecular reorientation was found to be particularly slow.

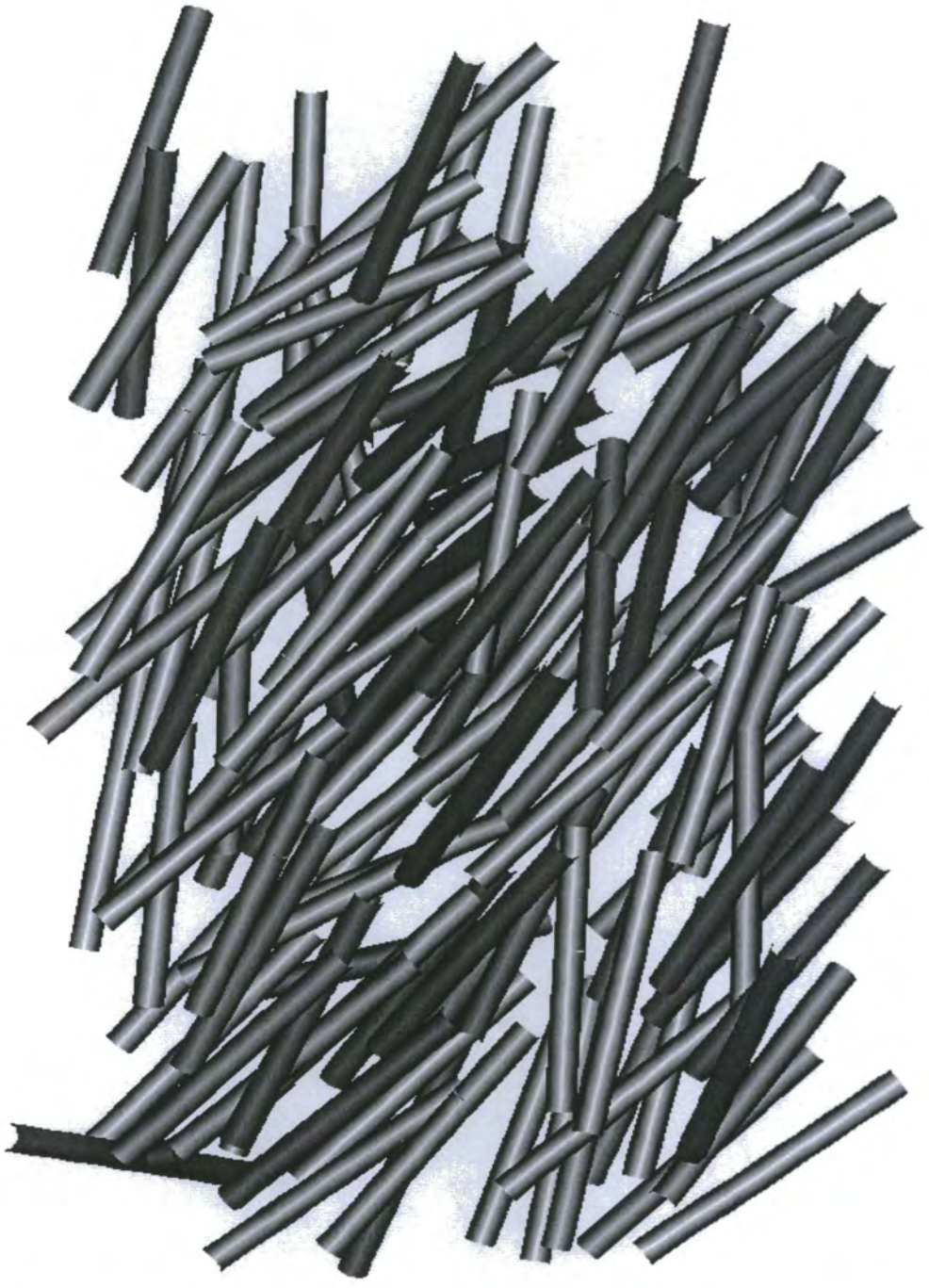

Figure 3.5: Snapshot of the 125 molecule system at 250 K in the nematic phase, showing the molecular long axis derived from the inertia tensor.

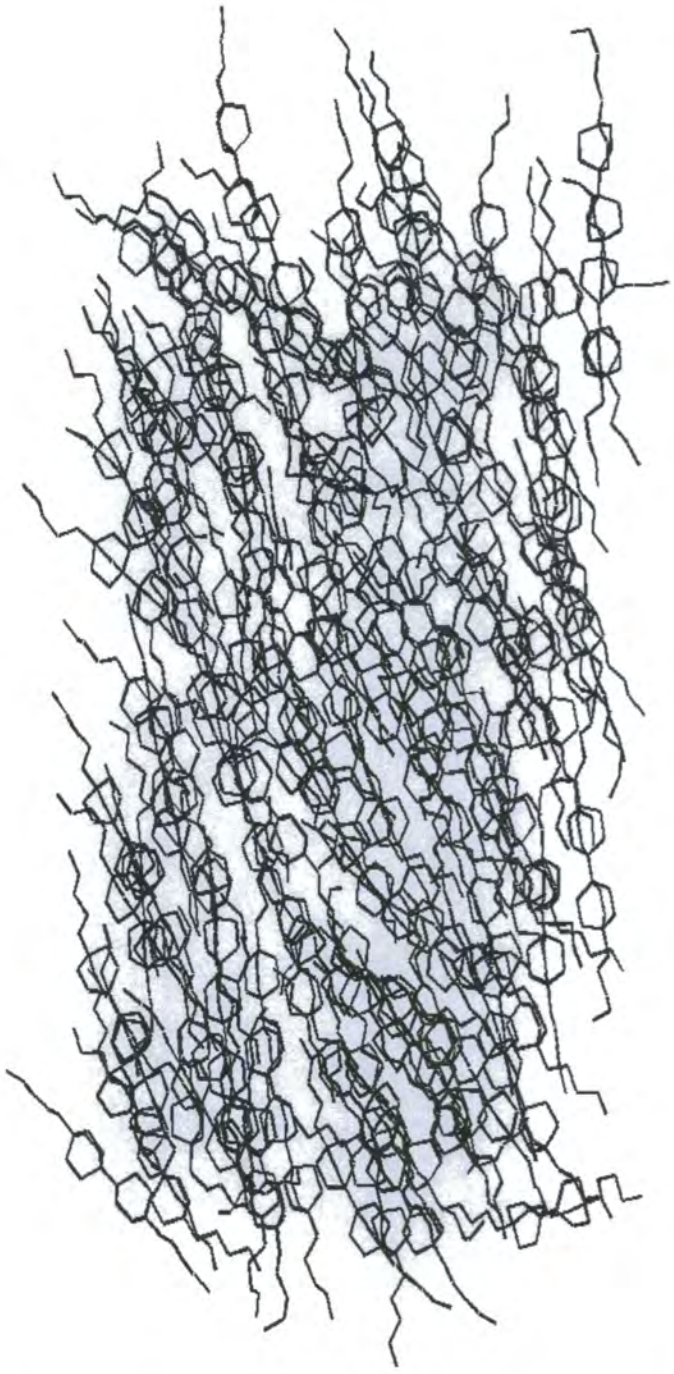

Figure 3.6: Snapshot of the 125 molecule system at 250 K in the nematic phase, showing molecular order.

Figure 3.7: Snapshot of the 64 molecule system at 400 K in the isotropic phase, showing the molecular long axis derived from the inertia tensor.

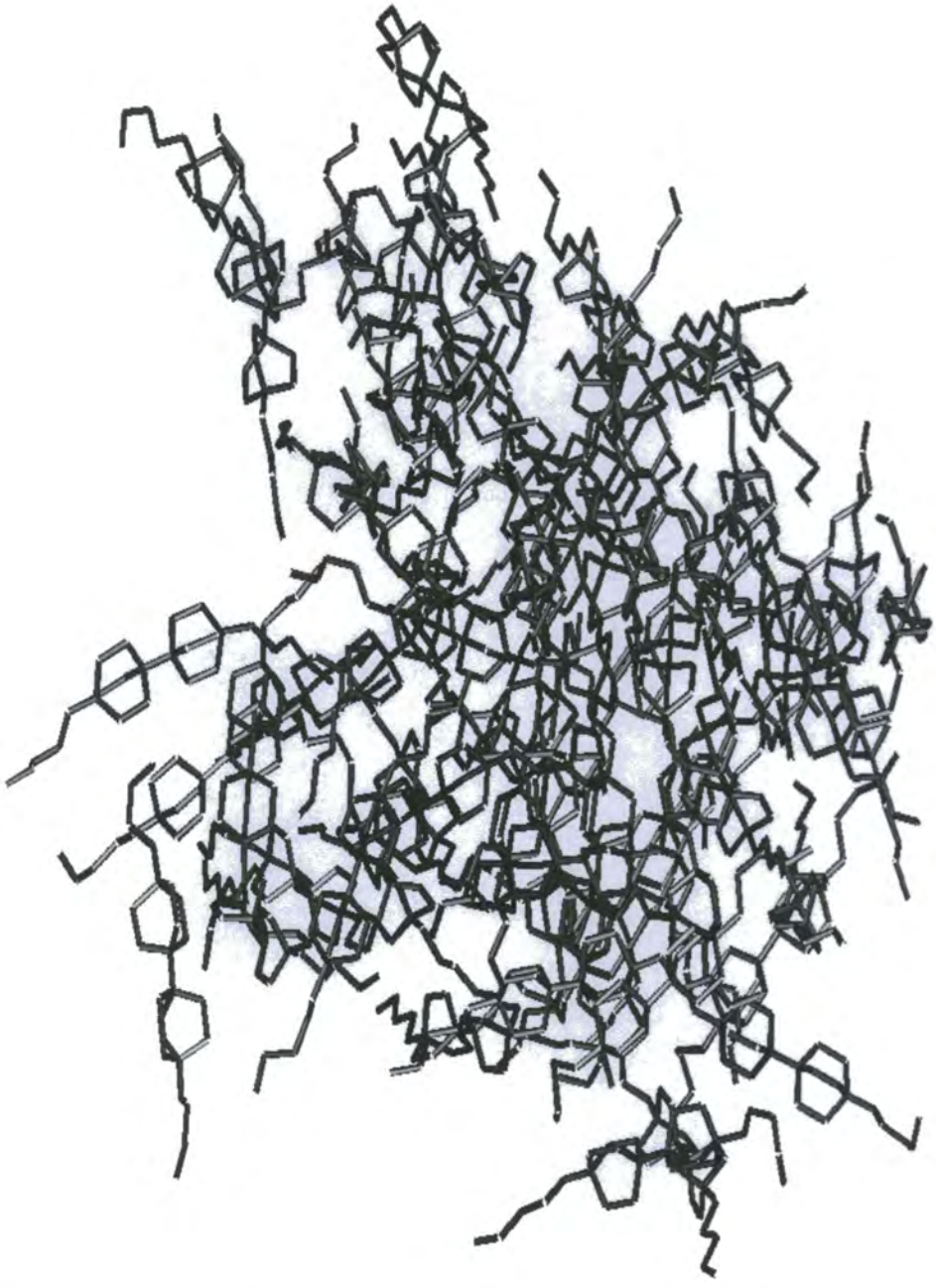

Figure 3.8: Snapshot of the 64 molecule system at 400 K in the isotropic phase, showing molecular order.

3.4.6 Dihedral angle populations

The *gauche/trans* dihedral angle populations are reported in table 3.3. For the nematic phase internal rotation about ω effectively stops but the molecules are still able to sample all major conformations by concerted changes in the two δ dihedral angles. For the three dihedrals α, β, γ in the alkyl chain a classic odd even effect is observed with *gauche* conformations most favoured for the dihedral β. This effect has also been observed in simulations of *trans*-4-(*trans*-4-n-pentylcyclohexyl)cyclohexylcarbonitrile (CCH5) [24] and 4-n-pentyl-4'-cyanobiphenyl (5CB) [34]. In the nematic phase there is a strong coupling between molecular conformation and the orientational mean field arising from neighbouring molecules in the fluid. The effect of this is to promote those conformations in which the molecule remains linear. Consequently for $\alpha\ \beta\ \gamma$, the conformations tg_+t, tg_-t are favoured over g_+tt, g_-tt, which are in turn favoured over ttg_+ and ttg_-. Local orientational ordering in anisotropic systems means that these preferences are also seen in the isotropic phase, but to a much smaller extent.

3.4.7 Effective torsional potentials

In figures 3.9, 3.10, 3.11 and 3.12 dihedral angle distribution functions $\Gamma(\phi)$ are plotted for the chain dihedrals α, β, γ and δ. The odd-even effect is again seen in these curves as is the strong temperature dependence of $\Gamma(\phi)$. To remove the influence of temperature in comparing the behaviour of dihedral angles in different phases the dihedral angle distribution is written in the following form [24]

$$\Gamma(\phi) = C \exp\left[-\frac{V(\phi)}{k_{\mathrm{B}}T}\right] \tag{3.6}$$

where C is a normalisation factor and $V(\phi)$ is an effective torsional potential or conformational free energy. $V(\phi)$ is composed of intramolecular contributions to the torsional energy, V_{int}, and an intermolecular part V_{ext}, that can be used to measure the influ-

Dihedral	T/K	N_{mol}	g^-/%	t/%	g^+/%
α	500	64	19.88	60.57	19.57
α	400	64	16.94	66.16	16.90
α	300	125	11.86	74.88	13.25
α	250	125	10.54	80.66	8.80
α	200	125	6.09	87.72	6.18
β	500	64	22.41	55.90	21.69
β	400	64	21.81	57.47	20.72
β	300	125	18.04	63.01	18.95
β	250	125	18.28	63.46	18.26
β	200	125	17.12	67.76	15.12
γ	500	64	16.00	68.18	15.82
γ	400	64	14.50	72.59	12.91
γ	300	125	8.04	84.44	7.52
γ	250	125	4.40	91.12	4.47
γ	200	125	3.32	93.57	3.11
δ	500	64	34.48	33.23	32.28
δ	400	64	33.88	33.66	32.47
δ	300	125	37.53	36.42	26.05
δ	250	125	33.55	40.08	26.37
δ	200	125	33.54	41.50	24.96
ω	500	64	27.36	39.66	32.98
ω	400	64	29.69	35.94	34.38
ω	300	125	0	100.0	0
ω	250	125	0	100.0	0
ω	200	125	0	100.0	0

Table 3.3: *Gauche* and *trans* dihedral angle populations.

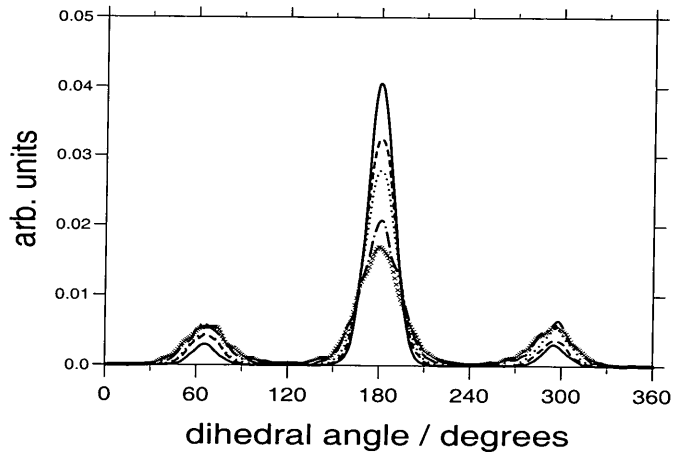

Figure 3.9: Dihedral distribution for torsional angle α. Crosses - 500 K (isotropic phase), dot-dashed line - 400 K (isotropic phase), dotted line - 300 K (nematic phase), dashed line - 250 K (nematic phase), bold line - 200 K (nematic phase).

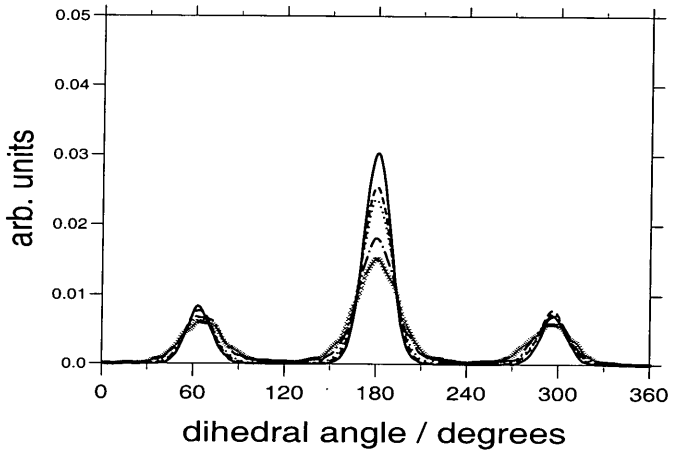

Figure 3.10: Dihedral distribution for torsional angle β. Crosses - 500 K (isotropic phase), dot-dashed line - 400 K (isotropic phase), dotted line - 300 K (nematic phase), dashed line - 250 K (nematic phase), bold line - 200 K (nematic phase).

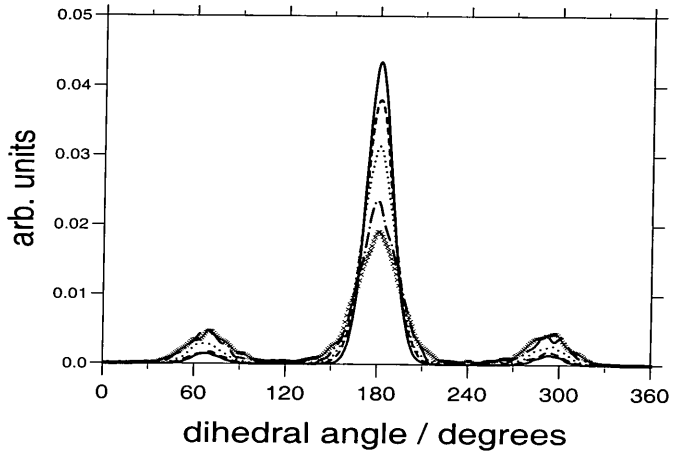

Figure 3.11: Dihedral distribution for torsional angle γ. Crosses - 500 K (isotropic phase), dot-dashed line - 400 K (isotropic phase), dotted line - 300 K (nematic phase), dashed line - 250 K (nematic phase), bold line - 200 K (nematic phase).

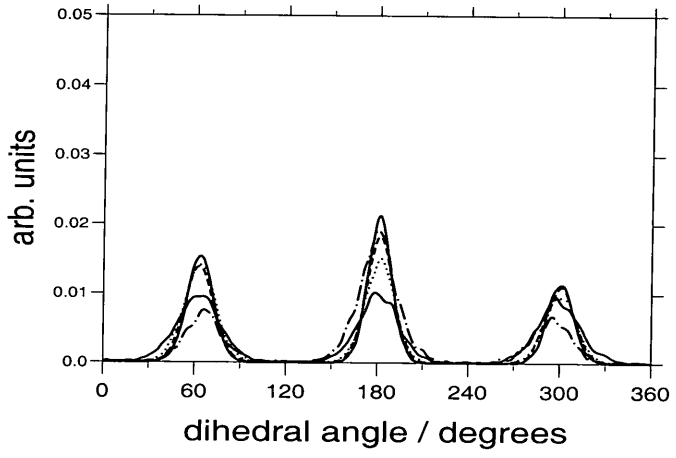

Figure 3.12: Dihedral distribution for torsional angle δ. Crosses - 500 K (isotropic phase), dot-dashed line - 400 K (isotropic phase), dotted line - 300 K (nematic phase), dashed line - 250 K (nematic phase), bold line - 200 K (nematic phase).

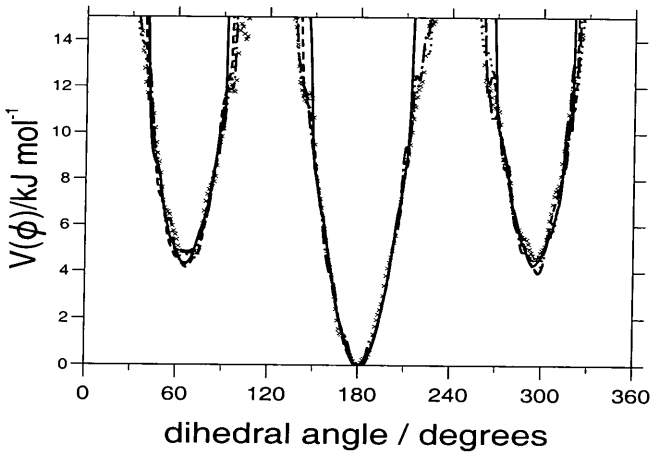

Figure 3.13: Effective torsional potential for torsional angle α. Crosses - 500 K (isotropic phase), dot-dashed line - 400 K (isotropic phase), dotted line - 300 K (nematic phase), dashed line - 250 K (nematic phase), bold line - 200 K (nematic phase).

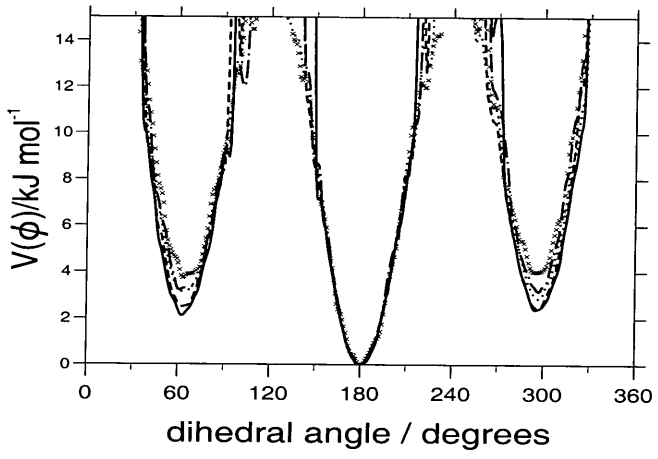

Figure 3.14: Effective torsional potential for torsional angle β. Crosses - 500 K (isotropic phase), dot-dashed line - 400 K (isotropic phase), dotted line - 300 K (nematic phase), dashed line - 250 K (nematic phase), bold line - 200 K (nematic phase).

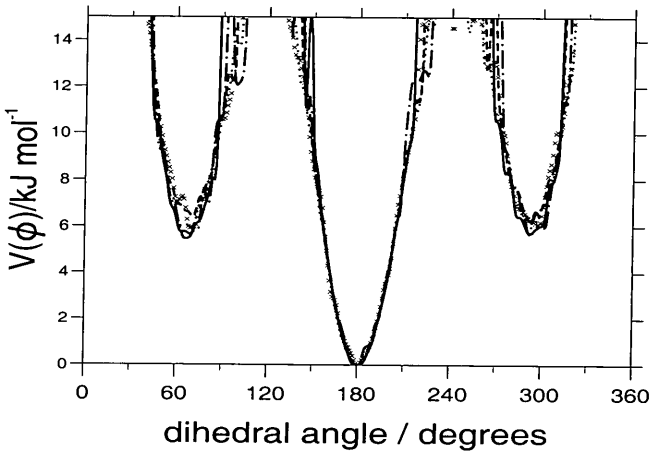

Figure 3.15: Effective torsional potential for torsional angle γ. Crosses - 500 K (isotropic phase), dot-dashed line - 400 K (isotropic phase), dotted line - 300 K (nematic phase), dashed line - 250 K (nematic phase), bold line - 200 K (nematic phase).

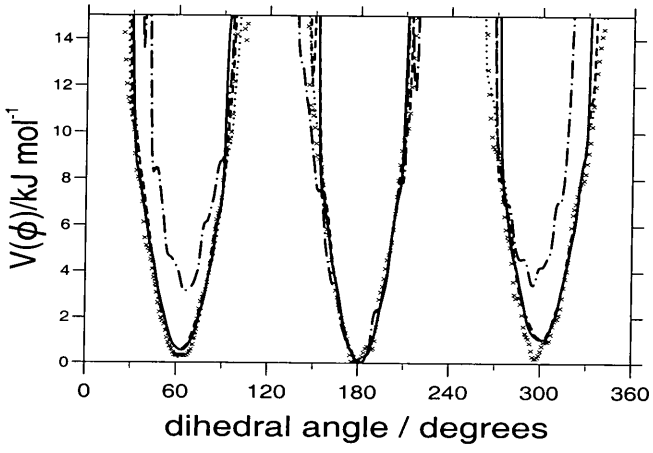

Figure 3.16: Effective torsional potential for torsional angle δ. Crosses - 500 K (isotropic phase), dot-dashed line - 400 K (isotropic phase), dotted line - 300 K (nematic phase), dashed line - 250 K (nematic phase), bold line - 200 K (nematic phase).

Conformer	% at 400 K	% at 300 K	% at 250 K
ttt	17.9	29.9	34.9
tgt	9.8	11.7	15.4
gtt	6.2	5.9	5.0
ttg	5.6	4.4	3.2

Table 3.4: Most populated conformers for chain dihedrals $\alpha\beta\gamma$.

ence of molecular environment on molecular structure. Figures 3.13-3.16 show values of $V(\phi)$ computed from equation 3.6 for α, β, γ and δ. To within statistical errors there is no significant difference in $V(\phi)$ for the odd dihedrals α and γ. However, for β a clear reduction in the energy difference between *gauche* and *trans* conformations $\Delta_{E_{gt}}$ is seen as the temperature is reduced. This can be directly attributed to the effects of the nematic mean field reducing the energy of conformations in which molecules remain linear. This is seen clearly in table 3.4 where the growth in populations of *ttt* and *tgt* conformers occurs at lower temperatures when orientational order is high. These results are consistent with molecular field theory. For 4-n-alkyl-4'-cyanobiphenyl mesogens 5CB (C_5 chain) and 8CB (C_8 chain) molecular field theory predicts an enhancement in populations for linear conformers [25,81] with increasing order parameter, and these results have been used to successfully interpret quadrupolar couplings from NMR studies of the deuterated compounds [82].

In this work $\Delta_{E_{gt}}$ changes by approximately 2 kJ mol^{-1} over the temperature range studied. This is comparable to the values of $\Delta_{E_{gt}}$ reported in table VI of reference [80], though in the latter case the conformations which were accessible in the mesophase favoured an *increase* in the *gauche/trans* energy gap of this magnitude. Sampling of conformations at the energy barriers is sparse, consequently it was not possible to ac-

$\langle S_2 \rangle$	400 K	300 K	250 K	200 K
bond 1	0.04	0.26	0.38	0.47
bond 2	0.01	0.01	0.03	0.03
bond 3	0.11	0.41	0.53	0.57
bond 4	0.01	-0.01	0.02	0.00
bond 5	0.22	0.58	0.68	0.70
bond 6	0.23	0.61	0.70	0.74
Inertia tensor	0.25	0.64	0.74	0.78

Table 3.5: Order parameters for bonds in 5,5-BBCO. (Bonds labels are defined in figure 3.1.)

curately measure the energy barrier for rotation between *gauche* and *trans* conformers. Hence the graphs of $V(\phi)$ are truncated at 15 kJ mol^{-1} in the figures.

3.4.8 Bond order parameters

Bond order parameters for the alkyl chain (table 3.5) exhibit an odd-even effect which arises due to the preference for the *all-trans* conformation in which successive bonds alternately lie parallel and at an angle to the molecular long axis. Bonds lying along the molecular long axis have the highest order parameters. For homologous series of molecules with different alkyl chain lengths this can lead to a strong odd-even effect in transition temperatures. For 4,4′-di-alkyl-bibicyclo[2.2.2]octanes this is seen in the reported crystal melting temperatures [75] but not in the clearing temperatures. The latter rise to a maximum of 520 K for 5,5-BBCO. At these elevated temperatures the influence of the *all-trans* conformation is much reduced. In this work, the percentage of *all-trans* conformations in the isotropic phase drops to a value of 16.8% at 500 K.

The reduction in *all-trans* populations is likely to diminish the importance of odd-even ordering of individual bonds in determining the clearing temperatures for the real materials.

3.4.9 Molecular Reorientation

The reorientational motion of the long molecular axis defined by diagonalisation of equation 2.21 was characterised by the reorientational correlation functions C_l (equation 2.28). For linear molecules in a liquid phase, C_l can be described by the cumulant expansion, which relates the behaviour of C_l to the angular velocity autocorrelation function C_ω [83–85]

$$C_l(t) \approx \exp\left[-\frac{-l(l+1)k_bT}{I}\int_0^t (t-\tau)C_\omega(\tau)d\tau\right], \tag{3.7}$$

with

$$C_\omega(t) = \frac{\langle \omega_i(0)\cdot\omega_i(t)\rangle}{\langle \omega_i(0)^2\rangle} \tag{3.8}$$

where ω_i is the angular velocity of molecule i. For short times, where $C_\omega \approx 1$, equation 3.7 becomes

$$C_l(t) \approx \exp\left[-\frac{l(l+1)k_bT}{2I}t^2\right]. \tag{3.9}$$

For long time-scales, where $t \gg \tau_\omega$, this relation reduces to the Debye equation

$$C_l(t) = \exp[-l(l+1)D_Rt] \tag{3.10}$$

where D_R is the rotational diffusion coefficient. The Debye model assumes that molecular reorientation results from many uncorrelated angular displacements leading to a single exponential decay of C_l. If the approximation holds true then a plot of $\ln C_l(t)/(-l(l+1))$ against t would result in the curves for different l being coincident for all times.

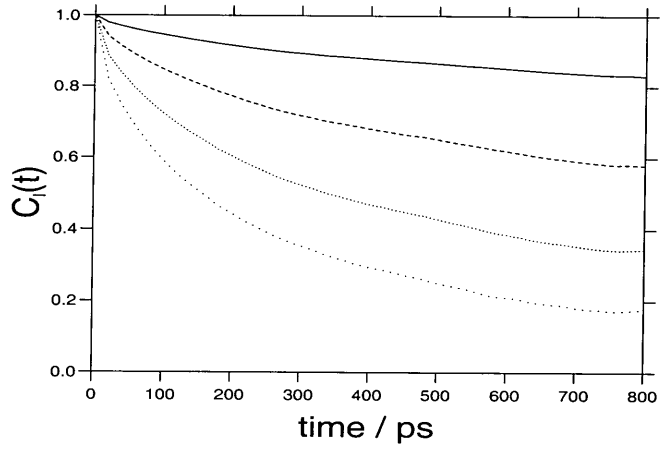

Figure 3.17: Reorientational correlation functions: P_1 bold line; P_2 dashed line; P_3 dotted line (closely spaced dots); P_4 dotted line (widely spaced dots), for the nematic phase (300 K)

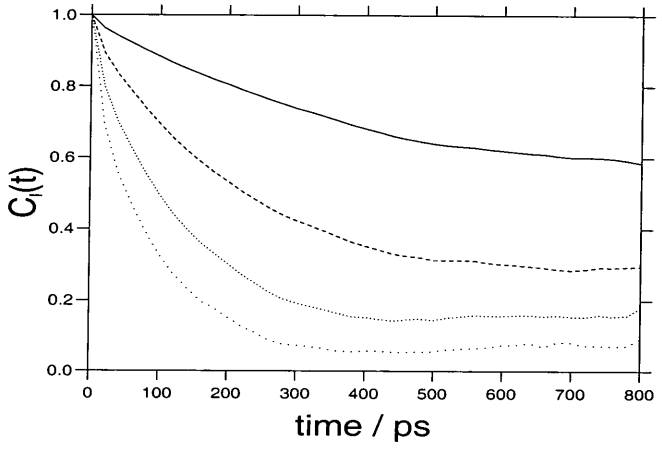

Figure 3.18: Reorientational correlation functions: P_1 bold line; P_2 dashed line; P_3 dotted line (closely spaced dots); P_4 dotted line (widely spaced dots), for the isotropic phase (400 K)

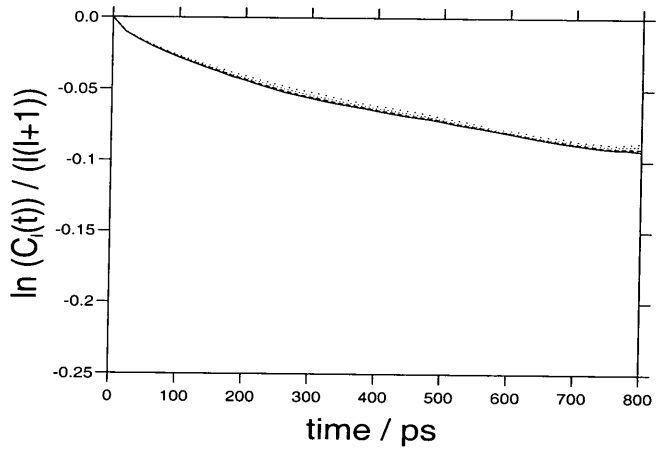

Figure 3.19: Reorientational correlation functions: P_1 bold line; P_2 dashed line; P_3 dotted line (closely spaced dots); P_4 dotted line (widely spaced dots), for the nematic phase (300 K)

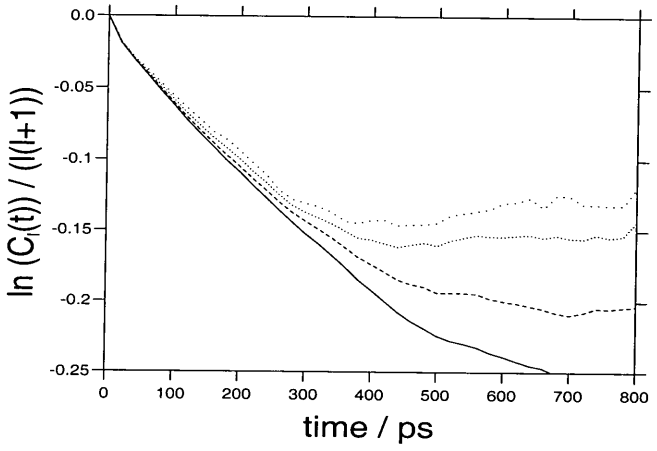

Figure 3.20: Reorientational correlation functions: P_1 bold line; P_2 dashed line; P_3 dotted line (closely spaced dots); P_4 dotted line (widely spaced dots), for the isotropic phase (400 K)

The decay of C_l for $l = 1,4$ is plotted in figures 3.17 and 3.18. It is seen that the decay of C_1 is *extremely slow* particularly in the nematic phase (figure 3.17). The behaviour of C_l is qualitatively similar to that seen in small linear molecules [74], though the time-scales involved are much longer for 5,5-BBCO. The Debye model appears to hold well for the isotropic phase for $t < 200$ ps (figure 3.20). However, at times $t > 200$ ps in the isotropic phase the $\ln C_l(t)/(l(l+1))$ curves fan out considerably. This behaviour represents the break down of the Debye model. In the cumulant expansion this behaviour is usually attributed to the neglect of higher order cumulants in equation 3.9. For the nematic phase in figure 3.20, the curves of $\ln C_l(t)/(l(l+1))$ are all coincident, suggesting that the cumulant expansion also works well for the time scales studied. However, in this case molecular reorientation is so slow that most molecules are performing rotational diffusion close to their original positions.

To test whether or not molecular conformational changes can make a major contribution to the orientation of the molecular long axis the behaviour of C_l was calculated, where $\mathbf{u}$ in equation 2.28 is now defined by the vector representing the long axis of the rigid core of 5,5-BBCO. It is found that the reorientational behaviour of the molecular core is very similar to that of the long axis as defined by the inertia tensor. This indicates that there is no significant coupling between conformational changes in the flexible alkyl chain and reorientational motion of the molecule as a whole.

3.5 Discussion

3.5.1 Equilibration times

It is informative to compare equilibration times with other model systems. Wilson [80] has performed simulations of a hybrid Gay-Berne/Lennard Jones liquid crystal dimer, in which two Gay-Berne particles are linked via a flexible alkyl chain. For 512 such

molecules, approximately 6 ns (3×10^6 time steps) are required for a smectic-A phase to grow from the isotropic fluid. The lengths of run required for flexible models of this type contrast strongly with those for single site potentials. For MD simulations of the Gay-Berne potential growth of a mesophase from the isotropic fluid typically requires $1 - 2 \times 10^5$ time steps t^*, where $t^* = \sqrt{(\epsilon_0/(m\sigma_0^2))}t \approx 0.0015$. From the work of La Penna et al. [86] it is possible to estimate typical mesogenic values for $\epsilon_0/k_B = 407$ K, $\sigma_0 = 5.7$ Å, and molecular mass $m = 7.5 \times 10^{-15}$ kg mol^{-1} for the Gay-Berne potential based on the mesogen para-azoxyanisole (PAA). These data produce a value for t of 7.5 fs which is in the range typically used for the integration of motion for (rigid) molecules. This suggests that the reason for the relatively slower equilibration times for atomistic model mesogens is partly due to the small time step required to integrate internal motion and partly down to the slowness of molecular reorientation for flexible molecules.

3.5.2 Comparison with the Real system

In the reported phase behaviour for the real material [75], 5,5-BBCO exhibits a melting point at 319 K and a clearing point of 520 K, both higher than those indicated by the united atom model of 5,5-BBCO studied in this chapter. Also this study found no evidence for smectic stability, whilst the experimental system exhibits a uniaxial smectic phase. There are several possible reasons for these discrepancies. Firstly, small size simulations are known to exhibit considerable hysteresis at first order phase transitions for simpler models such as the Gay-Berne potential (section 1.3.2). It is only when system size approaches 1000 molecules that its influence on phase transition temperature becomes small. Secondly, recent work by Jorgensen [44] and others have demonstrated that the AMBER inter molecular potential functions used in this study

can be improved upon for simulating simple liquids. It is these functions that will have the largest influence on transition temperatures. Finally, the cutoff of 7 Å for nonbonded interactions is close to the minimum that can be safely used in accurate atomistic work. If computational resources had allowed, it would have been interesting to extend the nonbonded cutoff to larger distances to determine if this had any influence on the formation of smectic structures.

3.6 Conclusions

Simulations have been carried out for systems of 64 and 128 molecules of the mesogen 4,4′-di-n-pentyl-bibicyclo[2.2.2]octane (5,5-BBCO) for simulation times of up to 12 ns. Spontaneous growth of a liquid crystal mesophase from an isotropic liquid has been observed in two independent runs which required respectively 10 ns and 6 ns for the orientational order parameter to equilibrate. These simulations are considerably longer than any previous runs for atomistic mesogens, and represent the first fully atomistic simulations to conclusively demonstrate the growth of a mesophase directly from an isotropic liquid.

The results have shown strong coupling between molecular order and internal molecular structure. A classic odd-even effect has been observed in both bond order parameters and in the relative populations of *gauche* conformers in the alkyl chain. Molecular reorientation of the long molecular axis was found to be extremely slow in these systems; particularly in the nematic phase. No significant coupling was found between molecular conformational changes and the reorientation of the long molecular axis defined by the inertia tensor. In the reported phase behaviour for the real material [75], 5,5-BBCO exhibits a melting point at 319 K and a clearing point at 520 K, both higher than those indicated by the united atom model for 5,5-BBCO.

CHAPTER 4

Simulation of Liquid Crystals using a Hybrid Lennard-Jones/Gay-Berne Model

4.1 Introduction

The simulations of 4,4′-di-n-pentyl-bibicyclo[2.2.2]octane in chapter 3 illustrated how computationally expensive atomistic modelling of liquid crystals is at the current time. Even when united atom models are used to eliminate some atomic sites from the simulation, system sizes are limited to 100-200 molecules at the most. However, for smectic phases it would be highly desirable to be able to simulate several hundred or (ideally) several thousand molecules to look at the ordering of molecules in layers. In this chapter the computational burden of simulating the many pairwise nonbonded interactions associated with the rigid core of a mesogen is reduced by replacing the core by a single-site Gay-Berne potential.

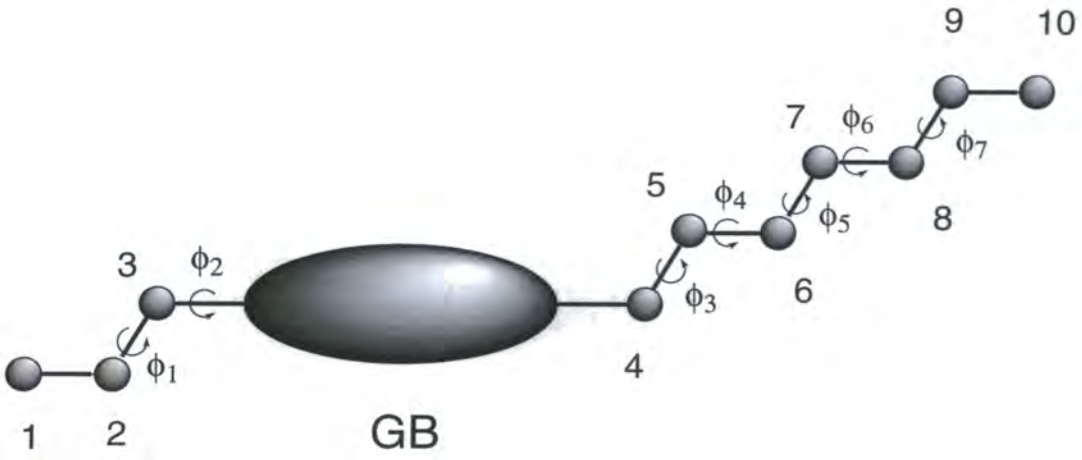

Figure 4.1: Schematic representation of the molecular model of C_3-GB-C_7, ϕ_i corresponds to dihedral angle i.

4.2 Computational model

The computational model to be investigated is based on a common group of mesogens consisting of rigid molecular core with two alkyl chains of unequal length at each end of the molecule [87–90]. The core unit of our mesogen is made from a single-site Gay-Berne potential. This Gay-Berne potential is flanked by C_3 and C_7 flexible alkyl chains made up from Lennard-Jones 12:6 potentials situated on the CH_2 and CH_3 united atoms. A schematic diagram of this (C_3-GB-C_7) model is shown in figure 4.1. The force field for this model is written as

$$\begin{aligned} E &= \sum_{i=1}^{N_{\text{angles}}} \frac{k_i}{2}(\theta_i - \theta_i^o)^2 \\ &+ \sum_{i=1}^{N_{\text{dihedrals}}} a_1(1+\cos\phi_i) + a_2(1-\cos(2\phi_i)) + a_3(1+\cos(3\phi_i)) \\ &+ \sum_{i=1}^{N_{\text{LJ}}}\sum_{j>i}^{N_{\text{LJ}}} U_{ij}^{\text{LJ}} + \sum_{i=1}^{N_{\text{GB}}}\sum_{j>i}^{N_{\text{GB}}} U_{ij}^{\text{GB}} + \sum_{i=1}^{N_{\text{LJ}}}\sum_{j=1}^{N_{\text{GB}}} U_{ij}^{\text{LJ/GB}}. \end{aligned} \tag{4.1}$$

In equation 4.1, N_{angles}, $N_{\text{dihedrals}}$, N_{LJ} and N_{GB} are respectively the number of angles, number of dihedral angles, number of Lennard-Jones sites and number of Gay-Berne sites in the system. The bond lengths in the model were fixed at 1.53 Å between LJ sites, and 6.37 Å between the Gay-Berne and LJ sites. A harmonic potential is

used to model bond angle deformation, where k_i is a bond angle force constant and θ_i and θ_i^o are actual and equilibrium bond angles. The values of k_i, θ_i^o and a_n are given in table 4.1. The parameters used to model the alkyl chains are obtained from the work of Jorgensen *et al.* [91] and Siepmann *et al.* [92], who have successfully simulated linear hydrocarbon chains. Gay-Berne sites are bonded via their centre of mass. One additional harmonic angle term is required for each site bonded to a Gay-Berne particle to prevent free rotation of Gay-Berne sites about their centres [80]. These terms involve the angle between the long axis of the Gay-Berne particle and the bond between the Gay-Berne site and the Lennard-Jones site to which it is attached. For these angles $\theta^o = 180°$, and the force constant is set at the value for a C-C-C bond angle. A single dihedral spans the Gay-Berne site (ϕ_2) to provide a coupling between the two chains. This interaction has two-fold symmetry, with $a_2/k_b = 892.71$ K, to mimic the effects of a typical phenyl ring-alkyl chain dihedral, where the barrier to rotation is known to be of this form and magnitude [93].

The terms U_{ij}^{LJ}, U_{ij}^{GB}, $U_{ij}^{\mathrm{LJ/GB}}$ in equation 4.1 represent non-bonded interactions energies for two particles i and j. The interaction energy U_{ij}^{LJ} for an inter-particle separation r_{ij} is given by the Lennard-Jones 12:6 potential (equation 1.2), with values for $\epsilon_{ij}^{\mathrm{LJ}}$ and $\sigma_{ij}^{\mathrm{LJ}}$ given in table 4.1 [91,92]. The U_{ij}^{GB} term represents the orientational dependent interaction energy for two Gay-Berne particles [19,20]. The parameters for the Gay-Berne potential were those of de Miguel *et al.* [94]. In this form of the potential, $\mu = 2$, $\nu = 1$, the length to breadth ratio σ_{ee}/σ_{ss} is 3.0 and the ratio of well-depths for end-to-end and side-to-side particles $\epsilon_{ee}/\epsilon_{ss}$ is 1/5. $\sigma_0^{\mathrm{GB}} = \sigma_{ss}$, and $\epsilon_0^{\mathrm{GB/k_b}} = \epsilon_{ss}/k_b$ are set using the values given in table 4.1 obtained from the work of La Penna *et al.* [95] and Wilson [22].

The form used for the Gay-Berne/Lennard-Jones interaction, $U_{ij}^{\mathrm{LJ/GB}}$, is based on

bond	bond length / Å
C-C	1.53
C-GB	6.37

bond angle	$K_\theta/\times 10^{-20}$J rad^{-2}	$\theta_{eq}/^\circ$
C-C-C	86.294	114.0
GB-C-C	86.443	114.0

Dihedral	a_1/K	a_2/K	a_3/K
C-C-C-C	355.03	-68.19	791.32
GB-C-C-C	0.0	892.71	0.0

Non-bonded	(ϵ/k_b) / K	σ / Å
CH_2	47.0	3.93
CH_3	114.0	3.93
GB	406.51	4.721
LJ/GB	171.08	4.117
	mass/kg	moment of inertia/kg m^2
CH_2	0.2325×10^{-25}	
CH_3	0.2495×10^{-25}	
GB	2.9558×10^{-25}	0.2731×10^{-23}

Table 4.1: Force field data for C7-GB-C3.

the work of Cleaver *et al.* [96] who have generalised the Gay-Berne potential to cover non-equivalent particles. Accordingly,

$$U_{ij}^{\mathrm{LJ/GB}} = 4\epsilon_0^{\mathrm{LJ/GB}}[\epsilon^{\mathrm{LJ/GB}}]^{\mu}(\hat{\mathbf{u}}_j, \hat{\mathbf{r}}_{ij}) \times \left[\left(\frac{\sigma_0^{\mathrm{LJ/GB}}}{r_{ij} - \sigma^{\mathrm{LJ/GB}}(\hat{\mathbf{u}}_j, \hat{\mathbf{r}}_{ij}) + \sigma_0{}^{\mathrm{LJ/GB}}}\right)^{12} - \left(\frac{\sigma_0^{\mathrm{LJ/GB}}}{r_{ij} - \sigma^{\mathrm{LJ/GB}}(\hat{\mathbf{u}}_j, \hat{\mathbf{r}}_{ij}) + \sigma_0{}^{\mathrm{LJ/GB}}}\right)^{6}\right], \tag{4.2}$$

where, in the limit of one of the particles being spherical, gives:

$$\sigma^{\mathrm{LJ/GB}}(\hat{\mathbf{u}}_j, \hat{\mathbf{r}}_{ij}) = \sigma_0[1 - \chi\alpha^{-2}(\hat{\mathbf{r}}_{ij} \cdot \hat{\mathbf{u}}_j)^2]^{-1/2} \tag{4.3}$$

and

$$\epsilon^{\mathrm{LJ/GB}}(\hat{\mathbf{u}}_j, \hat{\mathbf{r}}_{ij}) = \epsilon_0[1 - \chi'\alpha'^{-2}(\hat{\mathbf{r}}_{ij} \cdot \hat{\mathbf{u}}_j)^2] \tag{4.4}$$

with

$$\frac{\chi}{\alpha^2} = \frac{l_j^2 - d_j^2}{l_j^2 + d_i^2} \tag{4.5}$$

and

$$\frac{\chi'}{\alpha'^2} = 1 - \left(\frac{\epsilon_{ee}}{\epsilon_{ss}}\right)^{\frac{1}{\mu}}. \tag{4.6}$$

In this model $\chi/\alpha^2 = 0.77027$, and $\chi'/\alpha'^2 = 0.55279$.

Spherical nonbonded cutoffs of 9.808 Å, 18.884 Å ($4 \times \sigma_0^{\mathrm{GB}}$), 16.468 Å ($4 \times \sigma_0^{\mathrm{LJ/GB}}$), were employed for each of the pairwise-interactions U_{ij}^{LJ}, U_{ij}^{GB}, $U_{ij}^{\mathrm{LJ/GB}}$. Many simulations of isolated Gay-Berne sites shift the non-bonded potential to allow the interaction energy to go smoothly to zero at the cutoff [97], and here the same approach is adopted. To speed computation a separate Verlet neighbour list [59] was employed for each of the three sets of interactions. In calculating the intramolecular contributions to U_{ij}^{LJ}, $U_{ij}^{\mathrm{LJ/GB}}$, U_{ij}^{GB} in equation 4.1 all interactions between 1-2, 1-3 and 1-4 bonded sites have been excluded.

4.3 Simulation procedure

The equations of motions were integrated using a form of the leap-frog algorithm suitable for anisotropic systems [64, 98]. Calculations were performed for a system of 512 molecules in the NVT ensemble using a time step of 2 fs. The bond lengths were fixed to a tolerance of 1.0×10^{-6} Å using the SHAKE procedure of Ryckaert [67]. The starting configurations were created from an initial array of identical molecules, each in the *all-trans* conformation, aligned along a single Cartesian axis of a cubic cell. Each molecule was given a random displacement from a *bcc* lattice point and 50 % of the molecules (chosen at random) were rotated by 180° about the short molecular axis passing through the molecular centres of mass. This configuration was then rapidly compressed by a process of isotropically scaling the coordinates and employing short MD runs until liquid densities were reached (see section 2.4). Two pseudo-nematic staring configurations were created, with densities of 751.092 and 970.411 kg m^{-3} and with nematic order parameters of $S_2 = 0.6037$ and $S_2 = 0.4605$ respectively. Atomic velocities were assigned from a Maxwell-Boltzmann distribution, and simulations were then carried out on these configurations at 200 K and 300 K respectively. The orientational order parameter, molecular diffusion coefficients and dihedral angle distribution were monitored throughout the simulations, and snapshots of the system were viewed periodically using the AVS software. The orientational order of the Gay-Berne particle was monitored using S_2 from equation 2.17, where θ (in equation 2.17) measures the angle between the long-axes of the Gay-Berne ellipsoid and the average orientation of the sample defined by the director $\mathbf{n}$. Translational ordering of the system was characterised via the radial distribution function, calculated from equation 2.22. After equilibration of the two trial runs, a series of shorter simulations were performed starting from the final configurations of the 'longer runs' in order to explore the phase

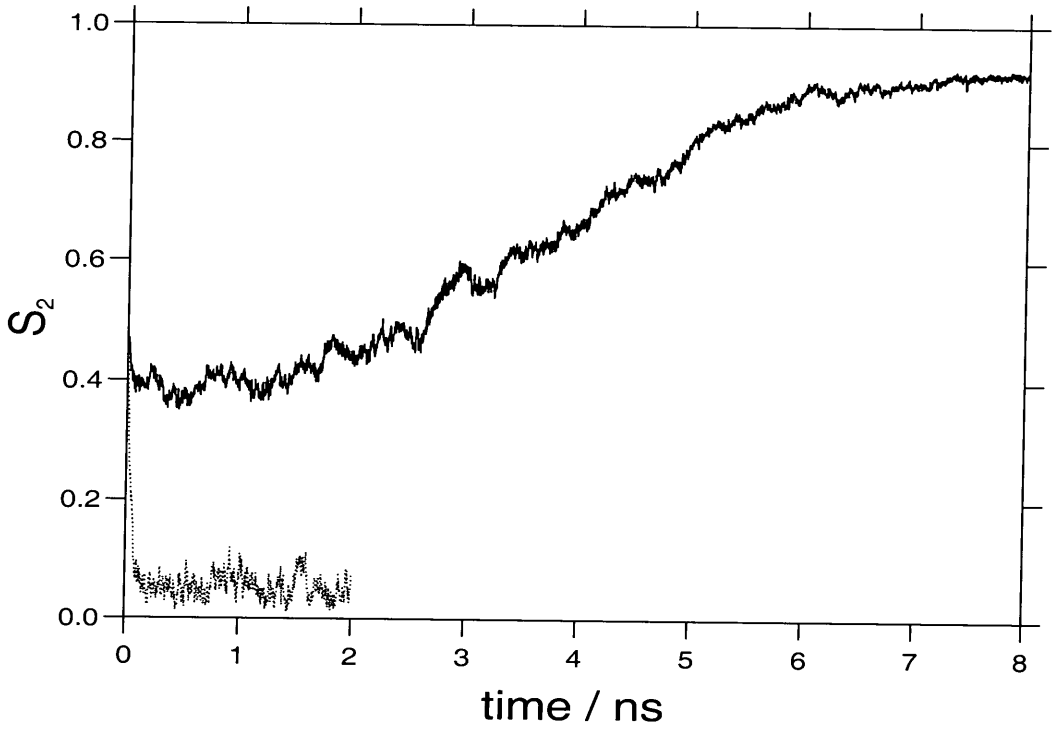

Figure 4.2: Order parameter S_2 at 752.092 kg m^{-3} at 200 K (solid line) corresponding to the growth of a smectic-B phase from a pseudo-nematic structure, and at 250 K (dotted line) showing the decay to the isotropic phase.

behaviour at the two densities. In these runs each picosecond of simulation time corresponds to approximately 4.6 cpu minutes on a DEC 433au workstation.

4.4 Results and discussion

4.4.1 Phase behaviour - low density system ($\rho = 752.092$ kg m^{-3})

The time evolution of the order parameter for the low density (752.092 kg m^{-3}) system at 200 K is shown in figure 4.2, along with the order parameter for the 235 K run for comparison. At 200 K the rise in $\langle S_2 \rangle$ is extremely slow and is accompanied by pre-transitional fluctuations that eventually lead to the formation of a smectic-B phase

with $\langle S_2 \rangle = 0.92$ (figure 4.3).

The smectic-B phase assignment is based on the form of the radial distribution functions shown in figures 4.5, 4.6, 4.7. The peaks in $g_{||}(r)$ (figure 4.6) indicate a layer spacing of approximately 23.7 Å, in comparison to an *all-trans* molecular length of $21.3 + \sigma^{LJ} = 25.2$ Å. The perpendicular component of the pair distribution function, $g_{\perp}(r)$ (figure 4.7), is used to monitor the intra-layer molecular order. The splitting of the second peak at $r/$Å$=10$ into two occurs as orientational order increases. This is indicative of hexagonal close packing within the layers, confirming the presence of a smectic-B phase. The smectic-B phase was seen to melt to an isotropic liquid at a temperature of 235 K. Separate simulations at 215 K starting from smectic-B and isotropic configurations respectively, showed no change in phase. This allowed us to assign the phase transition to between 200 K and 235 K. For relatively small systems one expects to see some degree of hysteresis in the position of the phase transition. Careful monitoring of the diffusion constant whilst cooling the smectic-B to temperatures below 200 K, indicated that the system had frozen. No significant structural differences were apparent between the smectic-B and frozen states. No regions of nematic or smectic-A stability were seen at $\rho = 752.092$ kg m^{-3}. Undoubtably the relative strength of Gay-Berne/Gay-Berne interactions, over the other non-bonded interactions, strongly promotes smectic behaviour in systems of this type. Consequently, the phase behaviour at this density is very similar to low density systems of Gay-Berne particles without alkyl chains [94, 99] where no nematic phase is seen.

4.4.2 Phase behaviour - high density system ($\rho = 970.411$ kg m^{-3})

Starting from the pseudo nematic configuration with $\langle S_2 \rangle = 0.60$, the high density system ($\rho = 970.411$ kg m^{-3}) evolved into a nematic phase with an order parameter of

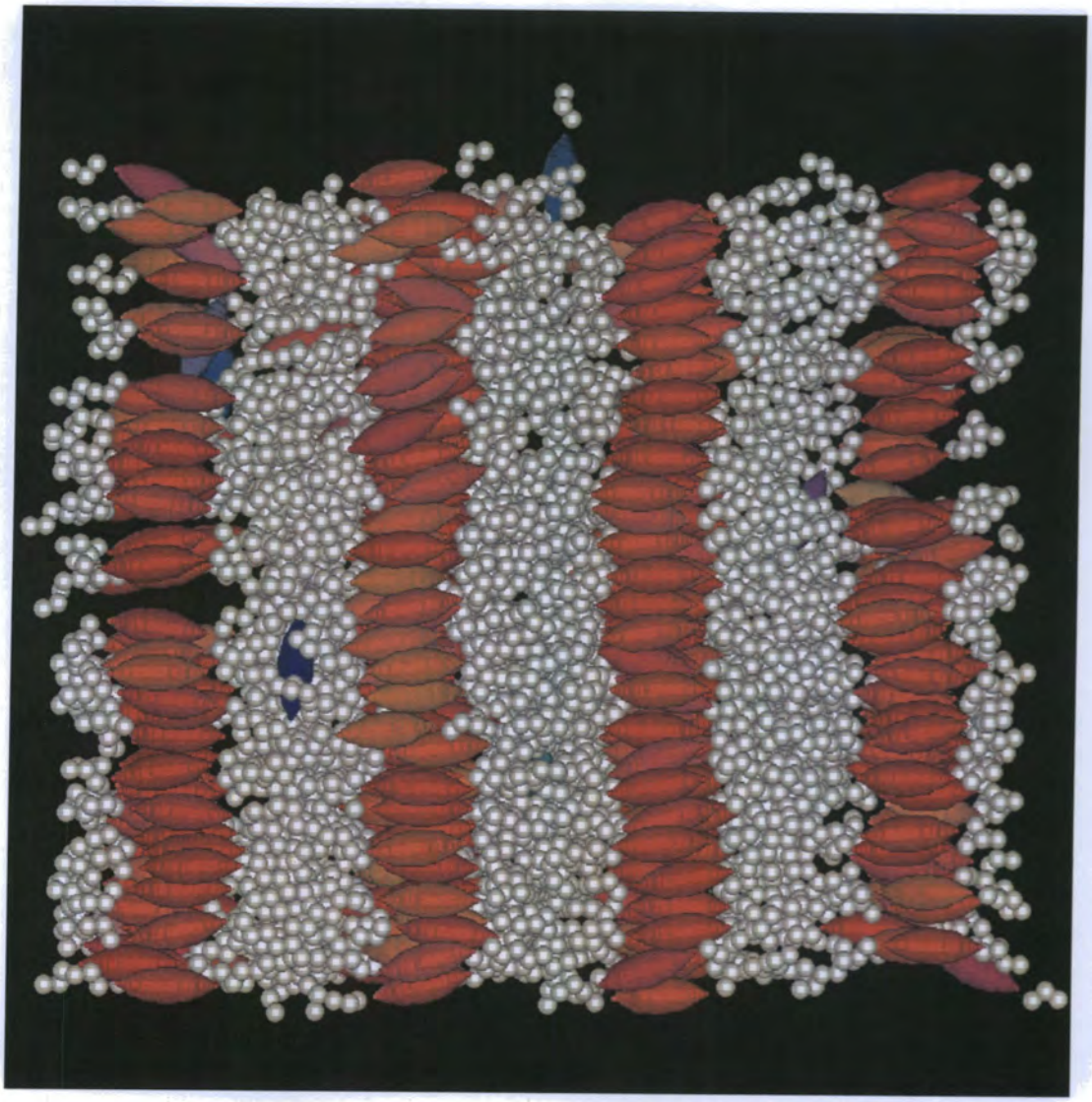

Figure 4.3: System snapshot: Smectic-B phase at 200 K (752.092 kg m^{-3}). Gay-Berne sites are represented by coloured ellipsoids; Lennard-Jones sites are represented by white spheres.

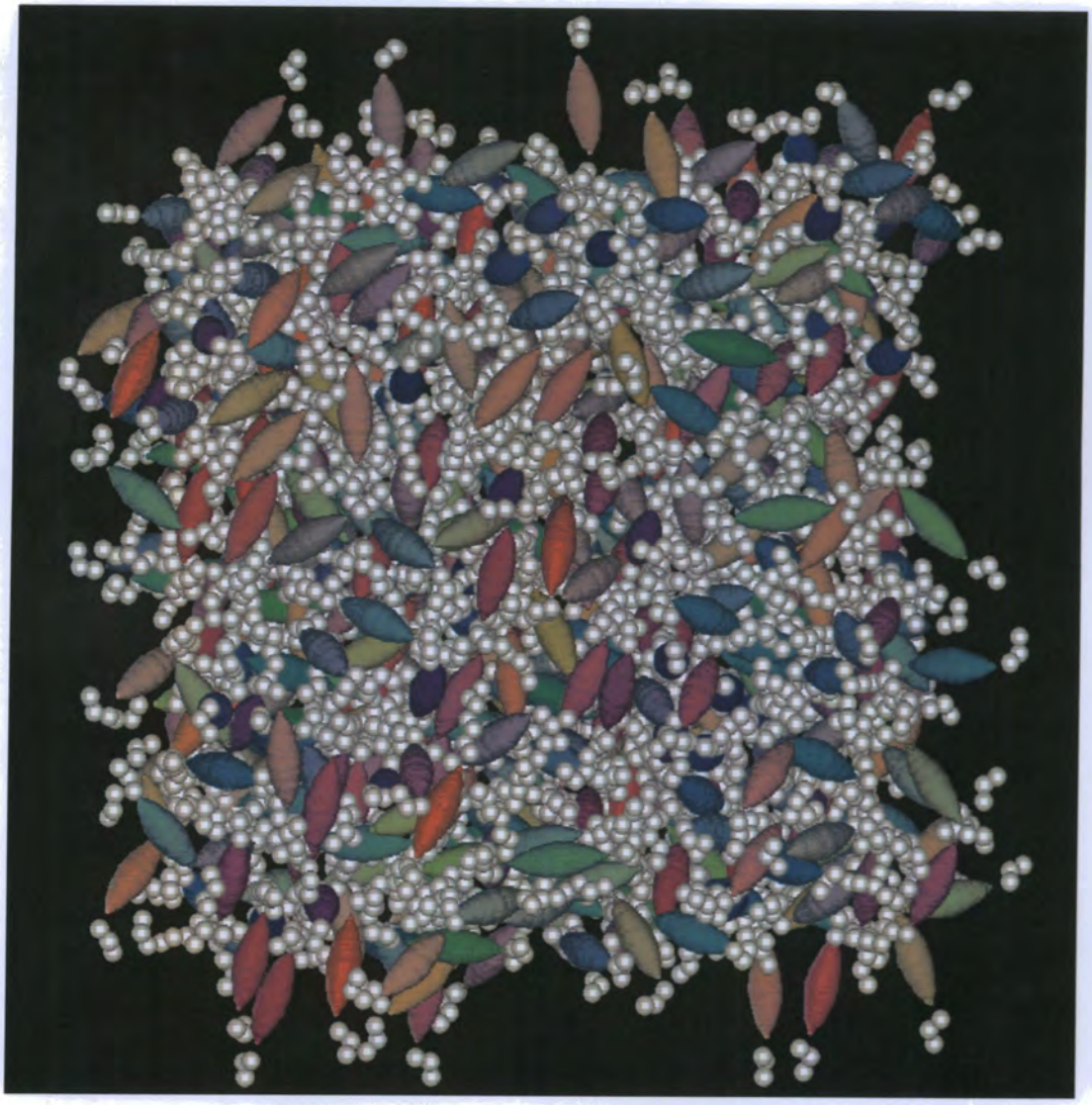

Figure 4.4: System snapshot: isotropic configuration at 500 K (752.092 kg m^{-3}). Gay-Berne sites are represented by coloured ellipsoids; Lennard-Jones sites are represented by white spheres.

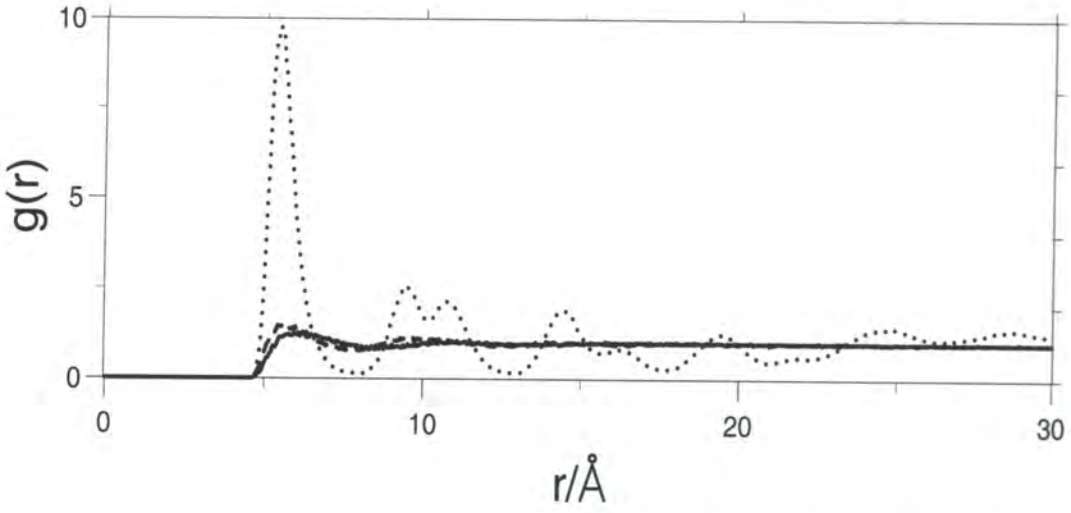

Figure 4.5: Radial distribution functions $g(r)$ for Gay-Berne sites in the NVT ensemble: bold line 300 K low density system (isotropic), dashed line 300 K high density system (nematic) and dotted line 200 K low density system (smectic-B)

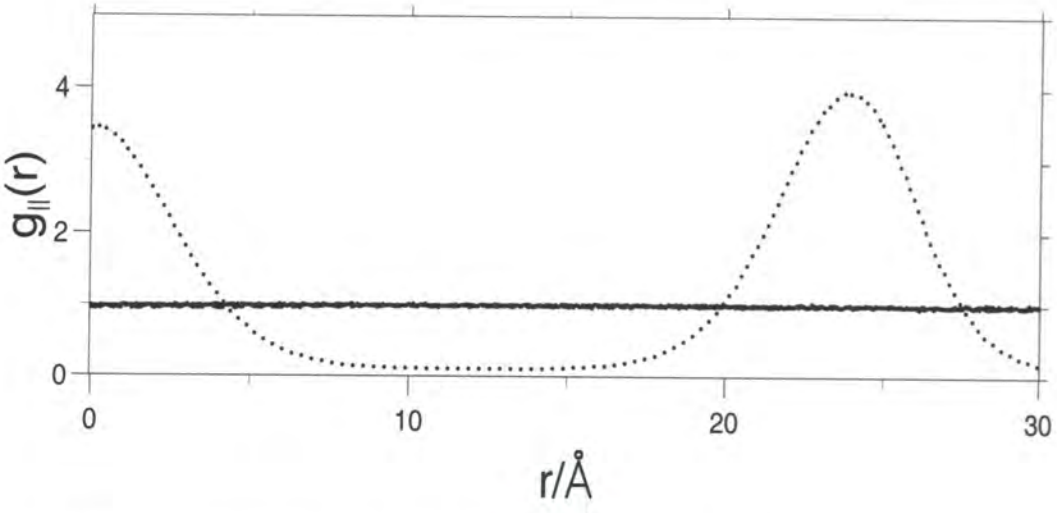

Figure 4.6: Radial distribution functions $g_{\|}(r)$ for Gay-Berne sites in the NVT ensemble: bold line 300 K low density system (isotropic), dashed line 300 K high density system (nematic) and dotted line 200 K low density system (smectic-B)

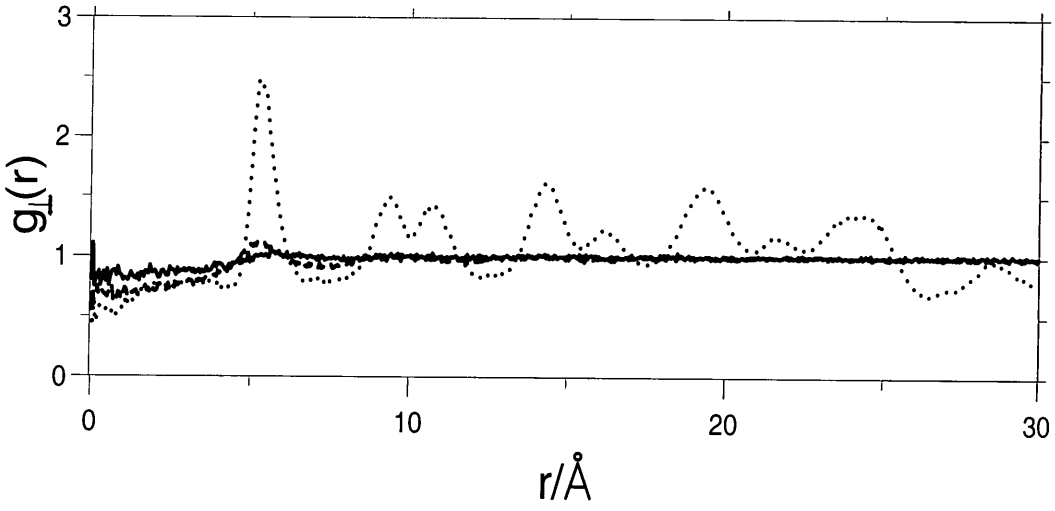

Figure 4.7: Radial distribution functions $g_\perp(r)$ for Gay-Berne sites in the NVT ensemble: bold line 300 K low density system (isotropic), dashed line 300 K high density system (nematic) and dotted line 200 K low density system (smectic-B)

$\langle S_2 \rangle \approx 0.73$ over a period of 1.0 ns (figure 4.8). Further simulations over a period of 7.0 ns demonstrated no changes in orientational or translational order. Careful monitoring of the pair distribution functions, $g(r)$, $g_\perp(r)$, $g_{||}(r)$, indicated that there were no significant smectic fluctuations during the course of these runs. $g_{||}(r)$ for this system (figure 4.6) remained completely flat, and both $g(r)$ and $g_\perp(r)$ exhibited only small peaks at $r \approx 5.5$ Å corresponding to the first solvation shell; typical of the behaviour for a nematic system [100]. The nematic ordering is confirmed by the form of the pair-wise orientational correlation function $g_2(r)$ for Gay-Berne sites (equation 2.23). In the nematic phase this function decays to a value of $\langle S_2 \rangle^2$ at large separations, as shown in figure 4.9. Here, the nematic phase is clearly distinguished from the isotropic phase (where $g_2(r)$ decays to zero within the simulation box), and the smectic-B phase (where the intra- and interlayer spacing give rise to a series of peaks and troughs in $g_2(r)$).

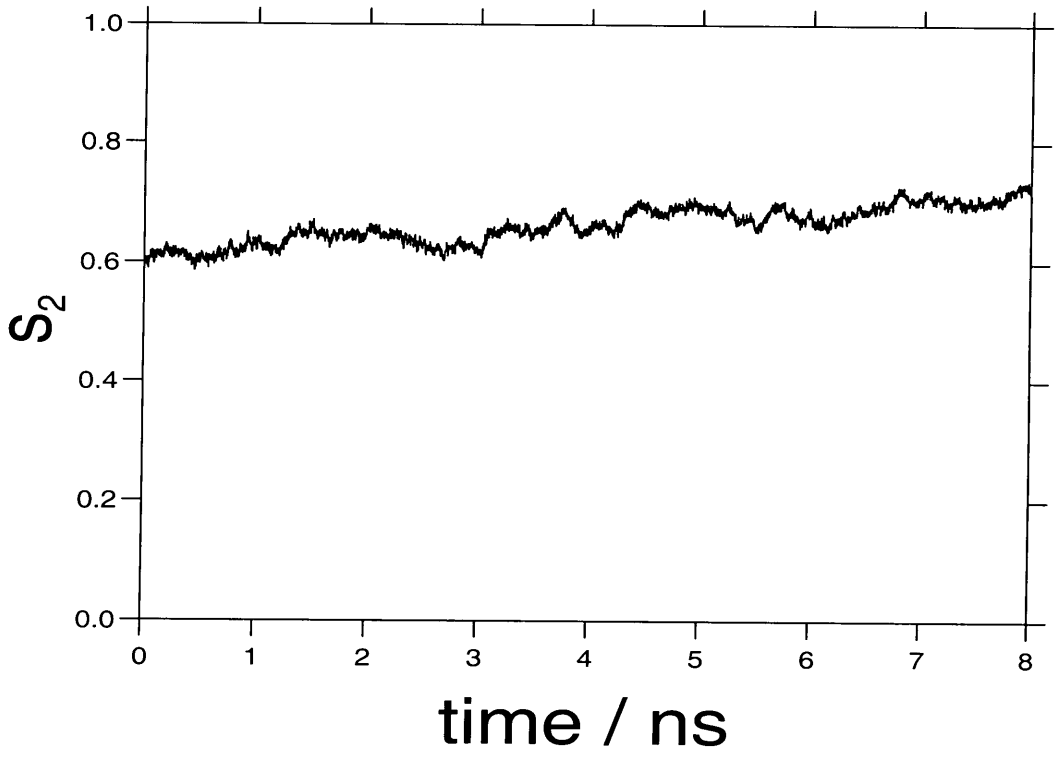

Figure 4.8: Order parameter S_2 at 970.411 kgm^{-3} at 300K.

The fully equilibrated nematic configuration at 300 K was used as a starting point for a further series of simulations. The nematic phase was found to be stable at temperatures up to 400 K. At 250 K monitoring of the diffusion constant indicated that the nematic froze to form a solid structure. Based on the phase behaviour of the low density system, it is likely that a smectic-B phase will exist between 250 K and 300 K given slow cooling of the system. However, limitations on available computer time have not allowed long runs at intermediate temperatures (between 250-300 K) to test this assumption. A full summary of all equilibrated state points for both the low and high density systems is presented in table 4.2.

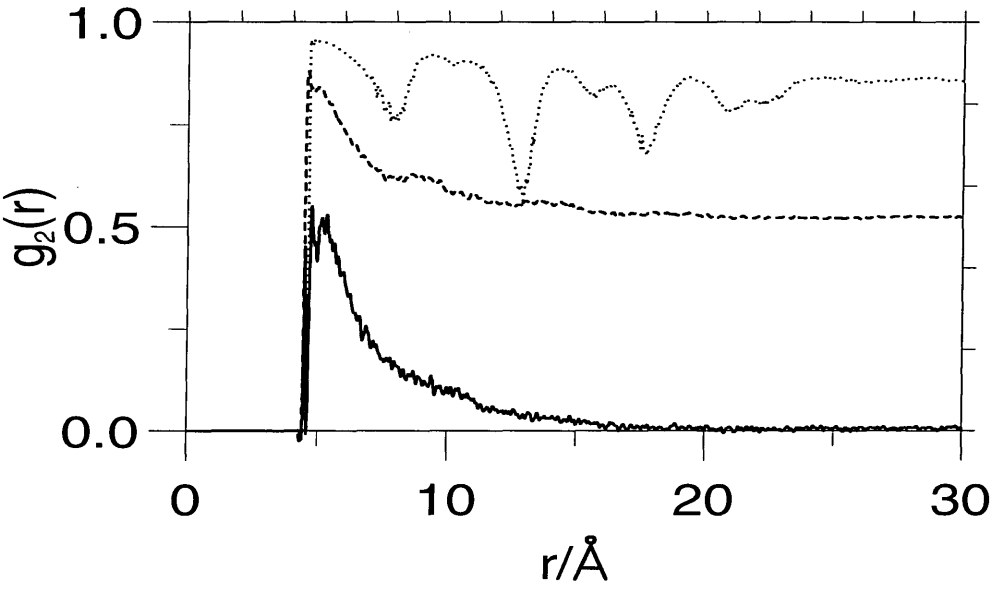

Figure 4.9: Pairwise orientational correlation function $g_2(r)$ for Gay-Berne centres, bold line 300 K low density system (isotropic), dashed line 300 K high density system (nematic) and dotted line 200 K low density system (smectic-B).

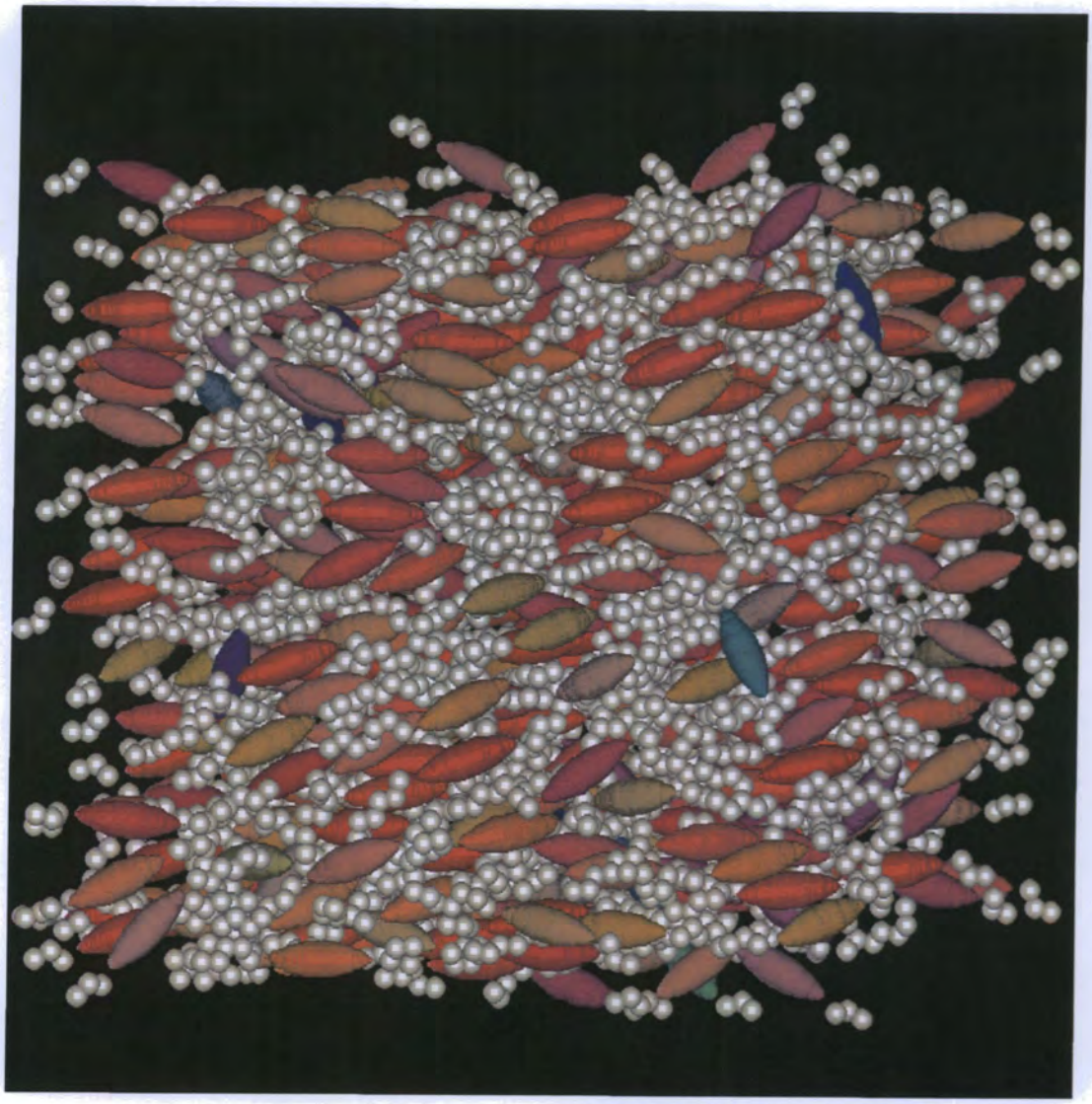

Figure 4.10: Snapshots from simulations in the NVT ensemble; nematic phase at 300 K at the high density Gay-Berne sites are represented by coloured ellipsoids; Lennard-Jones sites are represented by white spheres.

T /K	phase	density kg m^{-3}	equilibration time / ps	production time / ps	$\overline{S_2} \pm \sigma_x$	mean squared diffusion of GB units /Å^{2}ps^{-1}
200	solid	970.411	600	600	0.74 ± 0.01	2.7
250	nematic	970.411	400	3800	0.75 ± 0.01	6.1
300	nematic	970.411	1000	7000	0.73 ± 0.01	13.8
350	nematic	970.411	200	200	0.68 ± 0.01	22.6
400	nematic	970.411	200	800	0.55 ± 0.02	27.6
450	isotropic	970.411	200	1800	0.17 ± 0.02	31.2
200	smectic-B	752.092	6000	2000	0.92 ± 0.01	6.7
215	smectic-B	752.092	200	1000	0.92 ± 0.01	6.3
235	isotropic	752.092	400	1600	0.08 ± 0.02	72.2
250	isotropic	752.092	200	1800	0.04 ± 0.02	244.7
300	isotropic	752.092	200	800	0.09 ± 0.03	112.4
350	isotropic	752.092	200	600	0.06 ± 0.02	144.7
400	isotropic	752.092	200	800	0.05 ± 0.02	
450	isotropic	752.092	200	800	0.05 ± 0.02	
500	isotropic	752.092	200	1000	0.04 ± 0.02	
550	isotropic	752.092	200	1000	0.04 ± 0.02	

Table 4.2: Summary of simulation data in NVT ensemble. Quoted values of order parameters are for Gay-Berne units.

4.4.3 Comparison with a single-site Gay-Berne potential

It is interesting to compare the phase behaviour of our model with that of the pure Gay-Berne mesogen [94, 99]. As seen with the pure Gay-Berne potential, increases in density promote nematic behaviour. The origin of this effect lies in the competition between orientational and translational entropy within the system. As volume is reduced, molecules lying at an angle to each other exclude neighbours from a larger fraction of the total volume. This leads to a reduction in the translational entropy and molecules start to favour parallel alignment, enhancing the nematic region of the phase diagram. It is well-known that some twin-chain (real) mesogens form smectic-C phases. However, in the current model system the relatively high stability of the smectic-B phase has suppressed the formation of other smectic phases that do not possess intra-layer order.

It is known from the work of Brown *et al.* [101, 102] that a smectic-A phase can be induced by lengthening a Gay-Berne mesogen and simulating at elevated pressures. It is therefore possible that the system studied here may possess a smectic-A or smectic-C phase at higher densities in a region of the phase diagram that has not been studied.

4.4.4 Bond order parameters

Replacing the vector $\mathbf{e}_j$ in equation 2.17 by bond vectors allows individual order parameters to be calculated for each bond in the molecule. These are given in table 4.3 for the longer C_7 chain. In the nematic and smectic-B phases the values of bond order parameters exhibit a classic odd-even effect, with odd bonds having high order parameters and even bonds having order parameters close to zero. This reflects the relative importance of the *all-trans* conformation in the mesophases formed. Here successive bonds lie alternately parallel and at an angle to the molecular long axis. However, the

Bond	200 K	300 K	300 K	450 K
	752.092 kg m^{-3}	752.092 kg m^{-3}	970.411 kg m^{-3}	970.411 kg m^{-3}
GB-C_4	0.92	0.09	0.73	0.17
C_4-C_5	0.11	0.04	0.05	0.04
C_5-C_6	0.86	0.05	0.58	0.09
C_6-C_7	0.10	0.04	0.04	0.03
C_7-C_8	0.79	0.04	0.51	0.06
C_8-C_9	0.10	0.04	0.04	0.04
C_9-C_{10}	0.67	0.04	0.39	0.05

Table 4.3: Order parameters for bonds in the 7 site alkyl chain.

odd-even effect is seen to decrease in magnitude as the bonds become further from the molecular core, reflecting an increase in chain disorder. In several homologous series of real liquid crystals, this odd-even ordering of successive bonds manifests itself in an odd-even rise and fall in clearing temperatures. This is also seen to diminish as the alkyl chain becomes longer. It is noted that in both nematic and smectic-B phases, bond order parameters are always smaller than the order parameters for the Gay-Berne units, indicating the importance of the latter in determining the overall structure of the bulk liquid crystal.

4.4.5 Dihedral angle distributions and *trans/gauche* populations

The differences in bond order parameters found at different phases in table 4.3, point to the fact that large conformational changes must be occurring as the system moves from one state point to another. To monitor this the dihedral angle distributions were calculated (figure 4.11) for the dihedrals $\phi_1, \phi_3 - \phi_7$ as defined in figure 4.1. It is seen

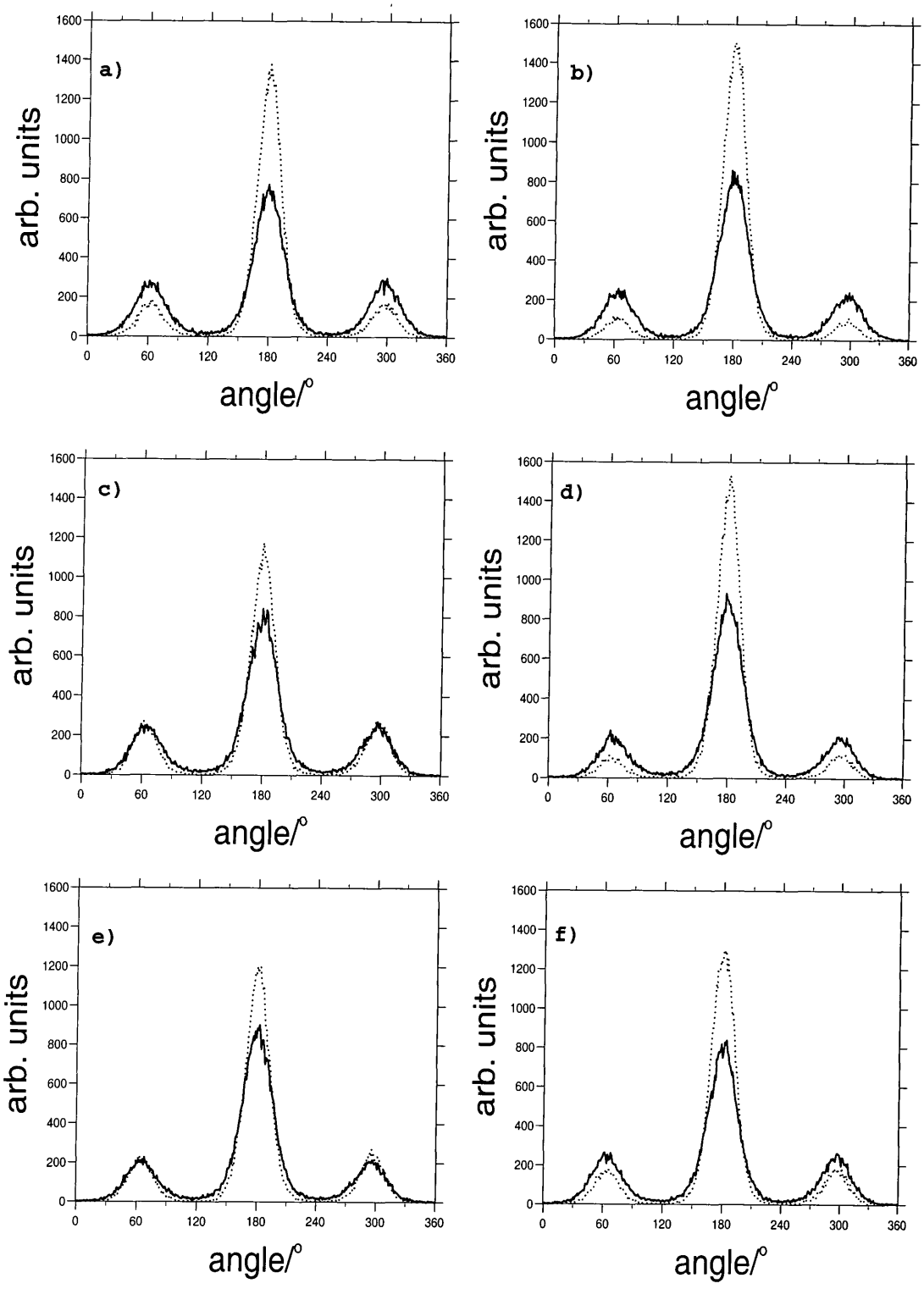

Figure 4.11: Dihedral angle distribution of (a) ϕ_1; (b) ϕ_3; (c) ϕ_4; (d) ϕ_5; (e) ϕ_6; (f) ϕ_7; in the NVT ensemble at density 970.411 kg m^{-3} bold line 450 K (isotropic), and dotted line 300 K (nematic)

from figure 4.11 that there is a strong preference for *trans* conformations in the nematic phase at 300 K compared to the isotropic phase at 450 K. Within the nematic phase the longer C_7 chain prefers the *trans* conformation more strongly for the odd dihedrals in the chain compared to even dihedrals: thus explaining the bond order parameter data seen in section 4.4.4. In the isotropic phase the odd-even effect disappears.

Integrating the dihedral angle distributions provides *trans/gauche* populations. In table 4.4 these are given for the nematic and isotropic state points of figure 4.11, and for two state points corresponding to the smectic-B and isotropic phases of the low density system. In the orientationally ordered phases, *gauche* conformations where the molecule remains elongated ϕ_6 and, in particular, ϕ_4 are favoured over *gauche* conformations in which the end of the chain is forced to lie at an angle to the molecular axes ϕ_1, ϕ_3, ϕ_5, ϕ_7. This effect has been seen before in the simulation of liquid crystal dimers [80] and in molecules with C_5 chains [21, 24]. The effect is also consistent with results of molecular field theory [81, 103].

4.4.6 Effective torsional potentials

The influence of the odd-even effect in table 4.4 is seen to reduce as dihedrals move away from the molecular core. Again this is consistent with the predictions of molecular field theory and experiment. Figure 4.12 shows a comparison between the effective torsional potentials (equation 3.6) at 300 K (nematic) and 450 K (isotropic) for the low density system. The difference in the two curves for each graph provides a direct measure in the change in V_{ext} between the two phases, and allows us to extract the energy difference between *trans* and *gauche* conformers for the two phases (table 4.5). The results in table 4.5 clearly show that the odd *gauche* conformers become energetically disfavoured in the nematic phase by between 1.3 kJ mol^{-1} and 0.6 kJ mol^{-1}, whilst the even *gauche*

T/K	phase	density/kg m^{-3}	dihedral	g$_-$/%	t/%	g$_+$/%
450	isotropic	970.411	ϕ_1	21.6	56.4	21.9
			ϕ_3	19.1	62.4	18.5
			ϕ_4	19.5	61.1	19.4
			ϕ_5	16.0	67.8	16.2
			ϕ_6	16.6	67.1	16.3
			ϕ_7	19.5	61.0	19.5
300	nematic	970.411	ϕ_1	10.7	79.0	10.3
			ϕ_3	6.7	87.2	6.1
			ϕ_4	16.0	67.5	16.4
			ϕ_5	6.3	86.2	7.4
			ϕ_6	13.8	70.9	15.3
			ϕ_7	10.8	78.1	11.1
300	isotropic	752.092	ϕ_1	16.6	67.6	15.8
			ϕ_3	15.4	70.9	13.6
			ϕ_4	14.9	71.4	13.7
			ϕ_5	11.8	76.2	12.1
			ϕ_6	12.9	74.9	12.2
			ϕ_7	14.6	70.5	14.9
200	smectic-B	752.092	ϕ_1	5.3	88.3	6.3
			ϕ_3	1.3	97.6	1.0
			ϕ_4	10.6	80.3	9.1
			ϕ_5	1.6	95.9	2.5
			ϕ_6	8.5	82.1	9.4
			ϕ_7	6.3	89.6	4.1

Table 4.4: *Trans-gauche* populations for selected state-points in the NVT ensemble

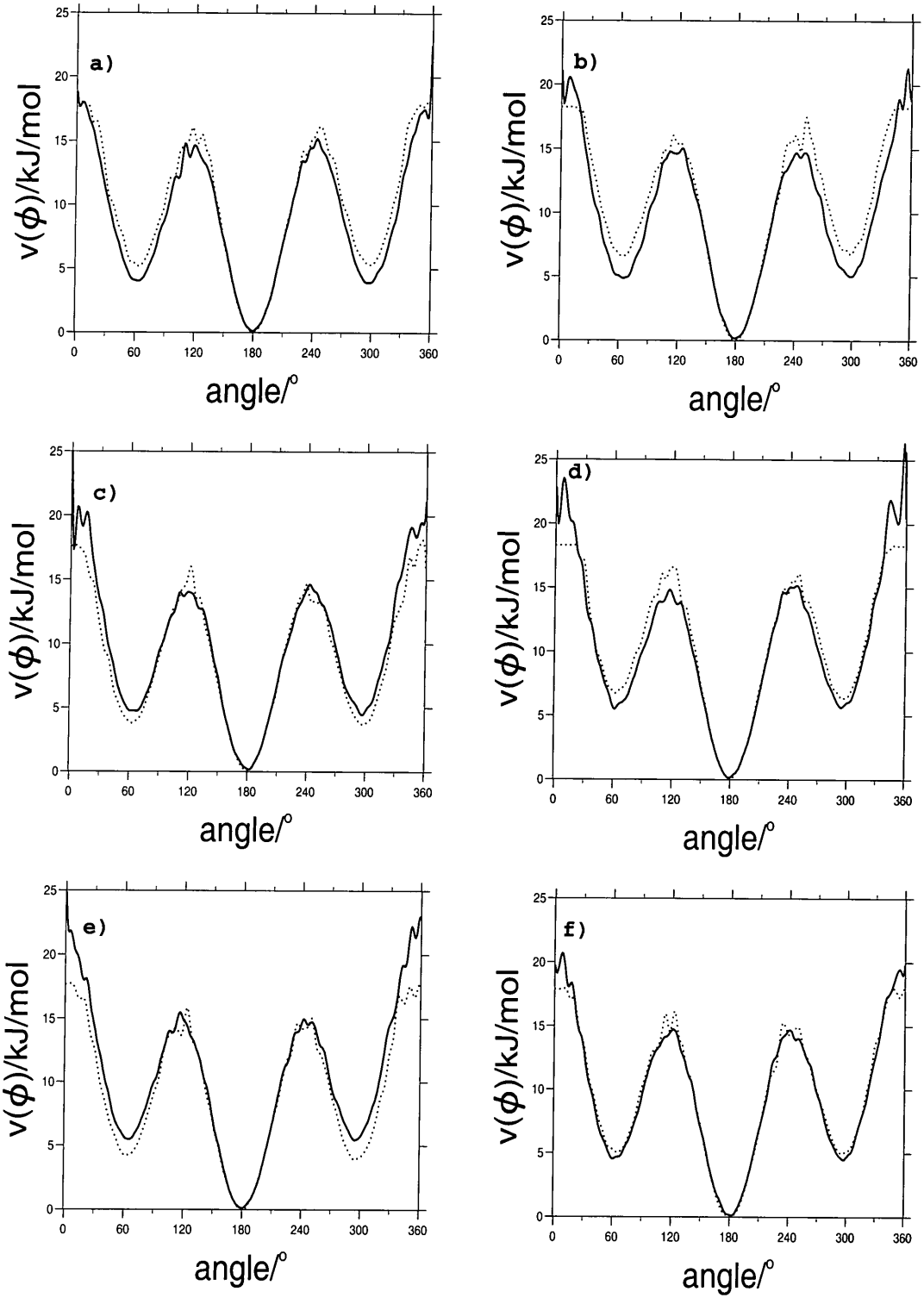

Figure 4.12: Effective torsional potential of (a) ϕ_1; (b) ϕ_3; (c) ϕ_4; (d) ϕ_5; (e) ϕ_6; (f) ϕ_7; in the NVT ensemble at density 970.411 kg m^{-3} bold line 450 K (isotropic), and dotted line 300 K (nematic)

Dihedral	ΔE_{gt}(450K) (isotropic)	ΔE_{gt}(300K) (nematic)	ΔE_{gt}(450K) $-\Delta E_{gt}$(300K)
ϕ_1	3.8	5.2	1.3
ϕ_3	4.8	6.7	1.9
ϕ_4	4.4	3.7	-0.8
ϕ_5	5.4	6.5	1.1
ϕ_6	5.4	4.1	-1.3
ϕ_7	4.4	5.0	0.6

Table 4.5: Differences in energy ΔE_{gt} between *gauche* and *trans* conformers for the high density system in units of kJ mol^{-1}.

conformers become energetically favoured by between 0.8 kJ mol^{-1} and 1.3 kJ mol^{-1}.

It is interesting to compare these results with values of ΔE_{gt} calculated elsewhere. In the simulation of 5,5-BBCO (Chapter 3) it was found that ΔE_{gt} *decreases* in magnitude for the central dihedral of the C_5 chain in going from the isotropic to the nematic phase. Wilson and Allen [24] have studied the mesogen *trans*-4-(*trans*-4-n-pentylcyclohexyl)cyclohexylcarbonitrile (CCH5) and report *increases* in ΔE_{gt} of 1.1, 0.03, 0.72 kJ mol^{-1} for the three dihedrals of the (C_5) alkyl chain, in going from the pretransitional isotropic phase at 390 K to a nematic phase with an order parameter of 0.62. In the work of Wilson [22] *increases* in ΔE_{gt} of approximately 2 kJ mol^{-1} are reported for the odd dihedrals of a GB-C_8-GB liquid crystal dimer system, in going from the isotropic phase at 330 K to a smectic-A phase with $S_2 = 0.75$ at 300 K. Much smaller increases in ΔE_{gt} are seen for the even dihedrals. The magnitude of the change in ΔE_{gt} is similar in all these systems, but there are clearly significant differences in the behaviour of different molecules. In each case however, the changes in ΔE_{gt} can

Molecule	reference	temperature/phase	all-*trans* population/%
CCH5	[24]	350 K (nematic)	49.2
GB-C_8-GB (dimer)	[22]	300 K (smectic-A)	47.2
5,5-BBCO	[21]	300 K (nematic)	29.9
C_7-GB-C_3	this chapter	300 K (nematic)	27.8

Table 4.6: Population of the all-*trans* conformer in a series of mesophase simulations.

be directly assigned to a preference for linear conformers in the mesophase. In the simulations of CCH5 and the liquid crystal dimer system the all-*trans* conformation is overwhelmingly preferred in the mesophase at the expense of odd *gauche* conformers (see table 4.6): leading to *increases* in ΔE_{gt} with increases in S_2 for odd *gauche* conformers. However for simulations of 5,5-BBCO and the C_3-GB-C_7 (where individual molecules have two chains) the all-*trans* conformation is relatively less important, and linear *gauche* conformers are strongly promoted by an increase in orientational order (see table 4.7): leading to a clear *decrease* in the value of ΔE_{gt} for even *gauche* conformers. Clearly, the influence of the mesophase on ΔE_{gt} depends critically on the overall shape of individual conformations and the balance of individual conformers at a particular temperature. This will depend not only on the length of the alkyl chain, but also on the shape of the molecular core.

4.5 Conclusions

Simulations have been performed on a hybrid Lennard-Jones/Gay-Berne mesogen with two alkyl chains (C_3-GB-C_7) for systems of 512 molecules at two densities. For the low density system (ρ = 752.092 kg m^{-3}) isotropic liquid and smectic-B phases are

ϕ_3	ϕ_4	ϕ_5	ϕ_6	ϕ_7	nematic / %	liquid / %
t	t	t	t	t	27.8	8.0
t	t	t	g+	t	7.0	3.1
t	g-	t	t	t	6.9	3.6
t	t	t	g-	t	6.8	3.5
t	g+	t	t	t	6.6	3.3
t	t	t	t	g+	3.7	3.3
t	t	t	t	g-	3.6	3.3
t	g-	t	g+	t	2.8	1.7
t	g+	t	g-	t	2.4	1.6
t	g+	t	g+	t	2.0	1.5
t	t	g-	t	t	2.0	2.9
t	t	g+	t	t	2.0	2.9
t	g-	t	g-	t	1.8	1.6
g+	t	t	t	t	1.1	2.3
t	g+	t	t	g+	1.1	1.5
t	g+	t	t	g-	1.1	1.2
g-	t	t	t	t	1.1	2.2
t	g-	t	t	g-	1.1	1.3
t	g-	t	t	g+	1.0	1.7

Table 4.7: Conformer populations for the nematic (300 K) and isotropic liquid (450 K) phases for the 970.411 kg m^{-3} system.

found, and for the high density system (ρ = 970.411 kg m^{-3}) the presence of a stable nematic phase is detected. The latter is promoted by excluded volume interactions that favour orientationally ordered states at high density. A strong coupling is seen between internal molecular structure within the model and the orientational order of the phase itself. Consequently, molecules show large conformational changes in moving from the isotropic to either the nematic or the smectic-B phase. This has been characterised by calculating effective torsional angle potentials for each phase. It is found that *gauche* conformations in which the chain lies along the the molecular long axis are selectively favoured in the orientationally ordered phases by up to 1.3 kJ mol^{-1} compared to the isotropic liquid, but the conformers where the chain lies at an angle to the molecular long axis are actively disfavoured by up to 1.9 kJ mol^{-1}.

One of the most useful outcomes of the work in this chapter has been the discovery of a stable nematic phase over a considerable temperature range. Prior to the work in this thesis, none of the previous simulation studies on atomistic (or hybrid) models had conclusively demonstrated the stability of a nematic mesophase over long simulation times. The current work therefore provides a useful model system to use in developing methods for the calculation of the bulk properties of liquid crystals. In chapter 5 this model is exploited further to provide the first calculations of elastic constants for flexible liquid crystal molecules.

CHAPTER 5

Nematic Elastic Constants

5.1 Introduction

In this chapter a study is made of the elastic properties of the nematic phase generated by the hybrid model of chapter 4. This provides, for the first time, results for the Frank elastic constants of a flexible liquid crystal molecule. The importance of a knowledge of these elastic constants for display devices is highlighted by the following equation

$$U_0 = \sqrt{\frac{\pi^2(K_1 + \frac{1}{4}(K_3 - 2K_2))}{2\epsilon_0(\epsilon_{||} - \epsilon_{\perp})}} \tag{5.1}$$

where U_0 is the threshold voltage required for switching in a ($\pi/2$ twist) twisted nematic device [104]. Here, K_1, K_2 and K_3 are the nematic elastic constants, respectfully corresponding to splay, twist and bend deformations, $\epsilon_{||}$ and $\epsilon_{\perp}$ are the dielectric constants, and ϵ_0 is the vacuum dielectric permittivity.

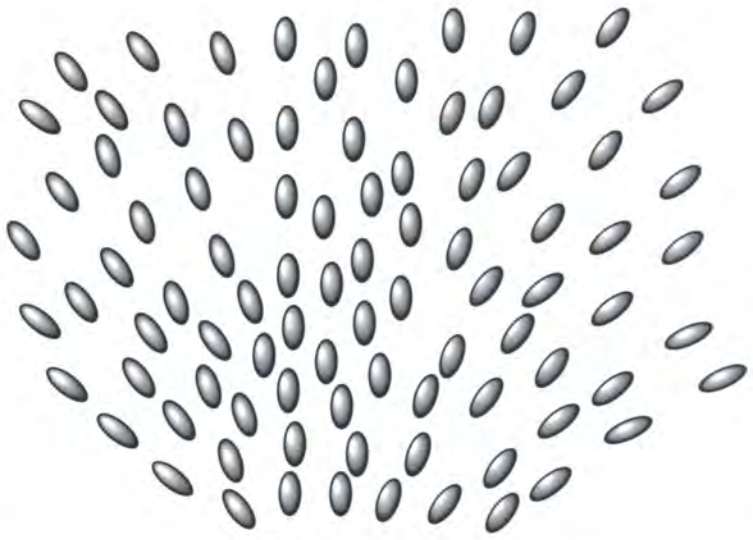

Figure 5.1: A representation of a splay deformation in a nematic liquid crystal.

5.2 Frank elastic constants

Continuum theory of nematic liquid crystals disregards structure on the molecular scale. The expression for the free energy density F_d of a distortion in the bulk nematic was developed by Frank [105], and is given by

$$F_d = \frac{1}{2}K_1[\text{div } \mathbf{n}(\mathbf{r})]^2 + \frac{1}{2}K_2[\mathbf{n}(\mathbf{r}) \cdot (\text{curl } \mathbf{n}(\mathbf{r}))]^2 + \frac{1}{2}K_3[\mathbf{n}(\mathbf{r}) \times (\text{curl } \mathbf{n}(\mathbf{r}))]^2 \quad (5.2)$$

where $\mathbf{n}(\mathbf{r})$ is a vector associated with the direction of the director field, and K_1, K_2 and K_3 are the Frank elastic constants, respectively known as the *splay*, *twist* and *bend* constants (see figures 5.1-5.3). Each of the Frank terms are positive, this is because expression 5.2 describes distortions from the minimum of the free energy density, any deformation in the director field leads to an increase in free energy.

5.3 Theory and methodology

In this study the Frank elastic constants are calculated from fluctuations of the nematic director (Allen *et al.* [97, 106]). For each set of coordinate data the nematic order

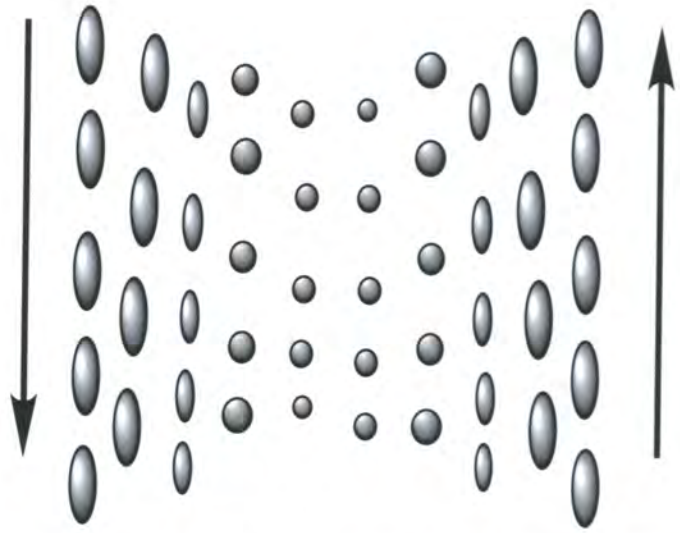

Figure 5.2: A representation of a twist deformation in a nematic liquid crystal.

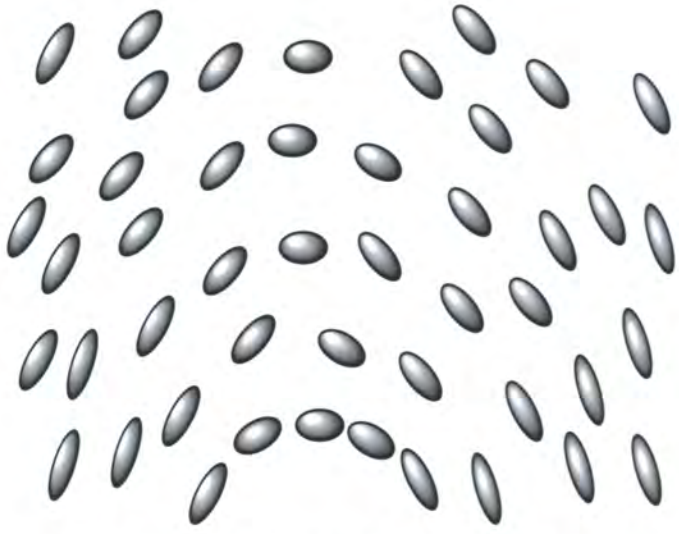

Figure 5.3: A representation of a bend deformation in a nematic liquid crystal.

parameter S_2 and director $\hat{\mathbf{n}}$ are calculated. A symmetric ordering tensor is then constructed in reciprocal space using the long axis vectors $\mathbf{u}_i$ for the Gay-Berne units

$$\hat{Q}_{\alpha\beta}(\mathbf{k}) = \frac{V}{N_{\mathrm{m}}} \sum_{i=1}^{N_{\mathrm{m}}} \left(\frac{3}{2} u_{i\alpha} u_{i\beta} - \frac{1}{2} \delta_{\alpha\beta} \right) \exp(i\mathbf{k} \cdot \mathbf{r}_i), \qquad \alpha, \beta = x, y, z. \tag{5.3}$$

Following Forster [107,108] an axis system **1**,**2**,**3**, is defined such that $\hat{\mathbf{n}} = (0, 0, 1)$. For wave vectors in the 1-3 plane, $\mathbf{k} = (k_1, 0, k_3)$, we obtain the equations

$$W_{13}(k_1, k_3) \equiv \frac{9/4 \;\; {S_2}^2 V k_B T}{\left\langle \left| \hat{Q}_{13}(\mathbf{k}) \right|^2 \right\rangle} \quad \rightarrow K_1 k_1^2 + K_3 k_3^2, \qquad as\ k \rightarrow 0 \tag{5.4}$$

$$W_{23}(k_1, k_3) \equiv \frac{9/4 \;\; {S_2}^2 V k_B T}{\left\langle \left| \hat{Q}_{23}(\mathbf{k}) \right|^2 \right\rangle} \quad \rightarrow K_2 k_1^2 + K_3 k_3^2, \qquad as\ k \rightarrow 0. \tag{5.5}$$

The values of components $\hat{Q}_{13}(\mathbf{k})$ and $\hat{Q}_{23}(\mathbf{k})$ can be transformed to the 1-3 plane via rotation of the ordering tensor $\hat{Q}(\mathbf{k})$ using the equations [109]

$$\hat{Q}_{13}(\mathbf{k}) = \begin{pmatrix} e_{1x} & e_{1y} & e_{1z} \end{pmatrix} \begin{pmatrix} \hat{Q}_{xx} & \hat{Q}_{xy} & \hat{Q}_{xz} \\ \hat{Q}_{yx} & \hat{Q}_{yy} & \hat{Q}_{yz} \\ \hat{Q}_{zx} & \hat{Q}_{zy} & \hat{Q}_{zz} \end{pmatrix} \begin{pmatrix} e_{3x} \\ e_{3y} \\ e_{3z} \end{pmatrix} \tag{5.6}$$

and

$$\hat{Q}_{23}(\mathbf{k}) = \begin{pmatrix} e_{2x} & e_{2y} & e_{2z} \end{pmatrix} \begin{pmatrix} \hat{Q}_{xx} & \hat{Q}_{xy} & \hat{Q}_{xz} \\ \hat{Q}_{yx} & \hat{Q}_{yy} & \hat{Q}_{yz} \\ \hat{Q}_{zx} & \hat{Q}_{zy} & \hat{Q}_{zz} \end{pmatrix} \begin{pmatrix} e_{3x} \\ e_{3y} \\ e_{3z} \end{pmatrix} \tag{5.7}$$

where

$$\hat{\mathbf{e}}_1 = \mathbf{k} - (\hat{\mathbf{n}} \cdot \mathbf{k})\hat{\mathbf{n}} \tag{5.8}$$

$$\hat{\mathbf{e}}_3 = \hat{\mathbf{n}} \tag{5.9}$$

and $\hat{\mathbf{e}}_2$ is mutually perpendicular to $\hat{\mathbf{e}}_1$ and $\hat{\mathbf{e}}_3$:

$$\hat{\mathbf{e}}_2 = \hat{\mathbf{e}}_1 \times \hat{\mathbf{e}}_3. \tag{5.10}$$

During our simulations the director is free to drift, yet our analysis requires a fixed grid of points in **k** space. To account for this we rotate the grid of **k**-space points by the operation

$$\begin{pmatrix} e_{1x} & e_{1y} & e_{1z} \\ e_{2x} & e_{2y} & e_{2z} \\ e_{3x} & e_{3y} & e_{3z} \end{pmatrix} \begin{pmatrix} \hat{\mathbf{k}}_1 \\ \hat{\mathbf{k}}_2 \\ \hat{\mathbf{k}}_3 \end{pmatrix} \Rightarrow \begin{pmatrix} \hat{\mathbf{k}'}_1 \\ 0 \\ \hat{\mathbf{k}'}_3 \end{pmatrix}. \tag{5.11}$$

5.4 Molecular dynamics simulations

A nematic configuration of 512 molecules was taken from the final configuration of the 300 K production run for the C_3-GB-C_7 system (see chapter 4). This system was then doubled up in the x direction to create a new configuration of 1024 molecules in a box of dimension $2 \times 1 \times 1$, with the nematic director aligned along the x axis. After a period of equilibration, simulations were performed in the NVT ensemble with a timestep of 3 fs, at temperatures of 250 K, 300 K, 325 K ,350 K, 375 K and 400 K. All of these temperature lie within the nematic region of the phase diagram (see table 4.2), with 250 K being close to the nematic/solid transition temperature, and 400 K being close to the nematic/isotropic transition temperature.

At each of the temperatures the systems were simulated for 1.3 ns. Coordinate data was collected every 50 steps (150 fs) resulting in 8671 coordinate collections ($\approx$ 3.8 Gbts of data). Two-dimensional histograms of the fluctuation quantities $\hat{Q}_{13}(\mathbf{k})$, $\hat{Q}_{23}(\mathbf{k})$ were tabulated with bin widths set equal to

$$\Delta\mathbf{k'}_1 = \Delta\mathbf{k'}_3 = \frac{2\pi}{\sqrt{(2L)^2 \times L^2 \times L^2}}. \tag{5.12}$$

5.5 Function fitting

A 6 parameter bivariate polynomial was fitted to the low k vector region of the data $(0 \leq k_1^2 \leq 0.1225, 0 \leq k_3^2 \leq 0.1225)$

$$W_{13}(k_1, k_3) = K_{1a}k_1^2 + K_{1b}k_1^4 + K_{1c}k_1^6 + K_{3a}k_3^2 + K_{3b}k_3^4 + K_{3c}k_3^6 \tag{5.13}$$

(with K_{1a} and K_{3a} yielding the splay and bend elastic constants), and

$$W_{23}(k_1, k_3) = K_{2a}k_1^2 + K_{2b}k_1^4 + K_{2c}k_1^6 + K_{3a}k_3^2 + K_{3b}k_3^4 + K_{3c}k_3^6 \tag{5.14}$$

(with K_{2a} and K_{3a} yielding the twist and bend elastic constants). During the analysis the standard deviation of the $\left\langle \left|\hat{Q}_{13}(\mathbf{k})\right|^2 \right\rangle$ and $\left\langle \left|\hat{Q}_{23}(\mathbf{k})\right|^2 \right\rangle$ bins was collected, and this was used in a χ^2 fit. A program was written to minimise the residuals between the collected data and the χ^2 fit using the NAG routine E04JAF.

5.6 Results

The values for the elastic constants obtained from the fitting program are presented in table 5.1. The plots in figures 5.4-5.15 show the surfaces W_{13} and W_{23} for each temperature. From the surfaces it is clear that the linear regime expected at low k vectors only extends to a small region of the data. The surfaces exhibit considerable curvature at higher k values as seen previously in studies of hard ellipsoids [106] and Gay-Berne mesogens [97].

5.7 Discussion

The relatively small size of the simulation box used in this study restricts the data collection at low k vectors. From the plots in figures 5.4-5.15 it can be seen that the low k vector region displays the correct functional form, but the sparsity of data

Temperature / K	K_1 / J m^{-1}	K_2 / J m^{-1}	K_3 / J m^{-1}	Fitting error	$\overline{S_2}$
250	1.76×10^{-11}		9.74×10^{-12}	3%	0.755
		1.36×10^{-11}	2.19×10^{-11}	4%	
300	1.10×10^{-11}		8.86×10^{-12}	5%	0.718
		1.32×10^{-11}	1.99×10^{-12}	5%	
325	9.44×10^{-12}		1.14×10^{-11}	4%	0.693
		1.39×10^{-11}	1.67×10^{-11}	3%	
350	1.25×10^{-11}		1.32×10^{-11}	6%	0.628
		1.31×10^{-11}	1.97×10^{-11}	4%	
375	9.40×10^{-12}		7.29×10^{-12}	5%	0.559
		9.72×10^{-12}	1.71×10^{-11}	5%	
400	7.63×10^{-12}		7.60×10^{-12}	3%	0.442
		1.29×10^{-11}	9.94×10^{-12}	5%	

Table 5.1: Fitted values for elastic constants for C_3-GB-C_7 system in the region $0 \leq k_1^2 \leq 0.1225, 0 \leq k_3^2 \leq 0.1225$ with a 6 parameter fit.

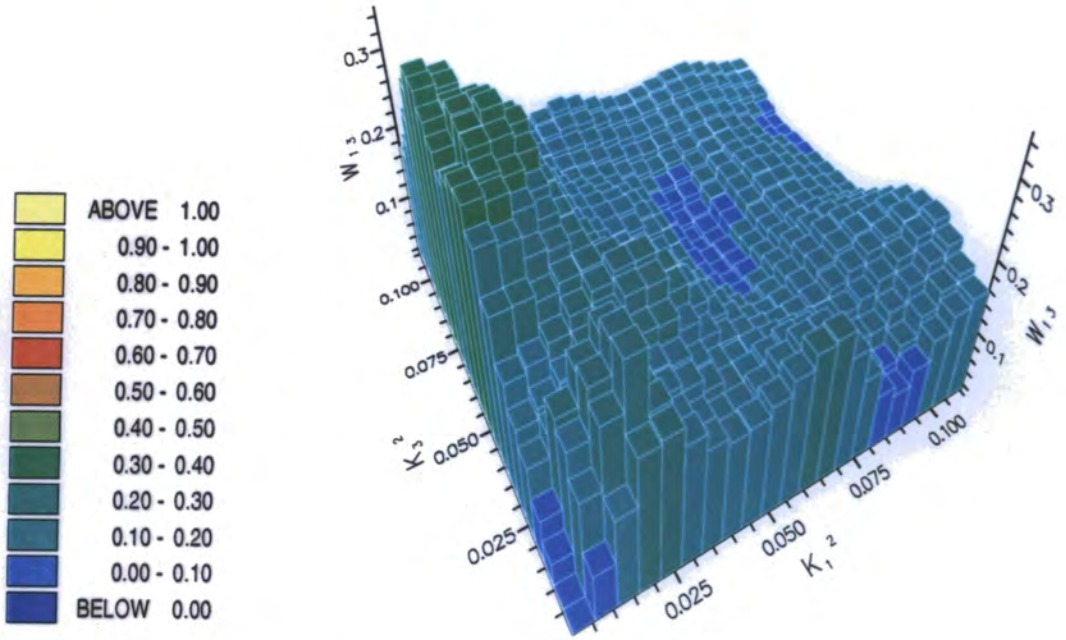

Figure 5.4: W_{13} interpolated landscape at 250 K in the region $0 \leq k_1^2 \leq 0.1225, 0 \leq k_3^2 \leq 0.1225$.

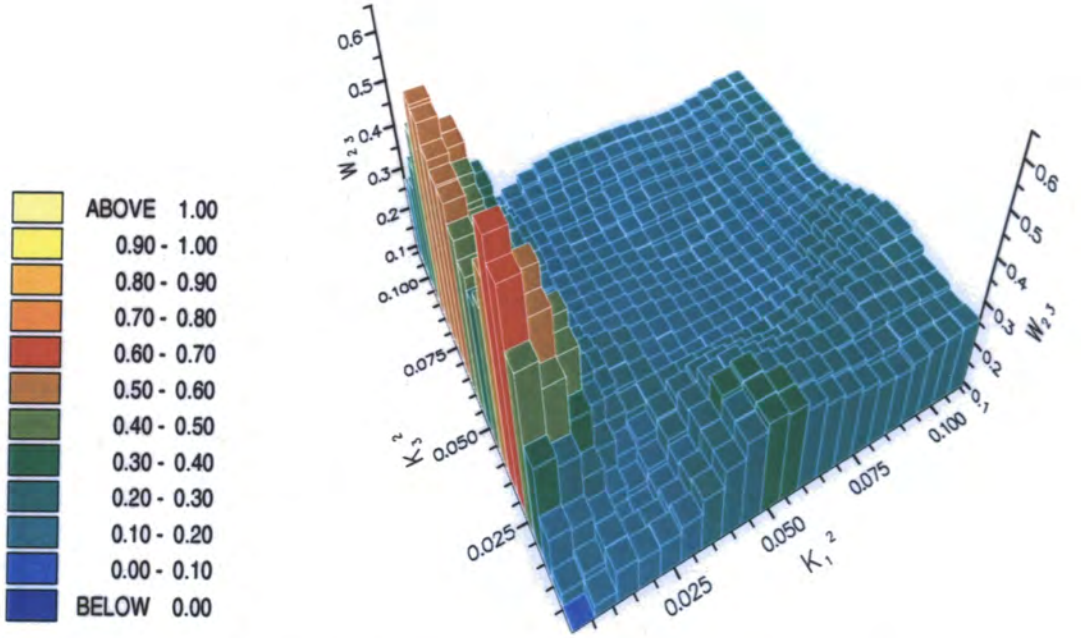

Figure 5.5: W_{23} interpolated landscape at 250 K in the region $0 \leq k_1^2 \leq 0.1225, 0 \leq k_3^2 \leq 0.1225$.

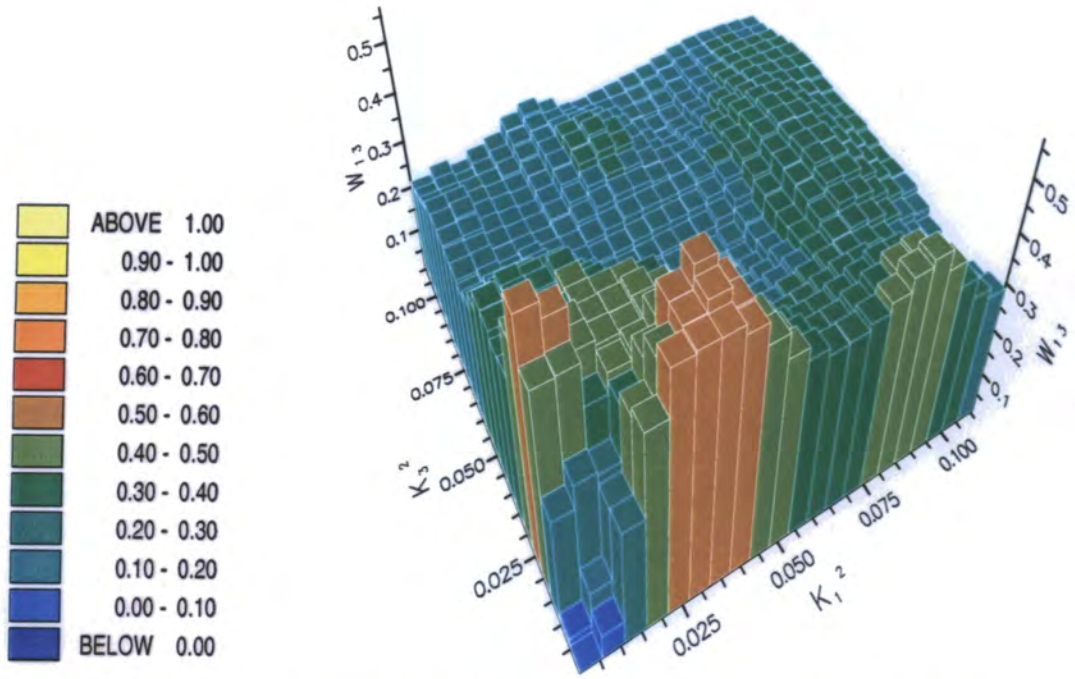

Figure 5.6: W_{13} interpolated landscape at 300 K in the region $0 \leq k_1^2 \leq 0.1225, 0 \leq k_3^2 \leq 0.1225$.

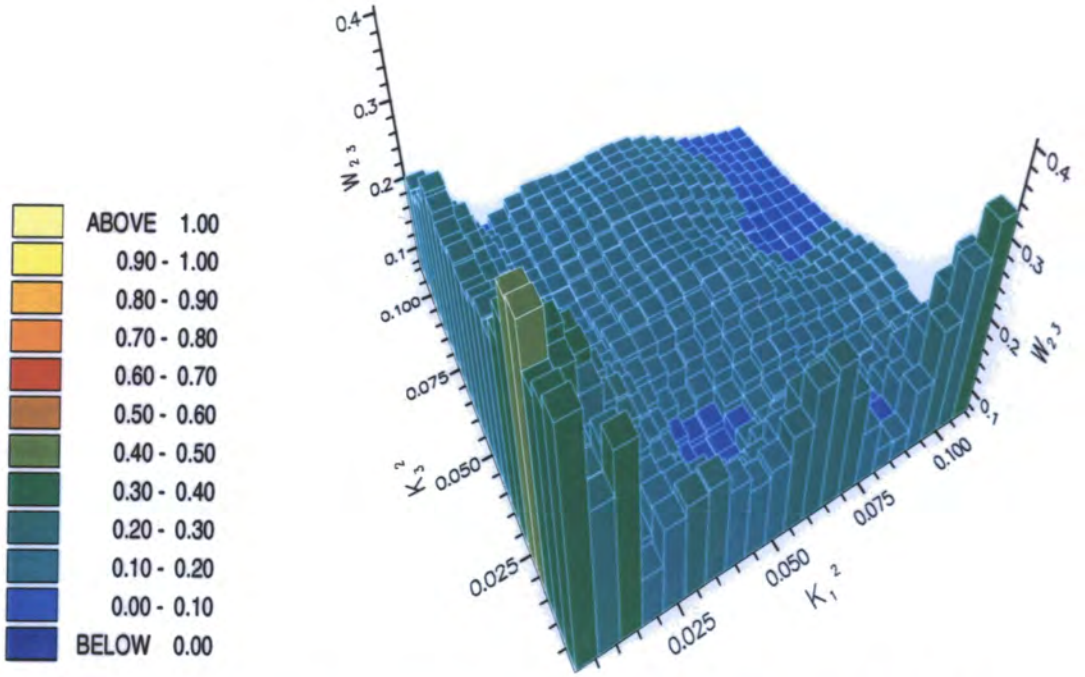

Figure 5.7: W_{23} interpolated landscape at 300 K in the region $0 \leq k_1^2 \leq 0.1225, 0 \leq k_3^2 \leq 0.1225$.

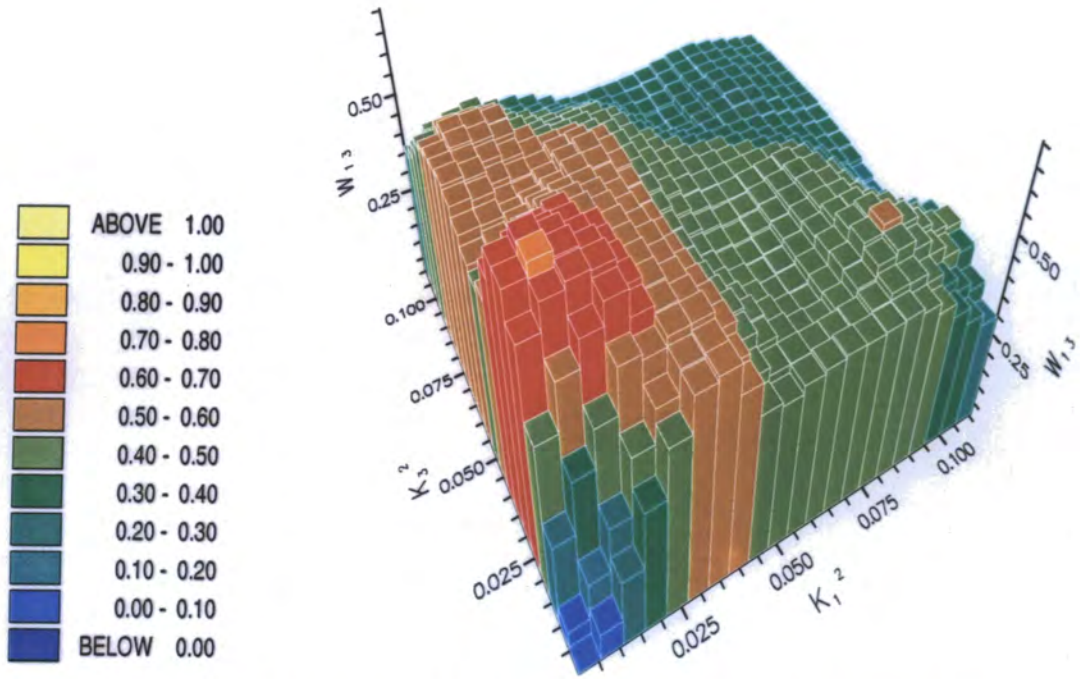

Figure 5.8: W_{13} interpolated landscape at 325 K in the region $0 \leq k_1^2 \leq 0.1225, 0 \leq k_3^2 \leq 0.1225$.

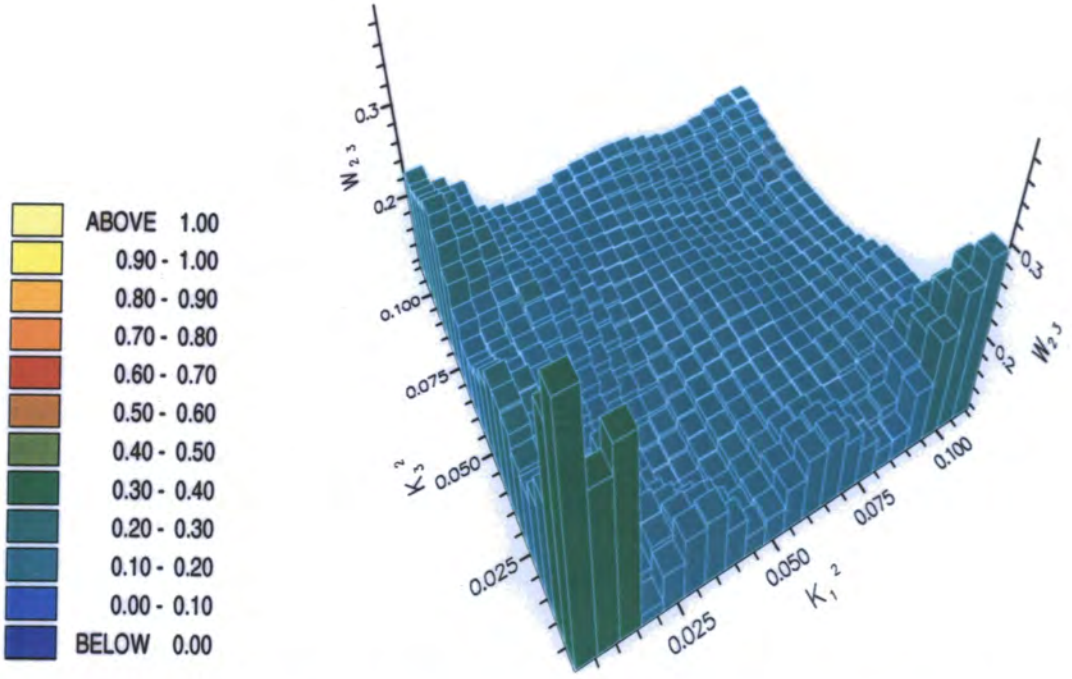

Figure 5.9: W_{23} interpolated landscape at 325 K in the region $0 \leq k_1^2 \leq 0.1225, 0 \leq k_3^2 \leq 0.1225$.

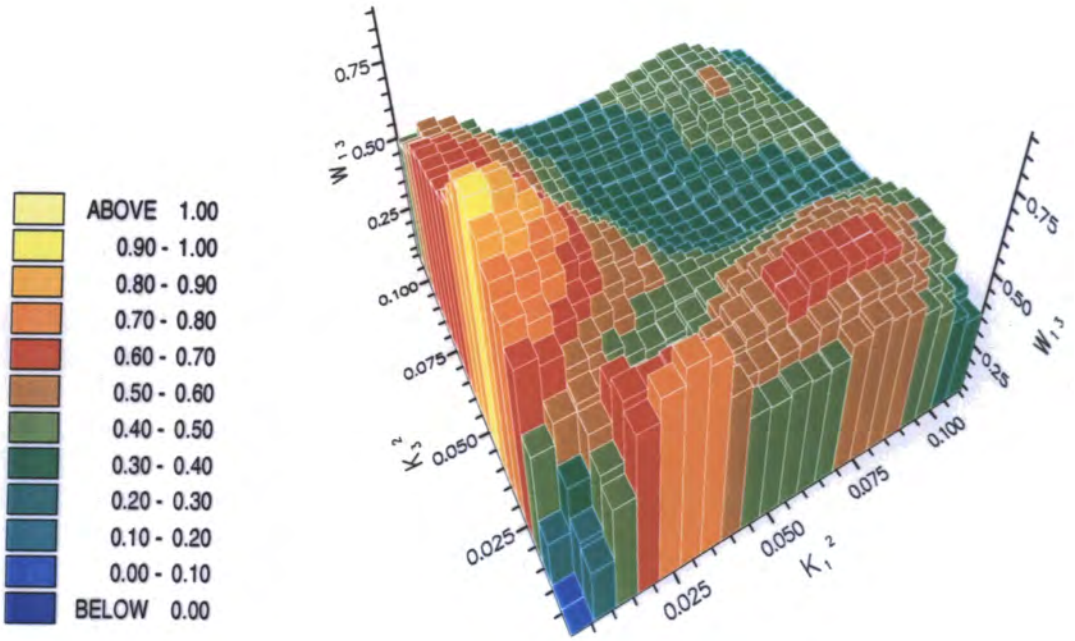

Figure 5.10: W_{13} interpolated landscape at 350 K in the region $0 \leq k_1^2 \leq 0.1225, 0 \leq k_3^2 \leq 0.1225$.

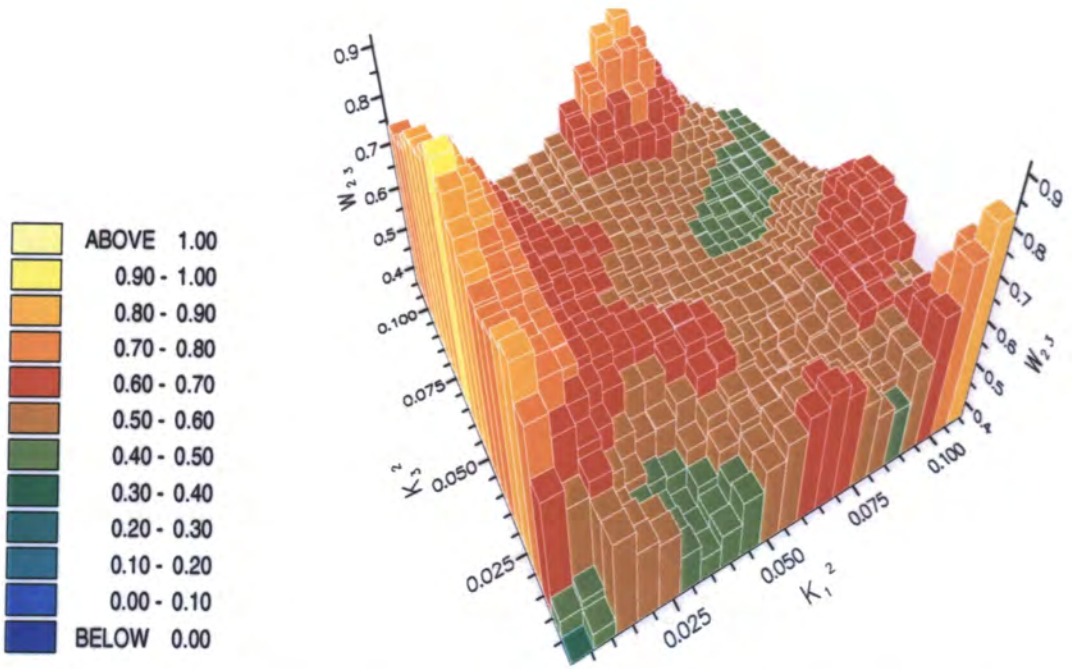

Figure 5.11: W_{23} interpolated landscape at 350 K in the region $0 \leq k_1^2 \leq 0.1225, 0 \leq k_3^2 \leq 0.1225$.

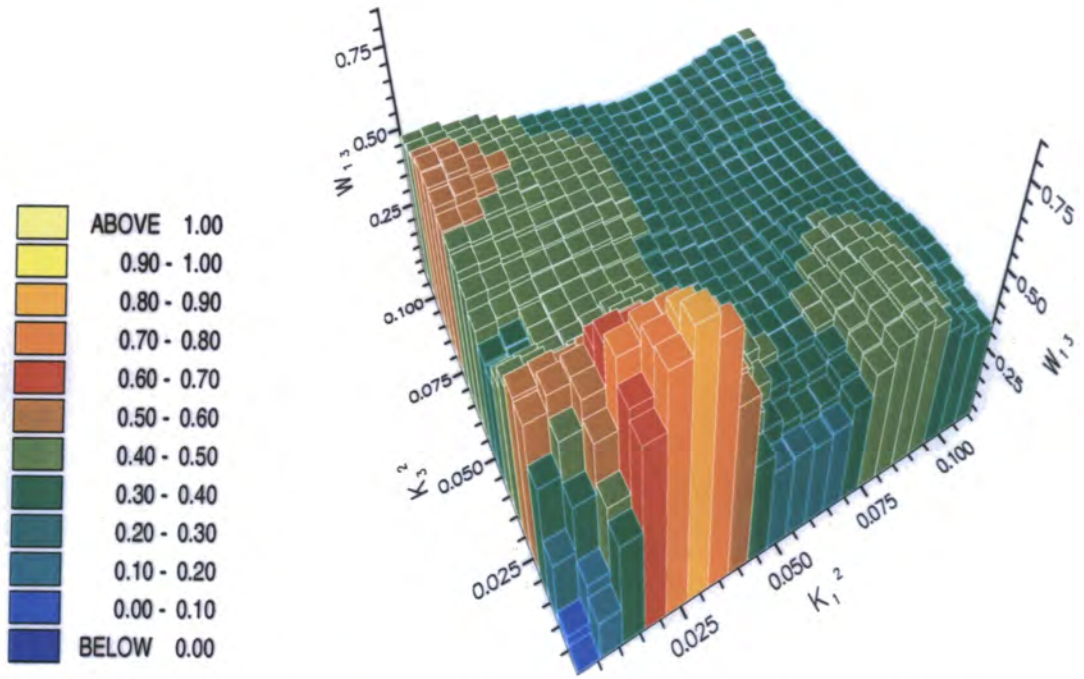

Figure 5.12: W_{13} interpolated landscape at 375 K in the region $0 \leq k_1^2 \leq 0.1225, 0 \leq k_3^2 \leq 0.1225$.

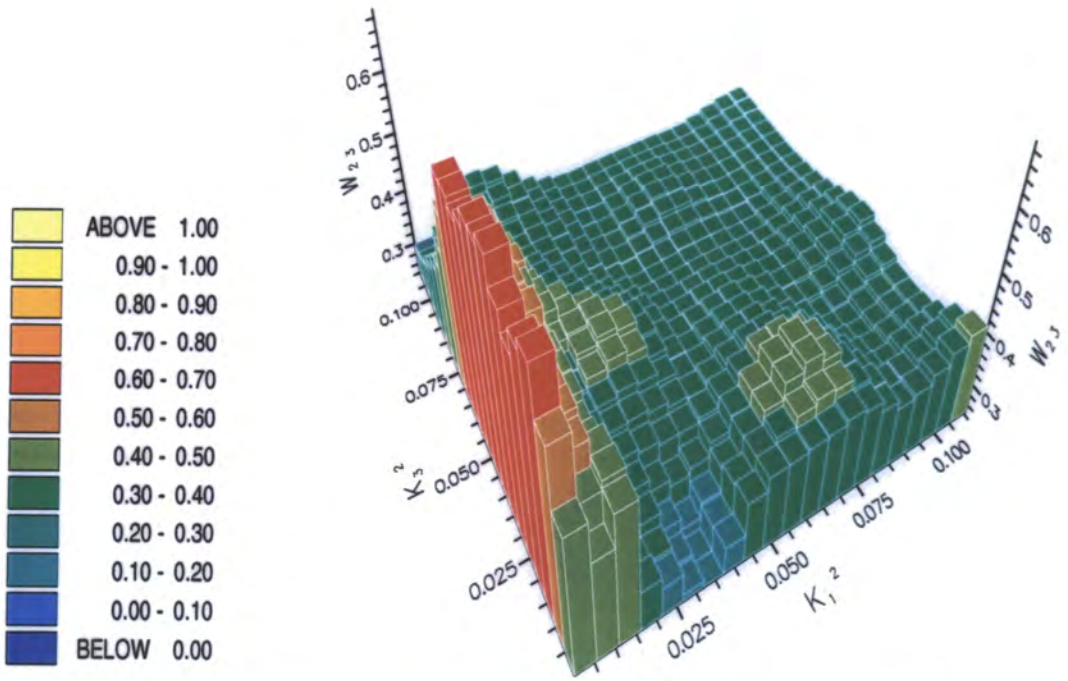

Figure 5.13: W_{23} interpolated landscape at 375 K in the region $0 \leq k_1^2 \leq 0.1225, 0 \leq k_3^2 \leq 0.1225$.

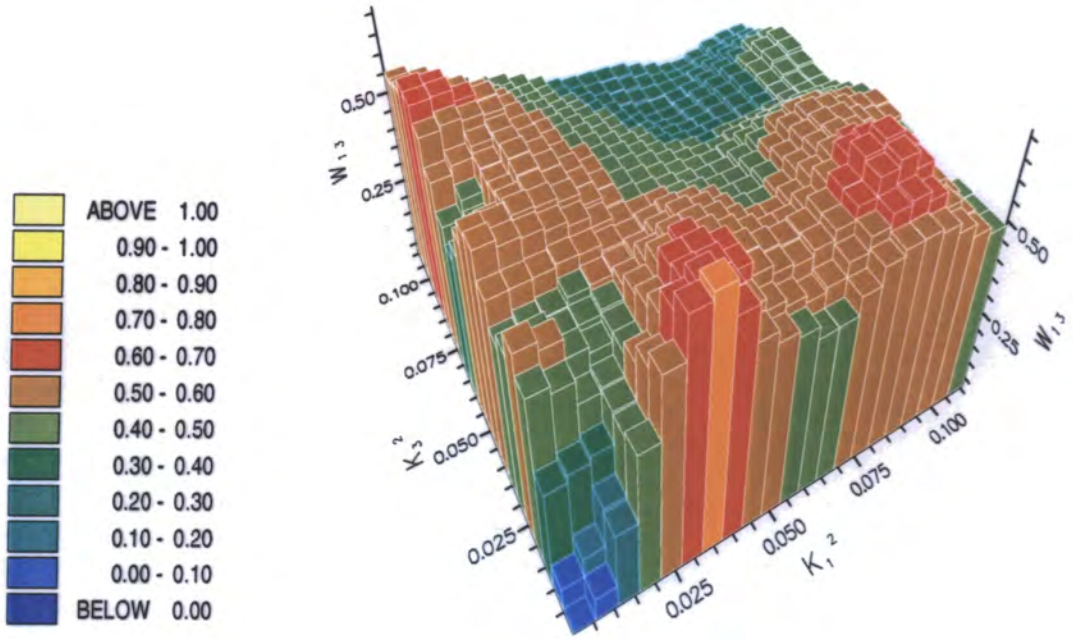

Figure 5.14: W_{13} interpolated landscape at 400 K in the region $0 \leq k_1^2 \leq 0.1225, 0 \leq k_3^2 \leq 0.1225$.

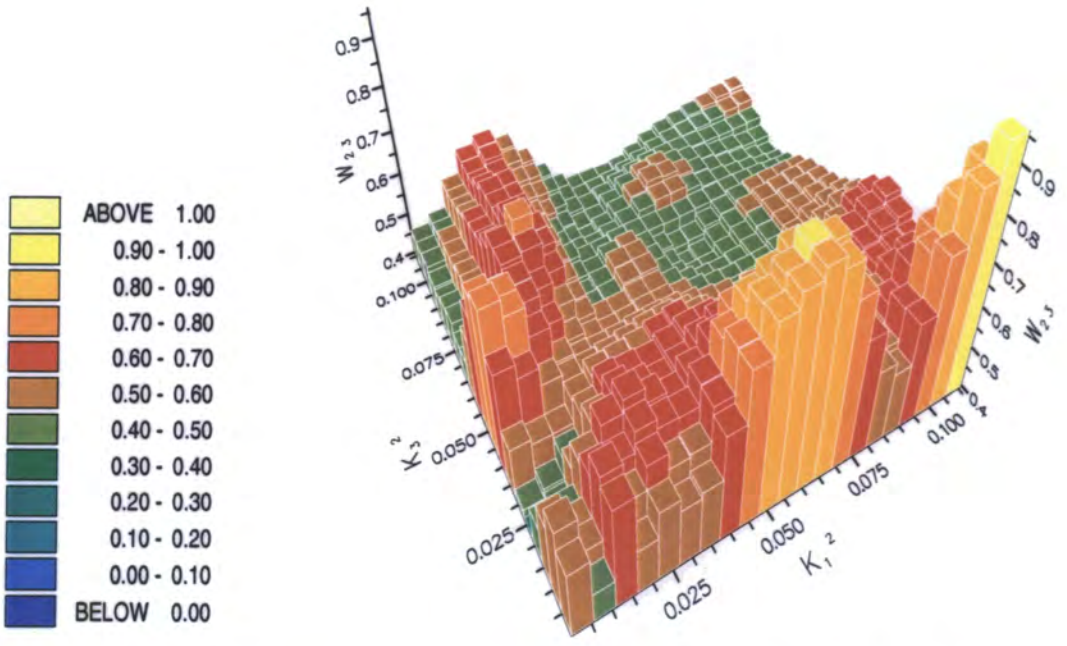

Figure 5.15: W_{23} interpolated landscape at 400 K in the region $0 \leq k_1^2 \leq 0.1225, 0 \leq k_3^2 \leq 0.1225$.

points preclude an accurate fit to the gradient of the curve in this region. Improved statistics may be available from using a slightly smaller bin width, but would be greatly improved in a larger system simulated for longer times. Despite the small linear regime for equations 5.13 and 5.14 the fitted elastic constant results are still encouraging. From a dimensional argument one expects the K values to be of the order of U/l, where U is a typical interaction energy, and l is a molecular length scale. Taking U to be ~ 3 kcal/mol (from typical latent heat values at the clearing temperature), and l to be $\sim$ 20 Å we should expect K_i to be $\sim 1 \times 10^{-11}$ J/m. The results of this study are indeed in this range, and are in the range of typical experimental studies for mesogens with alkyl chains [110–113].

A number of experimental studies have looked at the mesogen MBBA, a molecule with two alkyl chains and a rigid core similar to our model system. In the Rayleigh scattering work of Usui *et al.* [110] for the nematogen MBBA yielded $K_3/K_2 = 2.4 \pm 0.1$ near the solid/nematic transition temperature. This ratio decreased with increasing temperature, a trend that is seen in our results. Haller [111] found a value of 1.25 ± 0.05 for the ratio K_3/K_1 at a temperature of 295 K, whilst Rondelez *et al.* [112] found a ratio of 1.4 ± 0.2 at the same temperature, and Léger [113] found a ratio of 2.89 at the slightly elevated temperature of 296 K. Clearly it is just as difficult to determine the elastic constants experimentally as it is during a simulation of the type described in this chapter. It is predicted from Landau de Gennes expansions of the free energy that the ratio K_3/K_1 will tend to a value of 1 near the nematic/isotropic transition, a result that is seen in our data at 400 K. It is experimentally found that the twist term is always the smallest constant. This has not been observed in this study. However, the theoretical study by Allen *et al.* [97] on a larger system (8000 molecules) of the Gay-Berne ellipsoid at $\mu = 2$, $\nu = 1$, $\rho^* = 0.9$ also gave $K_2 > K_1$. So this result is not

surprising. More data in the very low k vector region would greatly aid more accurate evaluations of the constants.

5.8 Conclusion

The Frank elastic constants K_1, K_2 and K_3 have been calculated from fluctuation expressions for the hybrid Gay-Berne/Lennard-Jones model of C_3-GB-C_7 (described in chapter 4). It is found that the elastic constants are in the experimental range for similar 'real' mesogens and that the value of K_3/K_2 near the solid/nematic transition is in good accord with experiment. It is noted that the number of low k vectors available in this study was severely limited by system size. However, to undertake better studies of the nematic constants would require substantially more disk space ($>$ 100 Gbts) than was available during this work. An obvious extension of the work described here would be the use of a massively parallel computer with large quantities of disk space, allowing one to simulate a much larger system (a system of 4096 C_3-GB-C_7 molecules has been created ready for such a simulation on the Cray T3E), allowing access to the short k vector region for the fluctuation quantities $\hat{Q}_{13}(\mathbf{k})$ and $\hat{Q}_{23}(\mathbf{k})$.

CHAPTER 6

Force field development for siloxane polymers

6.1 Introduction

Siloxane chains are commonly used to provide a flexible polymer backbone for side group liquid crystalline polymers [114]. Siloxane chains are known to be particularly flexible when compared to hydrocarbon chains. However, unlike hydrocarbon systems, which are well described by a number of force fields [49], siloxane systems suffer from poorly developed force fields. Little is known about actual conformation energies, the shape of the torsional potential about a Si-O bond, or the actual height of the barrier to rotation. In a siloxane chain the equilibrium O-Si-O bond angle ($\approx 110°$) is very different from the equilibrium Si-O-Si bond angle ($\approx 141°$). This difference in angle leads to a polymer main chain which, when in the all *trans* conformation, is 'curled

up'. This behaviour is quite different from the behaviour of many other polymer main chains, in which the end-to-end distance increases with the number of *trans* states (for example polyethylene).

In a study of the conformational statistics of poly(dimethylsiloxane) Bahar *et al.* [115, 116] used the rotational isomeric state (RIS) approximation. In the RIS model [117,118] each dihedral angle is treated as if it was in one of several discrete rotational states. This model is most applicable to dihedrals that have distinct rotational minima, separated by barriers substantially greater than RT (0.59 kcal/mol at room temperature). Bahar *et al.* define three states located at torsional angles of 180° (*trans*), 60° ($gauche^-$), and 300° ($gauche^+$). The computational work of Grigoras and Lane [119] does not seem to support this assumption. Grigoras *et al.* have undertaken an *ab initio* study of a number of organosilicon compounds, in order to calculate molecular mechanics force field parameters. In their work they examine a sequence of torsional rotations about Si-O bonds, between the *cis* and *trans* conformations, for different sections of the siloxane chain. Their results show a lack of 3-fold symmetry about all of the investigated torsional rotations.

Although the work of Grigoras *et al.* represents an improvement on the approximation used by Bahar *et al.*, a series of one-dimensional 'cross-sections' through the energy surface may well fail to locate the principle features of the torsional potential. In this chapter a quantum mechanical study is undertaken, in two dimensions, of a siloxane chain fragment disiloxane diol $(HOMe_2Si)_2O$ (figure 6.1). An attempt is made to fit to the resulting potential energy surface, using standard functional forms for the Si-O torsional potential. This potential will be used in future simulations of a side group polymer liquid crystal with a siloxane backbone.

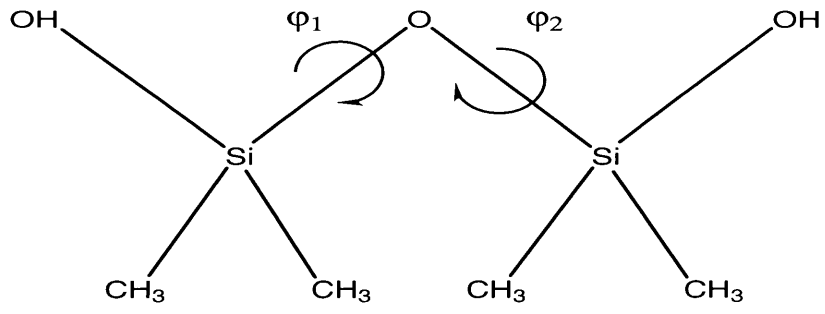

Figure 6.1: Disiloxane diol $(HOMe_2Si)_2O$.

6.2 Methodology

6.2.1 Hartree-Fock Molecular Orbital theory

We wish to solve the Schrödinger equation for a molecule

$$\hat{H}\Psi = E\Psi \tag{6.1}$$

where $\hat{H}$ is the Hamiltonian, Ψ is the wavefunction of the molecule, and E is the energy. For a system of n electrons of mass m_e, and N nuclei, the Hamiltonian of the molecule is given by

$$\hat{H} = -\sum_{i=1}^{n} \frac{h^2}{8\pi^2 m_e}\nabla_i^2 - \sum_{i=1}^{n}\sum_{\alpha=1}^{N} \frac{Z_\alpha e^2}{4\pi\epsilon_0 r_{i\alpha}} + \sum\sum_{i<j}^{n} \frac{e^2}{4\pi\epsilon_0 r_{ij}} \tag{6.2}$$

where the electron/nuclei distances are given by $r_{i\alpha}$, the inter electron separation is given by $r_{ij} = |\mathbf{r}_i - \mathbf{r}_j|$ and Z_α is the number of protons for nucleus α. The Schrödinger equation with this Hamiltonian is not analytically soluble. However it can be solved using numerical methods.

If the third term, the electron-electron repulsion term, is omitted from equation 6.2 we now have an expression that is equivalent to a set of n one-electron Schrödinger equations of the form

$$\hat{h}_i\psi_i = E_i\psi_i. \tag{6.3}$$

The spin-orbitals ψ_i (one electron orbitals that contain a spatial and a spin description)

can be written as a linear combination of single electron orbitals (LCAO)

$$\psi_i = \sum_{\nu=1}^{K} c_{\nu i}\phi_\nu \tag{6.4}$$

where ϕ_ν are one-electron orbitals known as *basis functions*, and the collection $\nu = 1, K$ constitute a *basis set.* A minimum basis set is one which has enough basis functions to accommodate all of the electrons within the molecule. The solution to equation 6.3 is given by the solution to the set of secular equations

$$\begin{array}{cccc} (H_{11} - ES_{11}) & + (H_{12} - ES_{12}) + & \ldots & + (H_{1K} - ES_{1K}) = 0 \\ \cdot & \cdot & \cdot\ \cdot\ \cdot & \cdot \\ \cdot & \cdot & \cdot\ \cdot\ \cdot & \cdot \\ \cdot & \cdot & \cdot\ \cdot\ \cdot & \cdot \\ (H_{K1} - ES_{K1}) & + (H_{K2} - ES_{K2}) + & \ldots & + (H_{KK} - ES_{KK}) = 0 \end{array} \tag{6.5}$$

with

$$H_{\alpha\beta} = \int \phi_\alpha^* \, \hat{h} \, \phi_\beta \, d\tau. \tag{6.6}$$

This can readily be achieved with little expenditure of computer time and the solutions for E and ψ_i provide molecular orbital theory results that are qualitatively correct.

For more quantitative results, electron-electron repulsion in equation 6.2 cannot be omitted. In the Hartree-Fock approach the one electron operator $\hat{h_i}$ in equation 6.3 is replaced by the Fock operator $\hat{F}$

$$\hat{F_i} = \hat{h_i} + \sum_j \left[2\hat{J_j} - \hat{K_j}\right], \tag{6.7}$$

where $\hat{J}$ and $\hat{K}$ respectfuly represent the Coulomb and exchange operators arising from electron-electron interactions. The secular equations now involve matrix elements

$$F_{\alpha\beta} = \int \phi_\alpha^* \, \hat{F} \, \phi_\beta \, d\tau. \tag{6.8}$$

which include the coefficients from equation 6.4, and must therefore be solved via a self-consistent field (SCF) approach. One first finds a trial solution for the spin orbitals

by making an initial guess for the coefficients $c_{\nu i}$ in equation 6.5 (with $H_{\alpha\beta}$ replaced by $F_{\alpha\beta}$). This trial solution is then used in equation 6.3 (with $\hat{h}_i$ replaced by $\hat{F}_i$). This provides a new set of spin orbitals with new coefficients. This process is iterative, converging on a self-consistent solution.

As more basis functions are added to equation 6.4 the energy converges closer to the true solution. In the *Hartree-Fock limit* (H-F) the addition of further basis functions no longer reduces the energy of the system.

In the SCF method each electron is assumed to be moving in an average potential created by the other electrons. This does not account for the fact that electron motion is correlated to the motion of the other electrons, and therefore leads to a difference between the exact energy of the system and that of the H-F energy.

6.3 Results and Discussion

6.3.1 *Ab initio* conformational landscape

The computer program Gaussian94 [58] was used for the *ab initio* calculation of the conformational landscape of the siloxane fragment shown in figure 6.1. The structure of the fragment was first optimised using a STO-3G* basis set. The STO-3G basis set is a minimal basis set of Slater type orbitals (STO's), created from three Gaussian functions. In order to account for anisotropic charge distributions, polarisation functions were added to the basis sets used to describe the carbon, oxygen and silicon atoms (indicated by * in the basis set description). A relaxed geometry scan was then performed on the two dihedral angles O-Si-O-Si (ϕ_1) and Si-O-Si-O (ϕ_2). In a relaxed geometry scan, the dihedrals ϕ_1 and ϕ_2 are fixed at the chosen values, whilst the rest of the molecular geometry is energy minimised (see Appendix C). Due to the symmetry of the fragment the scan range was chosen to be $-180° \leq \phi_1 \leq 180°$, $-180° \leq \phi_2 \leq 180°$ in steps of 10°.

The resulting conformational landscape is plotted in figure 6.2. The difference between the maximum and the minimum quantum mechanical energy in figure 6.2 is extremely small, $\approx$ 2.2 kcal mol^{-1} ($\approx$ 9.2 kJ mol^{-1}). This is much smaller than the barriers to rotation in hydrocarbon chains ($\approx$ 3 kcal mol^{-1} *trans-gauche* energy barrier, $\approx$ 4.5 kcal mol^{-1} *gauche-gauche* energy barrier [120]) and indicates that almost free rotation can occur about the Si-O bond at room temperature. The RIS description based on three energy minima for a torsional angle is clearly an unsuitable model for the Si-O bond.

The energy minimised structure of the disiloxane fragment is given in table 6.1 alongside results from an X-ray crystal structure [121]. There is a good agreement between the *ab initio* results and the X-ray data. The small differences that do exist between the solid state X-ray data and the STO-3G* data are probably due to a hydrogen bonded network that is thought to exist in the crystal structure of $(HOMe_2Si)_2O$.

6.3.2 MM3 Conformational Energy Landscape

Using the computational chemistry package CAChe 3.1 (Oxford Molecular Group) a set of molecular mechanics MM3 energy minimisations were performed on the siloxane fragment to find the energy minimised structure. MM3 is the most widely used molecular mechanics program and considerable work has been carried out to parameterise the MM3 force field for a wide range of molecules [49].

The results for the MM3 energy minimised structure are given in table 6.1. A relaxed scan was then performed about dihedrals ϕ_1 and ϕ_2 between -180 degrees and 180 degrees in 5° intervals to create a conformational energy landscape as shown in figure 6.3. The conformation of lowest energy is that of $\phi_1 = -180°$ and $\phi_2 = -180°$. It can be seen from table 6.1 that the molecular mechanics yields reasonable results for the bond angles. However the results for the dihedral angle bears no resemblance to

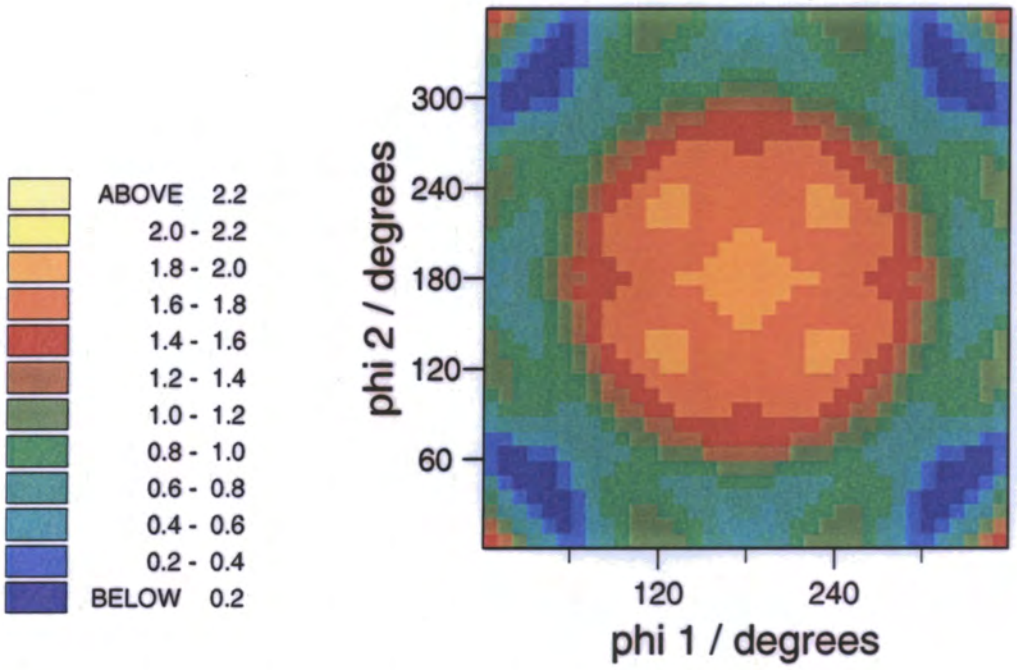

Figure 6.2: STO-3G* conformational energy landscape of the siloxane fragment, disiloxane diol, for rotation about dihedrals ϕ_1 and ϕ_2. Energy units in kcal/mol.

Bond angle		$\theta°$	
	MM3	STO-3G*	X-ray
$(O\text{-}Si\text{-}O)_1$	113.4	106.7	110.0
$(O\text{-}Si\text{-}O)_2$	113.4	106.8	109.6
Si-O-Si	144.4	137.2	141.4
Dihedral angle		$\phi°$	
	MM3	STO-3G*	X-ray
O-Si-O-Si	180.0	39.5	45.79
Si-O-Si-O	180.0	38.8	39.23

Table 6.1: Structural data for $(HOMe_2Si)_2O$. Columns 1 and 2 refer to energy minimised conformations. Column 3 refers to the crystallographic data from reference [121].

the *ab initio* or to the X-ray data. This is due to the fact that the torsional potential in the MM3 is assigned the parameters V_1= 0.00, V_2= 0.00, V_3= 0.10 kcal/mol. It is the $\cos 3\phi$ term that is the main influence on the potential energy surface plotted in figure 6.3, and this is clearly in error compared to the *ab initio* data of section 6.3.1.

6.3.3 Fitting to the *ab initio* potential energy surface

It is highly desirable to obtain improved torsional Si-O potentials for classical molecular mechanics, or molecular dynamics studies, of siloxane polymers. In most classical force fields the potential for rotation about a bond is represented by a 1,4-nonbonded interaction and a torsional expression. In the siloxane fragment studied here the 1,4-nonbonded interactions are small and can safely be neglected in fitting to a functional form. In view of this a fit was attempted to the *ab initio* data using three well known functional forms; the MM3 [49], the AMBER [43] and the Ryckaert-Bellemans [55] potentials. A computer program was written that implemented the NAG routine E04JAF, which sought to minimise the square of the difference between the fitted functional form and the *ab initio* results. The program returned the minimised values for the parameters and the residual (the sum of the square of the differences).

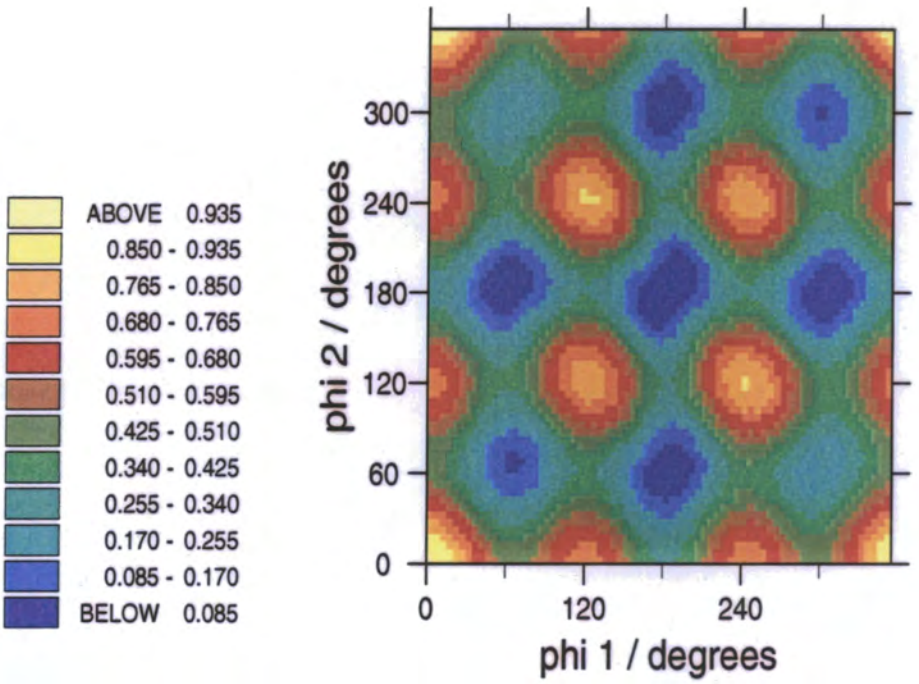

Figure 6.3: MM3 conformational energy landscape of the siloxane chain for rotation about dihedrals ϕ_1 and ϕ_2. Energy units in kcal/mol.

V_1	-0.369477
V_2	0.571860
V_3	0.738576
γ_1	-105.813°
γ_2	-103.290°
γ_3	180.156°
Residual	392.765909

Table 6.2: Fitted parameters and residual for the AMBER potential. V_1, V_2 and V_3 are in kcal/mol, γ_1, γ_2 and γ_3 are in radians.

For disiloxane diol the potential energy surface $E(\phi_1, \phi_2)$ can be written as a sum of two identical torsional potentials involving ϕ_1 and ϕ_2. In the AMBER [43] force field this can be represented as

$$E(\phi_1,\phi_2) = \frac{V_1}{2}(1+(\cos\phi_1-\gamma_1)) + \frac{V_2}{2}(1+(\cos 2\phi_1-\gamma_2)) + \frac{V_3}{2}(1+(\cos 3\phi_1-\gamma_3)) + \frac{V_1}{2}(1+(\cos\phi_2-\gamma_1)) + \frac{V_2}{2}(1+(\cos 2\phi_2-\gamma_2)) + \frac{V_3}{2}(1+(\cos 3\phi_2-\gamma_3)) \quad (6.9)$$

Similarly, using the MM3 [49] potential, $E(\phi_1, \phi_2)$ can be written

$$E(\phi_1,\phi_2) = \frac{V_1}{2}(1+\cos\phi_1) + \frac{V_2}{2}(1-\cos 2\phi_1) + \frac{V_3}{2}(1+\cos 3\phi_1) + \frac{V_1}{2}(1+\cos\phi_2) + \frac{V_2}{2}(1-\cos 2\phi_2) + \frac{V_3}{2}(1+\cos 3\phi_2). \quad (6.10)$$

Finally, using the Ryckaert-Bellemans [55] form for the potential, $E(\phi_1, \phi_2)$ is represented in terms of a power series in $\cos\phi_1$, $\cos\phi_2$

$$E(\phi_1,\phi_2) = \frac{V_1}{2} + V_2\cos\phi_1 + V_3\cos^2\phi_1 + V_4\cos^3\phi_1 + V_5\cos^4\phi_1 + V_6\cos^5\phi_1 + \frac{V_1}{2} + V_2\cos\phi_2 + V_3\cos^2\phi_2 + V_4\cos^3\phi_2 + V_5\cos^4\phi_2 + V_6\cos^5\phi_2. \quad (6.11)$$

V_1	-0.350012
V_2	0.549527
V_3	0.75802
Residual	399.537663

Table 6.3: Fitted parameters and residual for the MM3 potential. V_1, V_2 and V_3 are in kcal/mol.

Using these functional forms in the fitting program yields the parameters given in tables 6.2-6.4.

Of the three functional forms used the Ryckaert-Bellemans form provides the lowest residuals when fitted to $E(\phi_1, \phi_2)$. A plot of the minimised function is given in figure 6.4. The fitted Ryckaert-Bellemans potential produces a minima at ϕ_1=38.8°, ϕ_2=41.0° of 0.12 kcal/mol, a value extremely close to the global minima found in the *ab initio* study, and a maxima at ϕ_1=138.8°, ϕ_2=141.0° of 1.75 kcal/mol. In figure 6.5 a plot is made of the difference at each point from the fit and the STO-3G* calculation. The majority of the surface is fitted well, but this is a problem at the point ϕ_1=1.2°, ϕ_2=1.0°, corresponding to the *cis-cis* conformation, with a difference of 0.86 kcal/mol below the STO-3G* result, and at ϕ_2=178.7°, ϕ_2=1.0°, corresponding to the *cis-trans* conformation, with a difference of 0.58 kcal/mol above the STO-3G* result. This indicates that the fitted Ryckaert-Bellemans potential would promote more *cis-cis* conformations, and fewer *cis-trans* conformations. The MM3 molecular mechanics results clearly fail to predict the correct form of the potential energy surface. This is due to the fact that the MM3 potential is only able to create minima that are at intervals of 60°. It can be seen that the fit allowed by the Ryckaert-Bellemans potential has a

V_1	1.250025
V_2	-0.722631
V_3	-0.584082
V_4	0.143431
V_5	0.533889
V_6	0.310225
Residual	66.033761

Table 6.4: Fitted parameters and residual for the Ryckaert-Bellemans potential. V_1 through to V_6 are in kcal/mol.

significantly smaller residual than that allowed by either the AMBER or MM3 functions. The extension of the AMBER and MM3 torsional potentials to include higher order terms in the Fourier expansion has also been investigated. It is found that $\cos 6\phi$ terms are required to approach the quality of the Ryckaert-Bellemans fit.

6.4 Conclusions

In this chapter an *ab initio* potential energy surface corresponding to rotation about the two dihedral angles, ϕ_1 and ϕ_2, of disiloxane diol has been calculated. The *ab initio* data has been fitted to a number of standard functional forms commonly used to describe torsional potentials. Our results show that the barriers to rotation about the Si-O bond are very small ($\approx$ 2.2 kcal/mol).

Recently *ab initio* calculations of molecular force fields have been taken up in earnest in the literature. A series of *ab initio* studies have been carried out by Jorgensen *et al* [122] and used to fit a number of torsional potentials for organic molecules to

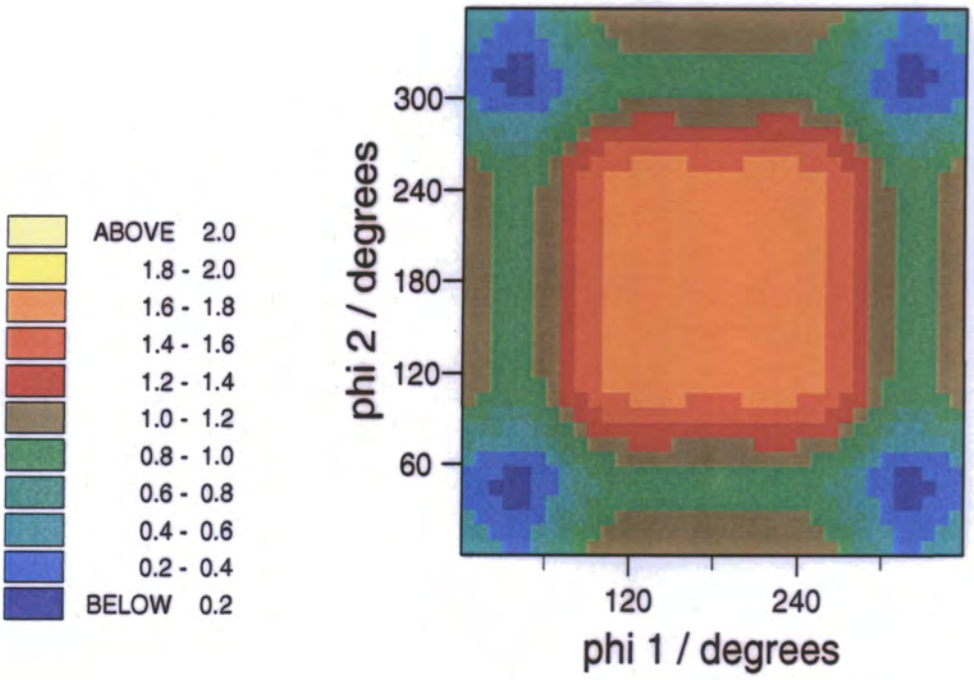

Figure 6.4: Fitted conformational energy landscape of the siloxane fragment for rotation about dihedrals ϕ_1 and ϕ_2 using the Ryckaert-Bellemans potential. Energy units in kcal/mol.

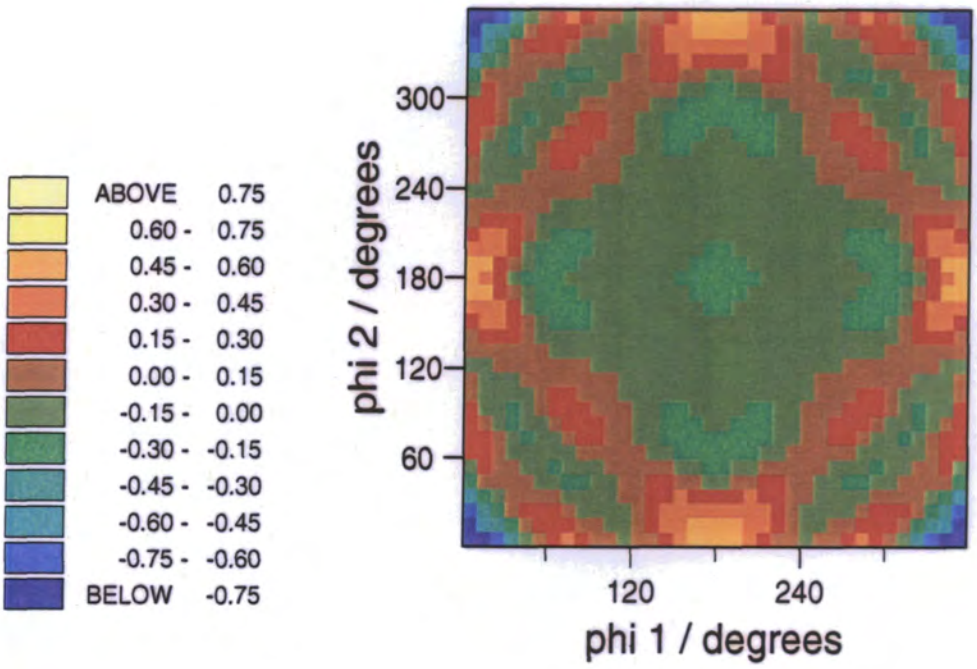

Figure 6.5: Difference between STO-3G* data and fitted conformational energy landscape of the siloxane fragment for rotation about dihedrals ϕ_1 and ϕ_2. Energy units in kcal/mol.

parameterise the OPLS force field. This approach has also been used by Halgren and Nachbar in the development of the Merck molecular force field MMFF [123–127]. Clearly there is great scope for further development of this method using high quality quantum chemical calculations, as used in recent DFT studies [56, 93].

CHAPTER 7

Conclusion

The work in this thesis describes computer simulation studies of liquid crystal phases. The results in chapter 3 describe the first atomistic study to show the growth of a liquid crystal phase from an isotropic liquid. The work demonstrates considerable coupling between orientational ordering and molecular shape, but indicates that the coupling between molecular conformational changes and molecular reorientation is relatively weak.

The employment of the Gay-Berne potential in the model simulated in chapter 4 provided a substantial saving in computer time over the fully atomistic model and allowed the study of a much larger system size. A further step forward in simulations of hybrid models would be the use of multi-time step algorithms [128] (not currently available in GB-MOL). These could decouple the (relatively) slow orientational motion of the Gay-Berne particle from the faster intramolecular bending and torsional motion allowing substantially faster simulation times. Much more use could be also made of

forms of the Gay-Berne potential [96] that are capable of modeling biaxial core units, such as biphenyl or bicyclohexyl groups.

The calculations of nematic elastic constants in chapter 5 show that there is a real role for simulation of 'realistic' mesogenic materials leading to physical parameters that are of genuine interest to industry. This is likely to lead to further fruitful collaborations between industry and academia.

The work on force field development in chapter 6 has led to an improved torsional potential for the siloxane polymer back-bone, and the results presented will be incorporated in future simulations of siloxane-based polymers.

With the ever increasing speed and storage capacity of modern workstations simulations of the kind described in this thesis are becoming ever more accessible, and the systems that are open to simulation will become more and more complex. There will be no problem making use of the latest computer technology; larger system sizes, longer run times and more detailed force fields will greatly enhance the predictive capabilities of computer simulations of liquid crystals.

BIBLIOGRAPHY

[1] F. Reinitzer. *Monatshefte fur Chemie*, 9:421, 1888.

[2] F. Reinitzer. *Liq. Cryst.*, 5:7, 1989.

[3] G. Friedel. *Anales Physique*, 18:273, 1922.

[4] J. W. Goodby and G. W. Gray. Guide to the nomenclature and classification of liquid crystals. In D. Demus, J. Goodby, G. W. Gray, H.-W. Spiess, and V. Vill, editors, *Handbook of Liquid Crystals*, volume 1, chapter II. Wiley-VCH, Weinheim, 1998.

[5] G. W. Gray and J. W. Goodby. *Smectic liquid crystals: Textures and Structures.* Leonard Hill, 1984.

[6] J. W. Goodby. High molecular weight liquid crystals. In D. Demus, J. Goodby, G. W. Gray, H.-W. Spiess, and V. Vill, editors, *Handbook of Liquid Crystals*, volume 3. Wiley-VCH, Weinheim, 1998.

[7] H. Bengs, H. Finkelmann, J. Kupfer, H. Ringsdorf, and P. Schuhmacher. *Macromol. Chem., Rapid Commun.*, 14:445, 1993.

[8] S. Disch, H. Finkelmann, H. Ringsdorf, and P. Schuhmacher. *Macromolecules*, 28:2424, 1995.

[9] W. Maier and A. Saupe. *Z. Naturforsch A*, 13:564, 1958.

[10] D. Brindle and C. M. Care. *J. Chem. Soc. Faraday Transactions*, 88:2163, 1992.

[11] J. C. Desplat and C. M. Care. *Molec. Phys.*, 87:441, 1996.

[12] P. A. Lebwhol and G. Lasher. *Phys. Rev. A*, 6:426, 1972.

[13] A. Stroobants, H. N. W. Lekkerkerker, and D. Frenkel. *Phys. Rev. Lett.*, 57:1452, 1986.

[14] D. Frenkel, H. N. W. Lekkerkerker, and A. Stroobants. *Nature*, 332:822, 1988.

[15] J. Vieillard-Baron. *J. Chem. Phys.*, 56:4729, 1972.

[16] J. Vieillard-Baron. *Molec. Phys.*, 28:809, 1974.

[17] D. Frenkel and B. M. Mulder. *Phys. Rev. Lett.*, 52:287, 1984.

[18] D. Frenkel and B. M. Mulder. *Molec. Phys.*, 55:1171, 1985.

[19] B. J. Berne and P. Peckukas. *J. Chem. Phys.*, 64:4213, 1972.

[20] J. G. Gay and B. J. Berne. *J. Chem. Phys.*, 74:3316, 1981.

[21] C. McBride, M. R. Wilson, and J. A. K. Howard. *Molec. Phys.*, 93:955, 1998.

[22] M. R. Wilson. *J. Chem. Phys.*, 107:8654, 1997.

[23] M. R. Wilson and M. P. Allen. *Molec. Cryst. Liq. Cryst.*, 198:465, 1991.

[24] M. R. Wilson and M. P. Allen. *Liq. Cryst.*, 12:157, 1992.

[25] M. R. Wilson. *J. Molec. Liq.*, 68:23, 1996.

[26] A. V. Komolkin, Yu. V. Molchanov, and P. P. Yakutseni. *Liq. Cryst.*, 6:39, 1989.

[27] S. J. Picken, W. F. van Gunsteren, P. Th. van Duijnen, and W. H. de Jeu. *Liq. Cryst.*, 6:357, 1989.

[28] B. Jung and B. L. Schürmann. *Molec. Cryst. Liq. Cryst.*, 185:141, 1990.

[29] I. Ono and S. Kondo. *Molec. Cryst. Liq. Cryst.*, 8:69, 1991.

[30] I. Ono and S. Kondo. *Bull. Chem. Soc. Jpn.*, 65:1057, 1992.

[31] I. Ono and S. Kondo. *Bull. Chem. Soc. Jpn.*, 66:633, 1993.

[32] G. Krömer, D. Paschek, and A. Geiger. *Ber. Bunsenges Phys. Chem.*, 97:1188, 1993.

[33] J. Huth, T. Mosell, K. Nicklas, A. Sariban, and J. Brickmann. *J. Phys. Chem.*, 98:768, 1994.

[34] C. W. Cross and B. Fung. *J. Chem. Phys.*, 101:6839, 1994.

[35] M. Yoneya and H. J. C. Berendsen. *J. Phys. Soc. Jpn.*, 63:1025, 1994.

[36] A. V. Kolmolkin, A. Laaksonen, and A. Maliniak. *J. Chem. Phys.*, 101:4103, 1994.

[37] S. Y. Yakovenko, A. A. Muravski, G. Kromer, and A. Geiger. *Molec. Phys.*, 86:1099, 1995.

[38] S. Y. Yakovenko, G. Kromer, and A. Geiger. *Molec. Phys.*, 275:91, 1996.

[39] S. Hauptmann, T. Mosell, S. Reiling, and J. Brickmann. *Chem. Phys.*, 208:57, 1996.

[40] A. V. Lyulin, M. S. Al Barwani, M. P. Allen, M. R. Wilson, I. Neelov, and N. K. Allsopp. *Macromolecules*, 31:4626, 1998.

[41] M. Karplus B. R. Gelin. *Biochemistry*, 18:1256, 1979.

[42] B. R. Brooks, R. E. Bruccoleri, B. D. Olafson, , D. J. States, S. Swaminathan, and M. Karplus. *J. Comput. Chem.*, 4:187, 1983.

[43] S. J. Weiner, P. A. Kollman, D. A. Case, U. C. Singh, C. Ghio, G. Alagona, S. Profeta, and P. Weiner. *J. Am. Chem. Soc.*, 106:765, 1984.

[44] W. D. Cornell, P. Cieplak, C. I. Bayly, I. R. Gould, K. M. Merz Jr., D. M. Ferguson, D. C. Spellmeyer, T. Fox, J. W. Caldwell, and P. A. Kollman. *J. Am. Chem. Soc.*, 117:5179, 1995.

[45] W. L. Jorgensen, D. S. Maxwell, and J. Tirado-Rives. *J. Am. Chem. Soc.*, 118:11225, 1996.

[46] W. L. Jorgensen and N. A. McDonald. *Theochem - J. Molec. Structure*, 424:145, 1998.

[47] N. L. Allinger, M. T. Tribble, M. A. Miller, and D. H. Wertz. *J. Am. Chem. Soc.*, 93:1637, 1971.

[48] N. L. Allinger. *J. Am. Chem. Soc.*, 99:8127, 1977.

[49] N. L. Allinger, Y. H. Yuh, and J. Lii. *J. Am. Chem. Soc.*, 111:8551, 1989.

[50] N. L. Allinger, K. S. Chen, and J. H. Lii. *J. Comput. Chem.*, 17:642, 1996.

[51] N. Nevins, K. S. Chen, and N. L. Allinger. *J. Comput. Chem.*, 17:669, 1996.

[52] N. Nevins, J. H. Lii, and N. L. Allinger. *J. Comput. Chem.*, 17:695, 1996.

[53] N. Nevins and N. L. Allinger. *J. Comput. Chem.*, 17:730, 1996.

[54] N. L. Allinger, K. S. Chen, and G. M. Anstead J. A. Katzenellenbogen, S. R. Wilson. *J. Comput. Chem.*, 17:747, 1996.

[55] J. P. Ryckaert and A. Bellemans. *Chem. Phys. Lett.*, 30:123, 1975.

[56] S. J. Clark, C. J. Adam, D. J. Cleaver, and J. Crain. *Liq. Cryst.*, 22:477, 1997.

[57] S. J. Clark, G. J. Ackland, and J. Crain. *Europhys. Lett.*, 44:578, 1998.

[58] M. J. Frisch, G. W. Trucks, H. B. Schlegel, P. M. W. Gill, B. G. Johnson, M. A. Robb, J. R. Cheeseman, T. Keith, G. A. Petersson, J. A. Montgomery, K. Raghavachari, M. A. Al-Laham, V. G. Zakrzewski, J. V. Ortiz, J. B. Foresman, J. Cioslowski, B. B. Stefanov, A. Nanayakkara, M. Challacombe, C. Y. Peng, P. Y. Ayala, W. Chen, M. W. Wong, J. L. Andres, E. S. Replogle, R. Gomperts, R. L. Martin, D. J. Fox, J. S. Binkley, D. J. Defrees, J. Baker, J. P. Stewart, M. Head-Gordon, C. Gonzalez, and J. A. Pople. Gaussian 94, revision e.2. 1995.

[59] L. Verlet. *J. Phys. Chem.*, 159:98, 1967.

[60] DL_POLY is a package of molecular simulation routines written by W. Smith and T. R. Forester, copyright The Council for the Central Laboratory of the Research Councils, Daresbury Laboratory at Daresbury, Nr. Warrington (1996). The replicated data form of SHAKE is called RD-SHAKE and is described in section 2.6.8 of the DL_POLY_2.0 reference manual.

[61] GBMOL: A replicated data molecular dynamics program to simulate combinations of Gay-Berne and Lennard-Jones sites. Author: Mark R. Wilson, University of Durham, (1996).

[62] D. Fincham. *CCP5 Quarterly*, 2:6, 1981.

[63] D. Fincham. *CCP5 Quarterly*, 10:43, 1983.

[64] D. Fincham. *CCP5 Quarterly*, 12:47, 1984.

[65] G. R. Luckhurst, R. A. Stephens, and R. W. Phippen. *Liq. Cryst.*, 8:451, 1990.

[66] K. Singer, A. Taylor, and J. V. L. Singer. *Molec. Phys.*, 33:1757, 1977.

[67] J. P. Ryckaert. *Molec. Phys.*, 55:549, 1985.

[68] P. H. Berens, D. H. J. Mackay, G. M. White, and K. R. Wilson. *J. Chem. Phys.*, 79:2375, 1983.

[69] R. Eppenga and D. Frenkel. *Molec. Phys.*, 52:1303, 1984.

[70] V. Zwetkoff. *Acta Physicoch. U. S. S. R.*, 10:557, 1939.

[71] C. Zannoni. Quantitative description of orientational order: rigid molecules. In J. W. Emsley, editor, *Nuclear magnetic resonance of liquid crystals.* D. Reidel Publishing Company, 1985.

[72] M. P. Allen and D. J. Tildesley. *Computer Simulation of Liquids*, chapter 11. Oxford University Press, Oxford, 1987.

[73] J. P. Hansen and I. R. McDonald. *Theory of Simple Liquids*, chapter 12. Academic Press, 1986.

[74] D. J. Tildesley and P. A. Madden. *Molec. Phys.*, 48:129, 1983.

[75] V. Reiffenrath and F. Schneider. *Z. Naturforsch A*, 36:1006, 1981.

[76] M. Claessens, M Ferrario, and J. P. Ryckaert. *Molec. Phys.*, 50:217, 1983.

[77] T. R. Forester and W. Smith. *Unpublished.*

[78] T. R. Forester and W. Smith. *DL_POLY_2.0.* DL_POLY is a package of molecular simulation routines written by W. Smith and T. R. Forester, copyright The Council for the Central Laboratory of the Research Councils, Daresbury Laboratory at Daresbury, Nr. Warrington (1996).

[79] W. G. Hoover. *Phys. Rev. A*, 31:1695, 1985.

[80] M. R. Wilson. *J. Chem. Phys.*, 107:8654, 1997.

[81] J. W. Emsley, G. R. Luckhurst, and C. P. Stockley. *Proc. R. Soc. Lond. A*, 381:117, 1982.

[82] J. W. Emsley, G. R. Luckhurst, and C. P. Stockley. *Molec. Phys.*, 44:565, 1981.

[83] R. M. Lynden-Bell and I. R. McDonald. *Molec. Phys.*, 43:1429, 1981.

[84] R. M. Lynden-Bell. Comparison of the resutls from simulations with the predictions of models for molecular reorientation. In W. J. Orville-Thomas A. J. Barnes and J. Yarwood, editors, *Molecular Liquids - Dynamics and Interactions.* D. Reidel Publishing Company, 1984.

[85] R. M. Lynden-Bell and W. A. Steele. *J. Phys. Chem.*, 88:6514, 1984.

[86] G. La Penna, E. K. Foord, J. W. Emsley, and D. J. Tildesley. *J. Chem. Phys.*, 104:233, 1996.

[87] *Jpn. Pat. application*, 125518, 1983.

[88] *Jpn. Pat. application*, 179293, 1982.

[89] N. A. Bumagin, E. V. Luzikova, and I. P. Beletskaya. *Russ. J. Organic Chem.*, 31:1496, 1995.

[90] M. A. Osman and T. Huynh-Ba. *Molec. Cryst. Liq. Cryst.*, 116:141, 1984.

[91] W. L. Jorgensen, J. D. Madura, and C. J. Swenson. *J. Am. Chem. Soc.*, 106:6638, 1984.

[92] J. L. Siepmann, S. Karaborni, and B. Smit. *Nature*, 23:330, 1993.

[93] C. J. Adam, S. J. Clark, M. R. Wilson, G. J. Ackland, and J. Crain. *Molec. Phys.*, 93:947, 1998.

[94] E. de Miguel, L. F. Rull, M. K. Chalam, and K. E. Gubbins. *Molec. Phys.*, 74:405, 1991.

[95] G. La Penna, D. Catalano, and C. A. Veracini. *J. Chem. Phys.*, 105:7097, 1996.

[96] D. J. Cleaver, C. M. Care, M. P. Allen, and M. P. Neal. *Phys. Rev. E*, 54:559, 1996.

[97] M. P. Allen, M. A. Warren, M. R. Wilson, A. Sauron, and W. Smith. *J. Chem. Phys.*, 105:2850, 1996.

[98] M. R. Wilson, M. P. Allen, M. A. Warren, A. Sauron, and W. Smith. *J. Comput. Chem.*, 18:478, 1997.

[99] E. de Miguel, E. M. del Rio, J. T. Brown, and M. P. Allen. *J. Chem. Phys.*, 105:4234, 1996.

[100] D. Frenkel. *J. Phys. Chem.*, 92:3280, 1988.

[101] J. T. Brown, M. P. Allen, E. M. del Rio, and E. de Miguel. *Phys. Rev. E*, 57:6685, 1998.

[102] J. T. Brown. *Ph.D. thesis, University of Bristol*, 1996.

[103] M. R. Wilson. *Liq. Cryst.*, 21:437, 1996.

[104] U. Finkenzeller. *Kontakte (Darmstadt)*, 2:7, 1988.

[105] F. C. Frank. *Discuss. Faraday Soc.*, 25:19, 1958.

[106] M. P. Allen and D. Frenkel. *Phys. Rev. A Rapid Commun.*, 37:1813, 1988.

[107] D. Forster. *Annals of Physics*, 84:505, 1974.

[108] D. Forster. *Hydrodynamic Fluctuations, Broken Symmetry and Correlation Functions*, chapter 11. W. A. Benjamin, Inc., 1975.

[109] J. F. Nye. *Physical Properties of Crystals*, chapter 9. Oxford University Press, 1957.

[110] H. Usui, H. Takezoe, A. Fukuda, and E. Kuze. *Jpn. J. Appl. Phys.*, 18:1599, 1979.

[111] I. Haller. *J. Chem. Phys.*, 57:1400, 1972.

[112] F. Rondelez and J. P. Hulin. *Solid State Commun.*, 10:1009, 1972.

[113] L. Léger. *Mol. Cryst.*, 24:33, 1973.

[114] J. E. Mark. Silicon-based polymer science. In J. M. Zeigler and F. W. G. Fearon, editors, *Advances in Chemistry Series*, volume 224. American Chemical Society, 1990.

[115] I. Bahar, I. Zuniga, R. Dodge, and W. L. Mattice. *Macromolecules*, 24:2986, 1991.

[116] I. Bahar, I. Zuniga, R. Dodge, and W. L. Mattice. *Macromolecules*, 24:2993, 1991.

[117] P. J. Flory. *Statistical Mechanics of Chain Molecules.* Hanser Publishers, 1969.

[118] W. L. Mattice and U. W. Suter. *Conformational Theory of Large Molecules.* John Wiley and Sons Inc., 1994.

[119] S. Grigoras and T. H. Lane. *J. Comput. Chem.*, 9:25, 1987.

[120] W. L. Jorgensen. *J. Chem. Phys.*, 87:5304, 1983.

[121] P. D. Lickiss, A. D. Redhouse, R. J. Thompson, W. A. Stanczyk, and K Rozga. *J. Organometallic Chem.*, 453:13, 1993.

[122] D. S. Maxwell, J. Tirado-Rives, and W. L. Jorgensen. *J. Comput. Chem.*, 16:984, 1995.

[123] T. A. Halgren. *J. Comput. Chem.*, 17:490, 1996.

[124] T. A. Halgren. *J. Comput. Chem.*, 17:520, 1996.

[125] T. A. Halgren. *J. Comput. Chem.*, 17:553, 1996.

[126] T. A. Halgren and R. B. Nachbar. *J. Comput. Chem.*, 17:587, 1996.

[127] T. A. Halgren. *J. Comput. Chem.*, 17:616, 1996.

[128] P. Procacci, T Darden, and M. Marchi. *J. Phys. Chem.*, 100:10464, 1996.

[129] M. R. Wilson and M. P. Allen. *Molec. Phys.*, 80:277, 1993.

[130] U. Burkert and N. L. Allinger. *Molecular Mechanics*, chapter 3. American Chemical Society, 1982.

APPENDIX A

Testing GBMOL: methane and butane

A.1 Introduction

In order to test the constant pressure algorithm and torsional potential within the code GB-MOL aspects of the work of Jorgensen *et al.* [91] were reproduced for the molecules methane and butane. The set of parameters developed by Jorgensen *et al.* [91] are particularly useful in the simulation of liquid crystals as they have been developed for the simulation of liquid hydrocarbons with the aim of studying organic and biochemical substrates at 298 K.

A.2 GBMOL Constant pressure algorithm

In GBMOL a Monte Carlo method [69, 129] is used to maintain a constant pressure in the simulation. In this method a random number is chosen from the uniform range

($-\delta_{max}$,δ_{max}). A box dimension is chosen at random, the new volume is then given by

$$V_{new} = V_{old} \exp(\delta). \tag{A.1}$$

The value of δ_{max} is chosen such that the acceptance ratios are in the range 35-50%. In the case of isotropic scaling equation A.1 becomes

$$V_{new} = L_x \exp\left(\frac{\delta}{3}\right) \; L_y \exp\left(\frac{\delta}{3}\right) \; L_z \exp\left(\frac{\delta}{3}\right). \tag{A.2}$$

The volume move is accepted with a probability of (1,exp($-\beta\Delta H$)), where

$$\beta\Delta H = \beta\Delta E + \beta P\Delta V - (N_m + 1)\delta. \tag{A.3}$$

Here, N_m is the number of molecules in the system, β= 1/kT, and ΔE is the energy difference between the new and old configurations. The molecular centers of mass are relocated by a scaling factor, whilst the molecules maintain their original intramolecular configuration.

A.3 Methane

A.3.1 Computational

Methane was modelled as a single united atom methylene site using the Lennard Jones 12-6 potential (equation 1.2) with σ as 3.73 Å and ϵ as 0.294 kcal/mol. Each atom had mass of 0.2662141 x 10^{-25} kg.

A.3.2 Results and discussion

A series of 10 runs of 1 $\times 10^6$ steps (corresponding to 10 ns) were performed in the NPT ensemble. The system consisted of 125 molecules at 111.06 K, at a pressure of 1 atmosphere (1.01325 $\times$ 10^{-5} Pa). Figure A.1 shows a plot of the fluctuations in volume over the production run. Data collections were made every 250 steps (i.e. every

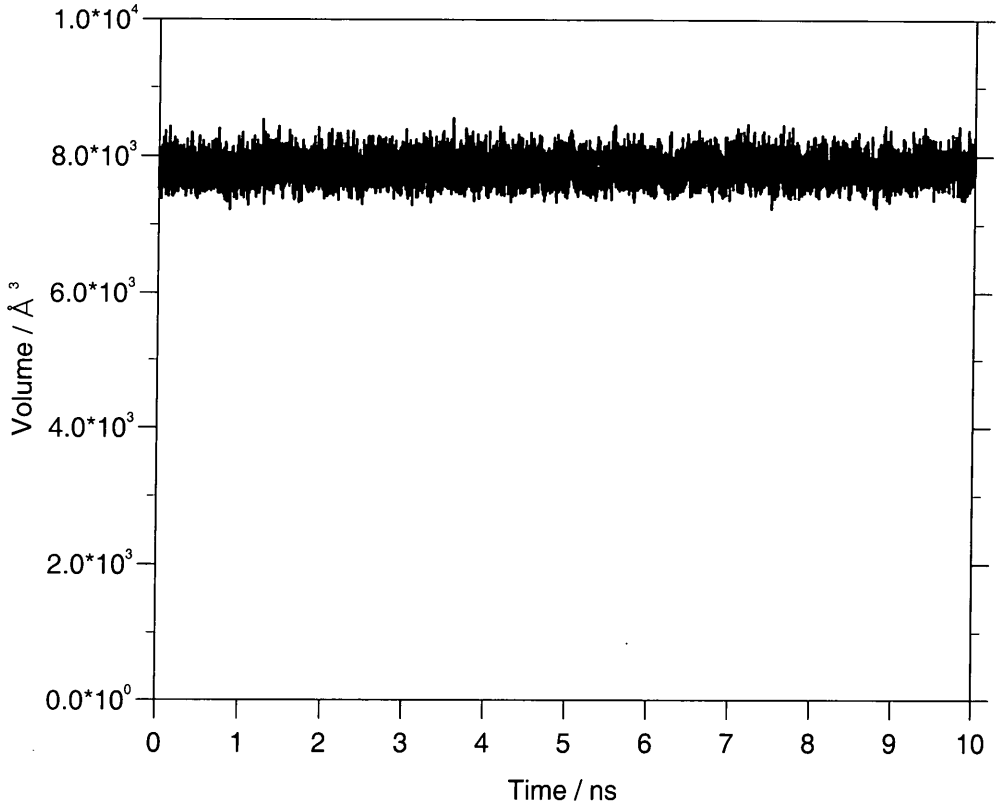

Figure A.1: System volume for a 10 ns run for methane

500 fs). The mean volume, over the production run, was 62.58 Å^3 per molecule. This corresponds to a density of 425.38 kg m^{-3} . This result can be compared with 63.3 Å^3 (421 kg m^{-3}) per molecule from the work of Jorgensen, and 62.8 Å^3 (424 kg m^{-3}) per molecule from experiment.

Calculation of the C-C radial distribution function for a system of 1000 atoms yields peaks at 4.05 Å, at a height of 2.97, and at 7.80 Å at a height of 1.30. These peaks correspond to the first and second solvation shells, and can be compared to peaks of 4.1 Å, and 7.8 Å, with respective heights of 2.9 and 1.3 found by Jorgensen *et al.* [91]. It is interesting to note that the location of the first peak lies just below the equilibrium value of 4.19 Å (derived from $r_0 = (2)^{1/6}\sigma$), which can be explained by an anisotropic

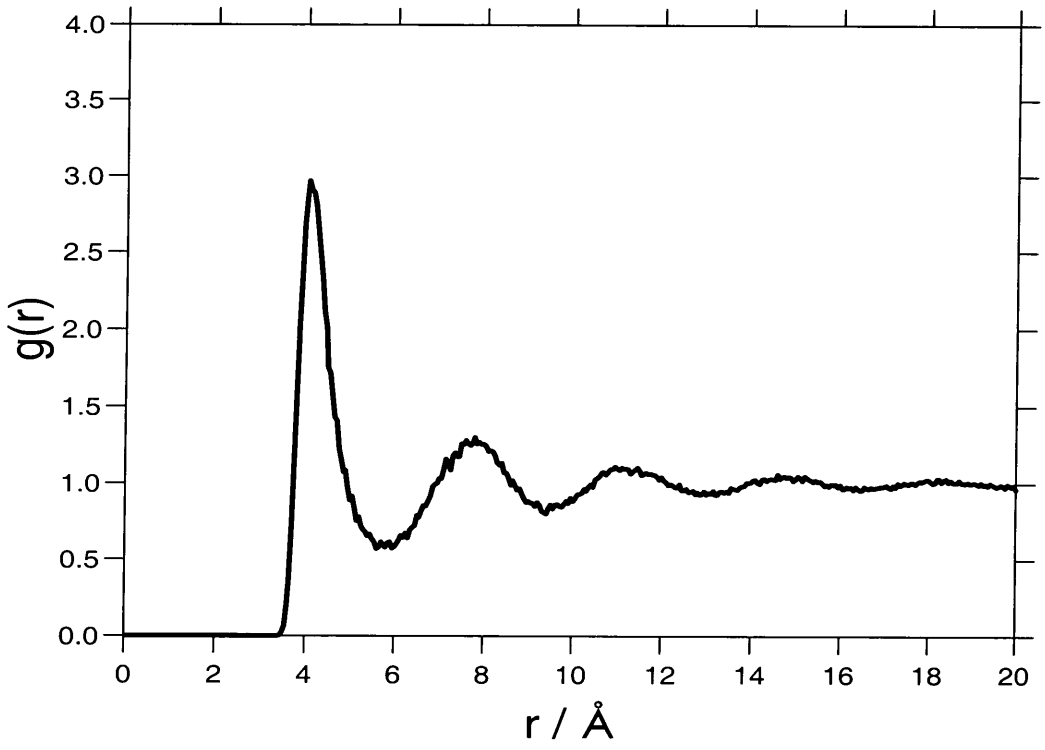

Figure A.2: RDF for a system of 1000 Lennard-Jones methane atoms at 111.06K

distribution of particle collisions.

A.4 Butane

A.4.1 Computational

The butane molecule was modelled as four united-atom CH_n sites, represented by Lennard-Jones potentials situated on the carbon atoms. The bond lengths were fixed at 1.53 Å and the angles to 112.0°. Lennard Jones 12-6 parameters were taken to be σ = 3.905 Å and ϵ = 0.118 kcal/mol. The butane molecule is the first alkane to possess a torsional potential. This potential can be described by a Fourier series [91]

$$V(\phi) = \frac{V_1}{2}(1 + \cos\phi) + \frac{V_2}{2}(1 - \cos 2\phi) + \frac{V_3}{2}(1 + \cos 3\phi) \qquad \text{(A.4)}$$

where the Fourier coefficients given for the n-butane molecule are V_1 = 1.522 kcal mol^{-1}, V_2 = -0.315 kcal mol^{-1}, and V_3 = 3.207 kcal mol^{-1}. A production run of 2 $\times 10^6$ steps (corresponding to 2 ns) was performed in the NPT ensemble. The system consisted of 125 molecules at 298.0 K at a pressure of 1 atmosphere (1.01325 $\times$ 10^{-5} kg s^{-2} $Å^{-1}$).

A.4.2 Results and discussion

A mean volume of 168.327 $Å^3$ per molecule was obtained from the production run, corresponding to a density of 572.956 kgm^{-3}. This compares with 168.7 $Å^3$ (572 kg m^{-3}) per molecule [91], and 168.4 $Å^3$ (573 kg m^{-3}) per molecule experimentally. The dihedral angle distribution is plotted in figure A.3, with a *trans* population of 67.69 % compared to 69.3 % in reference [91].

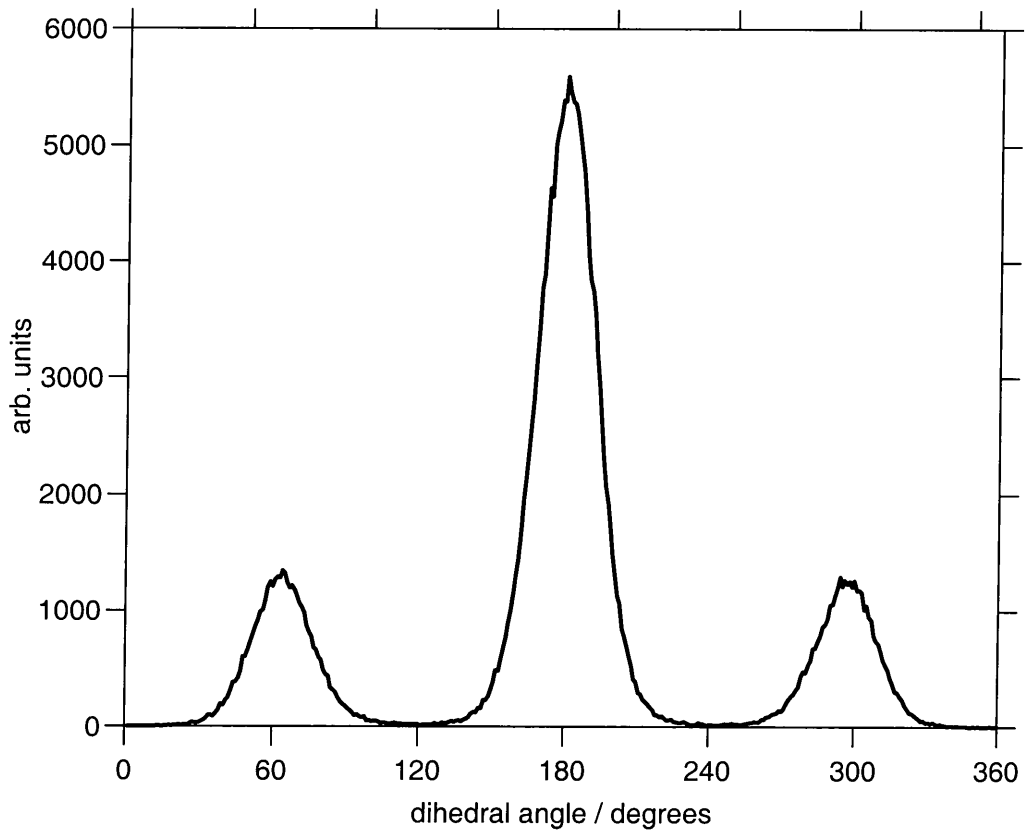

Figure A.3: Dihedral angle distribution for butane at 298 K

APPENDIX B

Ethane torsional potential

As a precursor to undertaking a study of the torsional potentials in the poly-(dimethylsiloxane) system, the an *ab initio* rotational barrier for ethane was calculated using the method prescribed by Maxwell *et al.* [122]. The minimum energy structure was computed at the RHF/6-31G*//RHF/6-31G* level using the program Gaussian94 [58]

B.1 Results

The structure calculated had a relaxed energy of -79.2287550 au, compared to the Maxwell *et al.* structure had an energy of -79.2287559 au. From this energy minimised structure a relaxed scan was performed consisting of four steps of 15°. The results are in excellent agreement with those in reference [122].

Bond length		Maxwell *et al.*
C-C	1.5274 Å	1.527 Å
C-H	1.0856 Å	1.086 Å
Bond angle		
C-C-H	111.202°	111.2°
H-C-H	107.680°	107.7°
Dihedral		
H-C-C-H	59.996°	60.0°

Table B.1: Gaussian94 minimum energy structure of ethane.

H-C-C-H	Relative energy	Relative energy (Maxwell *et al.*)
0°	2.985864	2.986
15°	2.519293	2.518
30°	1.434854	1.436
45°	0.409525	0.410
60°	0.000000	0.000

Table B.2: Torsional energy results for ethane in kcal/mol

APPENDIX C

Energy minimisation

C.1 Introduction

The problem is to perform a relaxed energy scan, in which certain features of the molecule, for example a dihedral angle, are fixed, whilst the remaining molecular geometry is relaxed. In the one-dimensional case the energy of the system can be written as

$$E = f(x). \tag{C.1}$$

The minimum energy, at point $x = x_{min}$ is given by

$$\frac{dE(x)}{dx} = 0 \tag{C.2}$$

(whether this is a global or a local minimum is a separate question). For a general point

$$x_{min} = x + \delta x \tag{C.3}$$

hence equation C.2 can be written as

$$\frac{dE(x+\delta x)}{dx} = 0 \tag{C.4}$$

If we expand equation C.4 as a Taylor series

$$0 = E'(x+\delta x) = E'(x) + E''(x)\delta x + \frac{1}{2}E'''(x)\delta x^2 + ... \tag{C.5}$$

Taking the first two terms of this series gives

$$0 \approx E'(x) + E''(x)\delta x \tag{C.6}$$

$$\Rightarrow E'(x) = -E''(x)\delta x \tag{C.7}$$

$$\delta x = -\frac{E'(x)}{E''(x)} \tag{C.8}$$

hence

$$x_{min} = x - \frac{E'(x)}{E''(x)}. \tag{C.9}$$

As this is a truncation at the second term, this is no longer the exact minimum. If this equation is used in a iterative scheme then, for a well behaved function, this will converge on the exact minimum. For a molecule containing N atoms, the energy of a conformation is given by a function of $3N$ variables

$$E = E(x_1, y_1, z_1, ..., x_N, y_N, z_N) \tag{C.10}$$

$E'()$ now becomes a vector, known as the force vector. The force vector represents the slope of the potential energy surface (PES). Similarly $E''()$ is replaced by a $3N \times 3N$ matrix of second derivatives, known as the Hessian matrix. The Hessian matrix represents the curvature of the PES. Equation C.9 becomes

$$\mathbf{r}_{min} = \mathbf{r} - \mathbf{H}^{-1}\mathbf{F} \tag{C.11}$$

where $\mathbf{r}$ is the postion vector, $\mathbf{r}_{min}$ is the location of an energy minima and

$$\mathbf{H}^{-1}\mathbf{F} = \begin{pmatrix} \frac{\partial E}{\partial x_1} \\ \frac{\partial E}{\partial y_1} \\ \frac{\partial E}{\partial z_1} \\ \cdot \\ \cdot \\ \cdot \\ \frac{\partial E}{\partial x_N} \\ \frac{\partial E}{\partial y_N} \\ \frac{\partial E}{\partial z_N} \end{pmatrix} \begin{pmatrix} \frac{\partial^2 E}{\partial x_1^2} & \frac{\partial^2 E}{\partial x_1 \partial y_1} & \frac{\partial^2 E}{\partial x_1 \partial z_1} & \cdots & \frac{\partial^2 E}{\partial x_1 \partial x_N} & \frac{\partial^2 E}{\partial x_1 \partial y_N} & \frac{\partial^2 E}{\partial x_1 \partial z_N} \\ \frac{\partial^2 E}{\partial y_1 \partial x_1} & \frac{\partial^2 E}{\partial y_1^2} & \frac{\partial^2 E}{\partial y_1 \partial z_1} & \cdots & \frac{\partial^2 E}{\partial y_1 \partial x_N} & \frac{\partial^2 E}{\partial y_1 \partial y_N} & \frac{\partial^2 E}{\partial y_1 \partial z_N} \\ \frac{\partial^2 E}{\partial z_1 \partial x_1} & \frac{\partial^2 E}{\partial z_1 \partial y_1} & \frac{\partial^2 E}{\partial z_1^2} & \cdots & \frac{\partial^2 E}{\partial z_1 \partial x_N} & \frac{\partial^2 E}{\partial z_1 \partial y_N} & \frac{\partial^2 E}{\partial z_1 \partial z_N} \\ \cdot & \cdot & \cdot & \cdots & \cdot & \cdot & \cdot \\ \cdot & \cdot & \cdot & \cdots & \cdot & \cdot & \cdot \\ \cdot & \cdot & \cdot & \cdots & \cdot & \cdot & \cdot \\ \frac{\partial^2 E}{\partial x_N \partial x_1} & \frac{\partial^2 E}{\partial x_N \partial y_1} & \frac{\partial^2 E}{\partial x_N \partial z_1} & \cdots & \frac{\partial^2 E}{\partial x_N^2} & \frac{\partial^2 E}{\partial x_N \partial y_N} & \frac{\partial^2 E}{\partial x_N \partial z_N} \\ \frac{\partial^2 E}{\partial y_N \partial x_1} & \frac{\partial^2 E}{\partial y_N \partial y_1} & \frac{\partial^2 E}{\partial y_N \partial z_1} & \cdots & \frac{\partial^2 E}{\partial y_N \partial x_N} & \frac{\partial^2 E}{\partial y_N^2} & \frac{\partial^2 E}{\partial y_N \partial z_N} \\ \frac{\partial^2 E}{\partial z_N \partial x_1} & \frac{\partial^2 E}{\partial z_N \partial y_1} & \frac{\partial^2 E}{\partial z_N \partial z_1} & \cdots & \frac{\partial^2 E}{\partial z_N \partial x_N} & \frac{\partial^2 E}{\partial z_N \partial y_N} & \frac{\partial^2 E}{\partial z_N^2} \end{pmatrix}^{-1} \tag{C.12}$$

Simple minimisation techniques, such as the steepest descent method, only make use of the slope of the PES and treat the Hessian matrix as a constant. In the 'block diagonal' Newton-Raphson method, an approximate version of the Hessian matrix is calculated [130]; the Hessian matrix is divided up into 3×3 submatrices along the diagonal. 'Off-diagonal' terms are neglected as these are comparatively small. It must be stressed that these methods find the nearest saddle point, or minima, from the starting point, not necessarily the global minima.

C.1.1 Relaxed scan

It is sometimes required to perform an energy minimisation whilst fixing one aspect of the molecular geometry. At this stage many minimisation routines remain in Cartesian coordinates. The feature of interest (for example a torsional angle) is constrained by applying a very large force constant. A more correct approach would be to transform the Hessian matrix from Cartesian coordinates to internal coordinates, set the partial derivative of that feature to be zero, then transform the Hessian matrix back into Cartesian coordinates. With the value of a feature fixed, one is able then to perform

energy minimisation calculations for a series of conformations, providing the form of the torsional potential as obtained in the study in chapter 6.

APPENDIX D

Postgraduate Courses

This appendix contains the syllabi of the graduate lecture courses attended during my Ph.D. studies.

D.1 Physical Chemistry of Polymers

Statistics of polymer molecules, average dimensions, models, distribution functions, influence of solvent. Thermodynamics of polymer systems, Flory-Huggins, excluded-volume and equation-of-state theories. Radiation-scattering, methods for the size and shape of the molecules. Light scattering from small particles, from large particles, anisotropic molecules, copolymers, mixed solvents. Small-angle scattering; X-rays and neutrons. Global dynamics of dilute polymer solutions; viscosity and its relation to molecular weight; evaluation of two parameter theories of polymer solution behaviour. Quasi-elastic light scattering, basis, correlation functions, diffusion coefficients.

D.2 Diffraction and scattering methods

Summary of crystallographic terms: Bragg's Law, diffraction theory, space-group symbols and their definition, calculation of structure factors and molecular density from measured intensities. Introduction to the practical methods used to measure diffraction data; their analysis to solve crystal structures. Introduction to the methods for recording intensity data: photographic, powder single crystal. 4-circle automated diffractometer, electronic counting. Allowance for the systematic errors in the experiment, interpretation and application of the crystallographic results. Interpretation of crystallographic papers in the literature.

D.3 Molecular Modelling

Definition of molecular modelling. Range of chemical applications. Overview of computational methods. Availability of software. Links to experimental results. Energy and force-fields in molecular dynamics. Optimisation of molecular geometry. Conformational-space analysis. Simulation of molecular dynamics. Intermolecular interactions in crystals, host-guest complexes and proteins. Semi-empirical methods. Electronic effects in conjugated π-systems. *Ab initio* calculations. Density functional theory.

APPENDIX E

Conferences

This appendix contains the details of the conferences attended during the course of my Ph.D. studies. Details of the papers presented are also listed.

1998 September 7-9:	CCP5 Annual Meeting: Making and Breaking Potentials, University of Edinburgh. Presentation: Molecular Dynamics simulation of Flexible Liquid Crystal Molecules.
1998 August 10-15:	EPSRC Graduate School, High Melton, Yorkshire.
1998 June 11-21:	NATO ASI Advances in Computer Simulations of Liquid Crystals, Erice, Sicily. Presentation: Molecular Dynamics simulation of Flexible Liquid Crystal Molecules.

1998 April 6-8: BLCS Annual Meeting, University of Leeds.
Presentation: Molecular Dynamics simulation of a
Flexible Liquid Crystal Molecule using a
Gay-Berne/Lennard-Jones model.

1998 March 24-27: CCP6 workshop: Optimisation Methods in Chemical Physics,
University of Durham.

1997 December 16-19: IOP Condensed Matter and Materials Physics Conference,
University of Exeter.

1997 November 28: Qu ımica Suave y Superconductividad, University Complutense in Madrid.

1997 November 7: Coherent Raman Spectroscopy of van der Waals and Hydrogen
Bonded Clusters, University Complutense in Madrid.

1997 October 24: Local Treatment of Electron Correlation in Large Molecules,
University Complutense in Madrid.

1997 October 17: Potential Distribution Theorems in Chain Molecules,
University Complutense in Madrid.

1997 September 22-23: RSC Structured Fluids, University of Durham.

1997 July 16: Hewlett Packard Java Programming Workshop, University of Durham.

1997 July 14-15: Hewlett Packard Network Printing Event, University of Durham.

1997 April 6-11: CCP5 Spring School: Methods in Molecular Simulation,
University of Bristol.
Presentation: Molecular Dynamics simulation of Realistic Liquid Crystals

1997 April 2: IOP Molecular Modelling and Neutron Scattering Workshop, Oxford.

1997 March 24-26: BLCS Annual Meeting, University of Southampton.
Poster: Molecular Dynamics simulation of Realistic Liquid Crystals.

1997 January 27: Further UNIX and Writing C-shell scripts, University of Durham.

1996 December 17-19: BLCS Winter Workshop, University of Hull.

1996 November 14: BCA Chemical Crystallography Group Autumn meeting: Dynamic Crystallography.

1996 September 23-25: CCP5 Annual Meeting: Condensed Matter Simulation: Realising the Potential of the Computer, University of Bristol. Presentation: A Molecular Dynamics study of Flexible Liquid Crystals.